

UC San Diego

UC San Diego Electronic Theses and Dissertations

Title

A Meshfree Computational Framework for Modeling Hydro-Mechanical Damage Processes in Porous Geomaterials

Permalink

<https://escholarship.org/uc/item/2xr741p1>

Author

Wei, Haoyan

Publication Date

2018

Peer reviewed|Thesis/dissertation

UNIVERSITY OF CALIFORNIA SAN DIEGO

**A Meshfree Computational Framework for Modeling Hydro-Mechanical Damage
Processes in Porous Geomaterials**

A dissertation submitted in partial satisfaction of the
requirements for the degree Doctor of Philosophy

in

Structural Engineering

by

Haoyan Wei

Committee in charge:

Professor Jiun-Shyan Chen, Chair
Professor Randolph E. Bank
Professor Yuri Bazilevs
Professor John S. McCartney
Professor Ingrid Tomac

2018

Copyright

Haoyan Wei, 2018

All rights reserved.

The Dissertation of Haoyan Wei is approved, and it is acceptable in quality and form for publication on microfilm and electronically:

Chair

University of California San Diego

2018

DEDICATION

To my family

TABLE OF CONTENTS

Signature Page	iii
Dedication	iv
Table of Contents	v
List of Figures	viii
List of Tables	xi
Acknowledgements.....	xii
Vita.....	xiv
Abstract of the Dissertation	xvi
Chapter 1 Introduction	1
1.1 Motivation.....	1
1.2 Objective	3
1.3 Outline.....	5
Chapter 2 Literature Review	7
2.1 Poromechanics for Multiphase Geomaterials	7
2.2 Overview of Numerical Methods for Poromechanics	8
2.2.1 Mesh-based Methods	8
2.2.2 Meshfree Methods	11
2.3 Challenges in Modeling Hydro-Mechanical Damage Processes	11
2.3.1 Inf-Sup Stability Constraints	12
2.3.2 Fracture Modeling.....	14
2.3.2.1 Discrete Crack Approaches	15
2.3.2.2 Smearred Crack Approaches.....	16
2.3.2.3 Methods for Hydraulic Fracture Simulation.....	17
2.3.3 Post-Failure Modeling of Landslides.....	20
2.3.3.1 Mesh Distortion Issues in Mesh-based Methods	20
2.3.3.2 Meshfree Methods for Landslide Modeling.....	21

	2.3.3.3 Domain Integration Techniques in Meshfree Methods	22
Chapter 3	A Stabilized Nodally Integrated Meshfree Formulation for Hydro-Mechanical Analysis of Saturated Porous Media	25
3.1	Governing Equations of Fluid-Saturated Porous Media.....	25
3.1.1	Strong Form	25
3.1.2	Weak Form.....	28
3.2	Reproducing Kernel Mixed Formulation.....	30
3.2.1	Reproducing Kernel Approximation.....	30
3.2.2	Reproducing kernel u-p Approximation and Discretization	32
3.2.3	Discrete Equations	34
3.3	Fluid Pressure Projection for Meshfree Method with Nodal Integration	35
3.3.1	Pressure Projection.....	35
3.3.2	Stabilized Conforming Nodal Integration for Pressure Projection	39
3.4	Numerical Examples	45
3.4.1	Terzaghi's Problem.....	45
3.4.2	Mandel's Problem.....	47
3.4.3	Strip Load on Elastic Half Space	52
Chapter 4	A Damage Particle Method for Smeared Modeling of Brittle Fracture	57
4.1	Continuum Damage Model.....	57
4.2	The Damage Particle Method	63
4.2.1	Variational Equation	63
4.2.2	Approximation of Fracture Surfaces by Damaged Particles.....	64
4.2.3	Dissipation Energy-based Regularization.....	68
4.2.4	Meshfree Discrete Equationsn	71
4.3	Numerical Examples	75
4.3.1	A Cracked Bar Under Tension.....	75
4.3.2	Kalthoff's Impact Problem	81
4.3.3	Dynamic Crack Branching Problem	86
Chapter 5	Application of the Damage Particle Method for Hydraulic Fracturing Simulation ...	89
5.1	Smeared Crack Model for Fractured Saturated Porous Media	89

5.1.1	Balance Equations.....	89
5.1.2	Continuum Damage Model for Fluid-filled Cracks.....	90
5.1.3	Cracking-enhanced Permeability Model.....	91
5.2	Reproducing Kernel Mixed Formulation.....	95
5.2.1	Variational Equations.....	95
5.2.2	Discrete Equations	96
5.3	Numerical Examples	90
5.3.1	Sneddon’s Pressurized Crack Problem	102
5.3.2	Fluid Injection-induced Crack Propagation in Porous Media.....	105
5.3.3	Blanton’s Hydraulic Fracturing Tests	109
Chapter 6	Semi-Lagrangian Reproducing Kernel Formulation for Landslide Modeling.....	115
6.1	Review of Nonlinear Poromechanics.....	115
6.1.1	Kinematics	116
6.1.2	Balance Equations.....	118
6.1.3	Constitutive Laws	120
6.1.4	Strong Form of the u-p Formulation.....	121
6.2	Semi-Lagrangian Reproducing Kernel Mixed Formulation	123
6.2.1	Semi-Lagrangian Reproducing Kernel Approximation.....	123
6.2.2	Variational Equations.....	126
6.2.3	Temporal Discretization.....	127
6.3	Naturally Stabilized Nodal Integration	129
6.4	Numerical Examples	137
6.4.1	Wave Propagation in Poroelastic Media.....	137
6.4.2	Liakopoulos’ Drainage Experiment.....	141
6.4.3	Seepage-induced Levee Failure	144
Chapter 7	Conclusions and Future Work.....	148
7.1	Conclusions.....	148
7.2	Recommendations for Future Research	150
References	151

LIST OF FIGURES

Figure 3.1	A fluid saturated porous medium	25
Figure 3.2	A domain discretized by meshfree particles and the associated reproducing kernel shape function	30
Figure 3.3	Nodal representative domain for stabilized conforming nodal integration and fluid pressure projection	41
Figure 3.4	Description of Terzaghi’s problem.....	45
Figure 3.5	Normalized fluid pressure profile for Terzaghi’s problem.....	46
Figure 3.6	Normalized fluid pressure profile near the drainage boundary	47
Figure 3.7	Description of Mandel’s problem.....	47
Figure 3.8	Normalized fluid pressure distribution.....	50
Figure 3.9	Normalized fluid pressure distribution for Mandel’s problem at various dimensionless time.....	51
Figure 3.10	Description of the footing problem and its meshfree numerical model with the Voronoi diagram.....	52
Figure 3.11	Normalized fluid pressure distribution along the central vertical line	53
Figure 3.12	Time history of fluid pressure	54
Figure 3.13	Numerical results of the fluid pressure, horizontal displacement, and vertical displacement distribution for the low permeable case	55
Figure 4.1	The failure process of a bar with weakened material at the middle cross-section and the expected load-displacement response.....	59
Figure 4.2	Illustration of adopting the discrete cohesive zone model and the continuum damage model for the cracked bar problem.....	60
Figure 4.3	The 1-D stress-strain relationship based on the continuum damage model	61
Figure 4.4	The fracture path and its approximation based on a set of crack segments passing the nodal points of the meshfree model.....	65
Figure 4.5	The nodal representative domain and boundary integral for smeared strain computation	66
Figure 4.6	The potential cracking zone and the crack prevention zone associated with the	

	damaged particle.....	68
Figure 4.7	Voronoi cell associated with the damaged particle	69
Figure 4.8	Load-displacement curves obtained from unregularized particle-based damage formulation and the proposed damage particle method	76
Figure 4.9	Evolution of crack opening displacement versus the displacement at the loading end of the bar	77
Figure 4.10	The smeared cracking zone in terms of non-zero damage distribution along the bar	78
Figure 4.11	Distribution of axial stress along the bar	79
Figure 4.12	Kalthoff's impact problem	81
Figure 4.13	Distribution of the damage state.....	82
Figure 4.14	Comparison of the crack growth paths between the Kalthoff's experimental result and different numerical simulation.....	83
Figure 4.15	Evolution of global fracture energy dissipation	84
Figure 4.16	Distribution of the damage state obtained when the damage particle tracking procedure is deactivated	85
Figure 4.17	The dynamic crack branching problem	86
Figure 4.18	Distribution of the damage state.....	87
Figure 4.19	Evolution of global fracture energy dissipation	88
Figure 5.1	Fluid fluxes along a discret fracture and smeared crack zone.....	93
Figure 5.2	Distribution of the imposed fluid pressure and damage state	102
Figure 5.3	Crack opening displacement distribution along the crack surface	103
Figure 5.4	The predicted displacement and stress distribution.....	104
Figure 5.5	A fluid-saturated plate with a pre-existing crack	105
Figure 5.6	Progressive evolution of the fluid pressure and the damage state.....	107
Figure 5.7	Fluid pressure and the associated Darcy velocity distribution	108
Figure 5.8	Illustration of hydraulic fracture and pre-fracture location	110

Figure 5.9	Modeling results of Blanton’s CT-4/CT-7 tests	113
Figure 5.10	Modeling results of Blanton’s CT-8/CT-9 tests	113
Figure 6.1	Illustration of the motion of a triphasic continuum.	117
Figure 6.2	Meshfree discretization with different types of kernel functions.....	123
Figure 6.3	Conforming nodal smoothing cells in SCNI and non-conforming nodal smoothing cells in SNNI.....	134
Figure 6.4	The problem set-up of wave propagation in poroelastic media	137
Figure 6.5	Time history of the solid displacement and the fluid pressure obtained from DNI- and NSNI-based RKPM formulations.....	138
Figure 6.6	Time history of the solid displacement and the fluid pressure obtained with different nodal discretization refinement	140
Figure 6.7	The set-up for Liakopoulos’ drainage experiment	141
Figure 6.8	Distribution of the water pressure along the height of the sand column	143
Figure 6.9	Time histories of the water pressure.....	144
Figure 6.10	Sketch of the levee problem	145
Figure 6.11	The RKPM simulation results of water pressure and equivalent plastic strain distribution in the levee	147

LIST OF TABLES

Table 5.1	Blanton's Test Conditions	111
-----------	---------------------------------	-----

ACKNOWLEDGEMENTS

I would like to express my sincere gratitude to my advisor, Professor J. S. Chen, for his careful guidance and constant encouragement throughout my Ph. D. studies. I feel very fortunate to have been a student in his research group, where I can learn so much from his extensive knowledge and great passion for pursuing creative ideas.

I acknowledge the members of my Ph.D. dissertation defense and candidacy exam committees: Professors Randolph Bank, Yuri Bazilevs, David Benson, John McCartney and Ingrid Tomac. I am very appreciative of their helpful comments and suggestions.

Thanks also go to numerous nice people I have met at both UCLA and UCSD. In particular, I am happily in debt of all my colleagues in the computational mechanics group: Jonghyuk Baek, Dr. Ramya Rao Basava, Frank Beckwith, Qizhi He, Dr. Michael Hillman, Tsung-Hui Huang, Jacob Koester, Dr. Shih-Po Lin, Chang Liu, Dr. Camille Marodon, Julio Martinez, Marco Pasetto, Dr. Marcus Rüter, Dr. Edouard Yreux, Dr. Yantao Zhang, Dr. Guohua Zhou, and many others. I am very thankful for their help and friendship. In addition, I would like to thank Dr. Hui-Ping Wang for helpful discussions during the conference and project meetings.

Chapter 3, in part, is a reprint of the material as it appears in “Wei, Haoyan, Chen, Jiun-Shyan, & Hillman, Michael. A Stabilized Nodally Integrated Meshfree Formulation for Fully Coupled Hydro-Mechanical Analysis of Fluid-Saturated Porous Media. *Computers & Fluids*, 141, 105-115, 2016”. The dissertation author was the primary investigator and author of this paper.

Chapter 4, in part, has been submitted for publication of the material as it may appear in “Wei, Haoyan, Chen, Jiun-Shyan. A Damage Particle Method for Smeared Modeling of Brittle Fracture. International Journal for Multiscale Computational Engineering, 2018”. The dissertation author was the primary investigator and author of this paper.

Last but not least, I will be forever indebted to my family for their endless love.

VITA

- 2009 Bachelor in Engineering Mechanics, Tongji University, Shanghai
- 2012 Master in Structural Engineering, Zhejiang University, Hangzhou
- 2018 Ph. D. in Structural Engineering, University of California, San Diego

Journal Publications

- 1) Wei, H., Chen, J. S. (2018). A damage particle method for smeared modeling of brittle fracture, *International Journal for Multiscale Computational Engineering*, under review.
- 2) He, Q., Wei, H., Chen, J. S., Wang, H. P., & Carlson, B. E. (2018). Analysis of hot cracking during lap joint laser welding processes using the melting state-based thermomechanical modeling approach. *The International Journal of Advanced Manufacturing Technology*, 94(9-12), 4373-4386.
- 3) Wei, H., He, Q., Chen, J. S., Wang, H. P., & Carlson, B. E. (2017). Coupled thermal-mechanical-contact analysis of hot cracking in laser welded lap joints. *Journal of Laser Applications*, 29(2), 022412.
- 4) Wei, H., Chen, J. S., Wang, H. P., & Carlson, B. E. (2016). Thermomechanical numerical analysis of hot cracking during laser welding of 6XXX aluminum alloys. *Journal of Laser Applications*, 28(2), 022405.
- 5) Wei, H., Chen, J. S., & Hillman, M. (2016). A stabilized nodally integrated meshfree formulation for fully coupled hydro-mechanical analysis of fluid-saturated porous media. *Computers & Fluids*, 141, 105-115.
- 6) Li, Z. X., Zhuo, X., Vu-Quoc, L., Izzuddin, B. A., & Wei, H. (2013). A four-node corotational quadrilateral elastoplastic shell element using vectorial rotational variables. *International Journal for Numerical Methods in Engineering*, 95(3), 181-211.
- 7) Wei, H., Li, Z. X., & Zhong, Z. (2012). Advanced nine-node corotational quadrilateral elastoplastic shell element. *Journal of Zhejiang University: Engineering Science*, 46(3), 424-430.

Conference Presentations

- 1) Wei, H., Chen, J. S. A mixed RKPM formulation for modeling hydro-mechanical damage processes in multiphase porous media. *13th World Congress on Computational Mechanics (WCCM)*. New York City, USA, June 2018.
- 2) Wei, H., Chen, J. S. A reproducing kernel damage particle method for fracture modeling. *18th U.S. National Congress for Theoretical and Applied Mechanics (USNC/TAM)*. Chicago, USA, June 2018.
- 3) Wei, H., Chen, J. S. A meshfree approach to modeling hydraulic fracturing in saturated porous media. *International Society for Porous Media (InterPore) 10th Annual Meeting*, New Orleans, USA, May 2018.
- 4) Wei, H., Chen, J. S., & Hillman, M. RKPM formulation for fully coupled hydro-mechanical analysis of fluid-saturated porous media. *Engineering Mechanics Institute Conference*, San Diego, USA, June 2017.
- 5) Pasetto, M., Chen, J. S., & Wei, H. Coupled Lagrangian and semi-Lagrangian RKPM. *Engineering Mechanics Institute Conference*, San Diego, USA, June 2017.
- 6) Wei, H., J. S. Chen, & M. Hillman. RKPM formulation for fully coupled hydro-mechanical analysis of fluid-saturated porous media. *United States Association for Computational Mechanics (USACM) Conference on Isogeometric Analysis and Meshfree Methods*, San Diego, USA, October 2016.
- 7) Wei, H., He, Q., Chen, J. S, Wang, H. P., & Carlson, B. E. Coupled thermal-mechanical-contact analysis of hot cracking in laser welded lap joints. *35th International Congress on Applications of Lasers & Electro-Optics (ICALEO)*, San Diego, USA, October 2016.
- 8) Wei, H., Chen, J. S, Wang, H. P., & Carlson, B. E. Thermomechanical numerical analysis of hot cracking in laser welding of 6xxx aluminum alloys. *34th International Congress on Applications of Lasers & Electro-Optics (ICALEO)*, Atlanta, USA, October 2015.
- 9) Wei, H., Chen, J. S. Towards a stabilized meshfree formulation for hydraulic fracturing simulation. *13th U.S. National Congress on Computational Mechanics (USNCCM)*, San Diego, USA, July 2015.

ABSTRACT OF THE DISSERTATION

A Meshfree Computational Framework for Modeling Hydro-Mechanical Damage Processes in
Porous Geomaterials

by

Haoyan Wei

Doctor of Philosophy in Structural Engineering

University of California San Diego, 2018

Professor Jiun-Shyan Chen, Chair

Hydro-mechanical damage processes occur in numerous geological hazards and engineering applications. Despite considerable effort made in the past years, reliable numerical prediction of failure processes in multiphase porous media remains challenging. This is mainly due to the complexity of the involved multi-physical phenomena, as well as the ineffectiveness of conventional mesh-based methods (e.g., FEM) which suffer from large deformation-induced mesh distortion issues and exhibit non-convergent solutions for damage and fracture problems. The objective of this work is to develop a robust meshfree computational framework for effective modeling of hydro-mechanical damage processes. To this end, a fluid pressure projection method is employed in conjunction with the stabilized conforming nodal integration to

achieve a stable reproducing kernel mixed formulation for poromechanics. Moreover, a damage particle method is developed for fracture modeling, where a smeared description of cracks is adopted to circumvent the burden associated with modeling complex crack patterns. To eliminate the pathological discretization size sensitivity, a scaling law is introduced in the damage model to ensure that the bulk damage energy dissipation over the nodal representative volume is consistent with the surface fracture energy of the crack segment. In addition, the smeared strain is computed as the boundary integral of displacements in each nodal representative domain, which avoids the ambiguity of taking direct derivatives of non-smooth displacements in the cracking region. As such, the computation of field and state variables along with the regularization procedure are all performed at nodal points, without any interpolation commonly needed in FEM. By incorporating the hydro-mechanical coupling, the damage particle method is capable of capturing the growth of fluid-driven cracks without tedious treatments of moving discontinuities. The effectiveness of the developed meshfree formulation is demonstrated in the modeling of hydraulic fracturing and landslides, which involves extreme deformation phenomena and interactions between solid, water and air phases.

Chapter 1

Introduction

In this chapter, the motivation for the present research work is introduced in Section 1.1, followed by the objectives of the research in Section 1.2. An outline of this dissertation is given in Section 1.3.

1.1 Motivation

Damage processes in multiphase porous media occur in numerous geological hazards and engineering applications. Typical examples are the rainfall-induced landslides which have caused significant casualties and economic losses worldwide [Petley (2012); Haque et al. (2017)]. Although extensive slope stability models have been developed, reliable numerical prediction of the failure process and its impact on the surroundings is still lacking because of the complexity of the involved multi-physics [McDougall (2016)]. On the application side of the damage processes in porous media, the hydraulic fracturing [Smith and Montgomery (2015)] has been utilized in the petroleum industry as a key technology to enhance the oil and gas productivity, even though the knowledge of the actual fracturing process remains mostly empirical [Bazant et al. (2014)].

To achieve reliable and efficient modeling of the abovementioned hydro-mechanical

damage processes, various computational formulations have been proposed over the years. However, the complex material failure mechanisms, extreme deformation and the interactions between the fluid and solid constitutions in the porous media still pose significant challenges to conventional numerical methods. For instance, as the ultimate impact of landslides depends not only on the failure initiation stage but also the post-failure process, the run-out analysis is of great importance in landside risk assessment and mitigation design, especially in cases involving extremely rapid, flow-like landslides, such as debris flows and rock avalanches [McDougall (2016)]. However, in these scenarios, the conventional mesh-based methods (e.g., FEM) often become ineffective due to mesh distortion issues which appear in large deformation problems. Meshfree methods (e.g., the Reproducing Kernel Particle Method [Liu et al. (1995); Chen et al. (1996)]), on the other hand, are well suited for capturing extreme deformation behaviors, because they naturally avoid computational difficulties associated with distorted or low-quality meshes [Chen et al. (1996); Chen, Hillman, Chi (2017)]. Nevertheless, current research on the development of robust meshfree methods for coupled hydro-mechanical analysis of porous media is still rare and deserves investigation.

Moreover, although fracture modeling has been of interest to the engineering community for decades, it remains tedious to capture a large set of evolving fractures using conventional approaches. For the discrete crack approaches, explicit tracking and modeling of discontinuous surfaces cause a number of non-trivial treatments, such as subdivision of quadrature cells, modification of mesh topology or nodal neighbor list, addition of extra nodal degrees of freedom, etc. These treatments greatly increase the computational complexity, especially when crack patterns are complicated (e.g., crack joining and branching) and hydro-mechanical couplings need to be considered. The smeared crack approaches, on the other hand, offer the advantage of

modeling fractures in a simple manner, where the sharp discontinuities are smeared over a finite domain and cracking effects are captured through a softened stress-strain law. Nonetheless, numerical methods based on smeared crack models often show mesh sensitive behaviors and yield non-convergent solutions upon model refinement. Although various regularization techniques, such as non-local damage models, have been developed to ensure convergent solutions in the smeared crack modeling, they are often computationally quite expensive for solving large-scale geotechnical engineering problems. Therefore, the development of an efficient and robust numerical modeling approach for the simulation of hydro-mechanically coupled fracturing processes is essential.

1.2 Objective

The objective of this work is to develop a meshfree method for the effective numerical simulation of hydro-mechanical damage processes in multiphase porous media. The specific developments are summarized as follows:

- 1) Development of a stable reproducing kernel mixed formulation for fully coupled hydro-mechanical analysis of porous media. Numerical modeling of reservoirs with low permeability or under nearly undrained conditions suffers from spurious fluid pressure oscillations due to the improper construction of approximation spaces. To address this issue, a fully coupled, stabilized meshfree formulation is developed based on a fluid pressure projection method, in which an additional stabilization term is added to the variational equation to correct the deficiency of the equal-order u-p reproducing kernel approximation. The projection scheme is formulated under the SCNI (Stabilized

Conforming Nodal Integration) framework which enables a significant enhancement of the computational efficiency and accuracy, and the spurious low-energy modes of nodal integration are also eliminated. The effectiveness of the proposed meshfree method is demonstrated by solving several hydro-mechanically coupled problems.

- 2) Development of a damage particle method for smeared modeling of brittle fracture. In this approach, the smeared strain is defined by the divergence operation with a boundary integral of displacements in each nodal representative domain, thus the ambiguity of taking direct derivatives of non-smooth displacements in the smeared cracking region is avoided. To address the discretization size sensitivity issue, a scaling law is introduced to the damage model based on the equivalence between the bulk damage energy dissipation and the surface fracture energy of the associated crack segment over the nodal representative domain. This approach is formulated under the SCNI framework, which allows the field and state variables to be calculated and stored at the same set of particles, avoiding interpolation of variables between nodal points and Gauss points in the conventional finite elements. Several numerical examples are presented to examine the effectiveness of the proposed method for fracture modeling.
- 3) Development of a hydro-mechanically coupled damage particle method for hydraulic fracturing modeling. The damage particle method is extended under the reproducing kernel mixed formulation, where the regularized smeared crack model is introduced to capture the fluid pressure-driven crack growth in fluid-saturated porous media. Moreover, convergent approximation of the COD (Crack Opening Displacement) is obtained based on the damage particle representation of fractures, and the extracted COD measure is

employed to define an anisotropic permeability model which can describe the enhanced fluid flow along fracture path. The resulting hydro-mechanically coupled damage particle method is shown to be effective in hydraulic fracture modeling.

- 4) Development of a stabilized semi-Lagrangian reproducing kernel mixed formulation for nonlinear modeling of multiphase porous media with application to landslide simulation. The semi-Lagrangian framework enables a robust approach to modeling extreme large deformation phenomena involving material flow and separation, and hydro-mechanical coupling of solid, water and air phases. To achieve a stable and accelerated solution to the coupled poromechanical problem, the naturally stabilized nodal integration scheme is employed, where implicit gradient-based stabilization terms associated with the strain and fluid pressure fields are introduced. The capability of the semi-Lagrangian formulation is demonstrated in several numerical examples, including post-failure modeling of a partially saturated levee.

1.3 Outline

The remainder of this dissertation is organized as follows. In the next chapter, an overview on fracture modeling approaches and meshfree methods for modeling multiphase porous media is given, along with discussions on the advantages and limitations of current computational methods. In Chapter 3, the reproducing kernel mixed formulation for hydro-mechanical analysis of saturated porous media is presented, where the fluid pressure projection method is formulated under the SCNI (Stabilized Conforming Nodal Integration) framework. Next, the damage particle method for smeared modeling of brittle fracture is

presented in Chapter 4, which is further extended for hydraulic fracture simulation by the incorporation of hydro-mechanical coupling effects in Chapter 5. Furthermore, the naturally stabilized nodal integration is employed in the semi-Lagrangian reproducing kernel mixed formulation for modeling partially saturated deformable porous media with application to run-out analysis of landslides in Chapter 6. Finally, conclusions and discussions on future research directions are given in Chapter 7.

Chapter 2

Literature Review

In this chapter, a general overview of poromechanics and associated numerical methods are reviewed in Section 2.1 and Section 2.2, respectively. Next, progress and challenges in modeling hydro-mechanical damage processes are discussed in Section 2.3.

2.1 Poromechanics for Multiphase Geomaterials

Geomaterials (e.g., soils and rocks) are naturally-occurring mixture of mineral, organic ingredients, cracks and open pores, which are filled with one or several types of fluids, and the interaction between the solid deformation and the fluid flow often have a significant effect on the material behaviors as well as associated failure processes. For instance, settlement of building structures on saturated soils can occur as the fluid is squeezed out slowly. During heavy rainfall, the negative water pressure (often called ‘suction’) in unsaturated soils can be significantly altered, which leads to reduced effective stress and shear strength of the solid skeleton, and ultimately induces landslides and debris flows. Similarly, a saturated or partially saturated soil can substantially lose strength and behave like a liquid (often referred to as ‘soil liquefaction’) in response to a rapid earthquake loading. In the process of hydraulic fracturing, cracks are formed in rocks due to the high pressure of injected fracking fluid. Meanwhile, hydraulic properties of rocks are altered and an enhanced fluid flow network is created by the interaction between the

hydraulic fractures and the natural fractures (faults, joints, bedding planes, etc.), which lead to the increased oil and gas production in low-permeable reservoirs.

Obviously, understanding the multi-physical response in porous geomaterials is important for a wide spectrum of engineering applications. To this end, the poromechanics theories as an extension of solid mechanics have been continuously developed since the classical contributions of Terzaghi (1925) to consolidation analysis. [Biot (1941)] first presented the theory of poroelasticity for isothermal, quasi-static phenomena in fluid-saturated porous media, which was later reformulated in [Rice and Cleary (1976)]. Dynamic effects were incorporated in [Biot (1956ab)], and non-isothermal effects were considered in [Palciauskas and Domenico (1982)], among many other developments. In general, the description of multiphase systems is today based either on averaging theories with a classical view point on Biot's theory, or on the mixture theory integrated by the concept of volume fractions [Coussy (2004)]. Under appropriate assumptions, the averaging theory yields exactly the same governing equations as the classical mixture theory [Lewis and Schrefler (1998)].

2.2 Overview of Numerical Methods for Poromechanics

2.2.1 Mesh-based methods

In the last few decades, a considerable progress has been made for developing computational poromechanical formulations to analyze problems for which conventional analytical approaches are ineffective. In the pioneering work of [Zienkiewicz et al. (1984)], various formulations were proposed based upon Biot's theory with different simplifications and choices of primary variables, among which the so-called u-p formulation (where solid

displacement u and pore fluid pressure p are chosen as primary variables) becomes the most popular theory in geotechnical engineering applications because of its simplicity and effectiveness. A nonlinear FEM (Finite Element Method) u - p formulation was then developed in [Zienkiewicz (1990ab)] for modeling static and dynamic behavior of soils, which shows the effectiveness of numerical computation by reproducing many of the phenomena for which previously only rough rules of thumb were available, such as an approximate yet satisfactory reconstruction of the failure of the lower San Fernando dam during the 1971 earthquake. The FE formulation of [Zienkiewicz (1990b)] for partially saturated porous media was further extended to account for finite strain effects in [Meroi, Schrefler, Zienkiewicz (1995)]. A FE formulation for modeling slow transient phenomena involving coupled heat, water and gas flow in deforming porous media was developed in [Gawin, Baggio, Schrefler (1995)], where the heat transfer through conduction and convection as well as the latent heat transfer is taken into account. Later, fully coupled FE models are developed to simulate the consolidation involving flow of water and air in deforming porous media in [Schrefler and Zhan (1993)] under quasi-static conditions, and in [Schrefler and Scotta (2001)] under dynamic conditions, where the pore gas pressure is treated as an additional primary variable. [Uzuoka and Borja (2012)] presented a dynamic formulation for unsaturated poroelastic solids at finite strain based on a neo-Hookean hyperelastic model. The effect of hydraulic hysteresis is taken into account in the formulations developed in [Shahbodagh-Khan, Khalili, Esgandani (2015)] and [Pedroso (2015)] for unsaturated porous media. Dynamic strain localisation in saturated and partially saturated porous media was analyzed in [Zhang and Schrefler (2000)] with the use of a gradient plasticity model. Comparative studies on different plasticity models within the FE u - p formulation were performed in [Khoei, Azami, Haeri (2004)], and it was shown that, if a properly calibrated

constitutive model is employed, the numerical simulation can reproduce quantitatively the behavior of geomaterials and predict the mechanism of failure and the motion along the failure surfaces.

In addition to the abovementioned FEM-based formulations, attempts have also been made in applying other numerical techniques to model the multi-physical processes of porous media. For instance, [Prevost (2014)] developed a procedure to couple geomechanical models based on FEM to reservoir models based on FVM (Finite Volume Method), motivated by the fact that most existing reservoir simulators are based on a FVM implementation of the pressure equation. A formulation based on FDM (Finite Difference Method) is also developed recently in [Zhang, Pedroso, Li, Ehlers (2017)] for porous media modeling, where high computational efficiency is achieved, but the numerical scheme is restricted to regular mesh/grids.

2.2.2 Meshfree methods

Meshfree methods [Belytschko, Lu, Gu (1994); Liu, Jun, Zhang (1995); Chen, Pan, Wu, Liu (1996); Li, Liu (2004); Chen and Belytschko (2015); Chen, Hillman, Chi (2017a); Chen, Liu, et al (2017b)] can overcome several drawbacks that are inherently associated with FEM. For instance, the time-consuming mesh generation process and the computational errors induced by distorted or low quality meshes in FEM can be avoided in meshfree methods [Chen, Pan, Wu, Liu (1996)]. Additionally, with the flexibility of controlling the order of smoothness, continuity and locality, the meshfree approximation offers exceptional benefits for solving problems with moving discontinuities such as crack propagation [Belytschko, Lu, Gu, Tabbara (1995); Krysl, Belytschko (1999); Bordas, Rabczuk, Zi (2008)] and problems with high order differentiation such as shear band formation via gradient plasticity or damage material models [Chen, Wu,

Belytschko (2000); Chen, Zhang, Belytschko (2004)]. The attributes of meshfree methods make them very attractive in engineering practice, and therefore meshfree methods have been successfully applied to a range of engineering mechanics problems for which the use of conventional mesh-based methods present significant difficulties.

Several coupled meshfree formulations have been proposed for the porous media modeling, including the Element-Free Galerkin (EFG) method [Murakami, Kawabata, Aoyama (2000); Karim, Nogami, Wang (2002); Oliaei, Soga, Pak (2009); Shibata and Murakami (2011); Hua (2011); Samimi and Pak (2012)], the Radial Point Interpolation Method (RPIM) [Wang, Liu, Wu (2001); Wang, Liu, Lin (2002); Khoshghalb, Khalili (2010)] and the Smoothed Particle Hydrodynamics (SPH) method [Bui, Fukagawa, Sako, Ohno (2008)], which have shown the advantages of meshfree methods in producing more accurate solutions for coupled problems over the standard FEM. Recently, the Reproducing Kernel Particle Method (RKPM) has been extended to solve the poromechanics problems based on a sequentially coupled scheme with a stabilized staggered iteration procedure used in between different solvers [Xie and Wang (2014)]. Despite the abovementioned development, the amount of research work on meshfree methods for multiphase porous media modeling remains limited, and further exploration of the unique features of meshfree methods is deserved in order to develop a robust computational poromechanical formulation.

2.3 Challenges in Modeling Hydro-Mechanical Damage Processes

The hydro-mechanical damage phenomena in multiphase porous media occur in a number of geotechnical engineering applications from the safety analysis of slopes and dams to

the design of underground storage of toxic or radioactive waste, as well as the stimulation in low-permeable gas and oil reservoirs, to name a few. Therefore, a reliable and efficient method for simulating these damage processes is of great importance. However, despite the progress made in computational method development, several numerical issues still exist, which need to be addressed.

2.3.1 Inf-Sup stability constraint

When the u-p form of the poromechanics theory is employed, there is an additional requirement on the approximation space in the mixed formulation. In the low permeable or nearly undrained limit, a nearly incompressibility constraint on the solid deformation is yielded, and if the approximation spaces for the solid displacement and the fluid pressure are not chosen properly, poor numerical results in the form of spurious pressure oscillations will appear [Zienkiewicz, Chan, Pastor, Schrefler, Shiomi (1999)]. This spatial instability is caused by the violation of the Ladyzhenskaya-Babuška-Brezzi (LBB) condition (also called the inf-sup condition) [Babuska (1973); Brezzi (1974); Haga, Osnes, Langtangen (2012)].

To address this issue, finite elements with a stable approximation pair are often employed. For instance, [Zienkiewicz, Chan, Pastor, Schrefler, Shiomi (1999)] used quadratic basis functions for displacement and linear basis functions for pore pressure to satisfy inf-sup condition and maintain numerical stability for isothermal hydromechanics problems. [Jha and Juanes (2007)] have shown that linear displacement combined and piecewise constant pore pressure may also lead to stable solutions for isothermal poromechanics problems. Nevertheless, these mixed-order interpolations complicate the implementation and are usually computationally expensive due to the requirement of extra degrees of freedom and high order domain integration

schemes. On the other hand, the equal-order approximation is in practice quite attractive because of its simplicity and efficiency for solving large-scale problems, especially for modeling fractured reservoirs [de Borst, Rethore, Abellan (2006)]. To this end, various stabilization strategies have been proposed to achieve oscillation-free solutions with an equal-order u-p approximation, including the fractional step algorithm [Pastor, Li, Liu, Zienkiewicz, Quecedo (2000), Li, Han, Pastor (2003)], the Galerkin Least Squares formulation [Wan Durlafsky, Hughes, Aziz (2003)], the fluid pressure Laplacian method [Truty and Zimmermann (2006)], and the fluid pressure projection method [White, Borja (2008); Sun, Ostien, Salinger (2013); Sun (2015); Choo, Borja (2015)], etc. Among these different stabilization approaches, the pressure projection based method has been proposed for nearly incompressible finite elasticity [Chen and Pan (1996); Chen, Wu, Pan (1996); Chen, Yoon, Wang, Liu (2000)], stokes flow [Dohrmann and Bochev (2004); Bochev, Dohrmann, Gunzburger (2006)] and poromechanics [White, Borja (2008); Sun, Ostien, Salinger (2013); Sun (2015); Choo, Borja (2015)]. Compared to other stabilization techniques, the pressure projection method has several appealing features such as the avoidance of stress-recovery techniques or high-order derivatives of shape functions commonly used in the Petrov-Galerkin type methods [Wan, Durlafsky, Hughes, Aziz (2003)], and also the stability property of the time-integration scheme is not affected, unlike the fractional step algorithm [Pastor, Li, Liu, Zienkiewicz, Quecedo (2000), Li, Han, Pastor (2003)].

While most of the research work on stabilization for poromechanics problems has been focused on FEM, very few attempts have been made to address this issue in the context of meshfree methods. The work by Hua [Hua (2011)] showed that the fluid pressure oscillation can be avoided by adjusting the numbers of u and p field nodes in the EFG method, but it is not clear how an optimal distribution of the nodes can be designed for general cases. The stabilized

Petrov-Galerkin formulation has been employed by Xie et al. [Xie and Wang (2014)] to eliminate the pressure oscillation in the RKPM method; however, this method results in a non-symmetric system matrix and requires calculation of high-order derivatives of meshfree shape functions which is time consuming.

2.3.2 Fracture modeling

Despite considerable advances made in fracture modeling methods, computational difficulties remain arising when growing fractures with complicated patterns need to be modeled, e.g., in hydraulic fracturing where many fractures exist and interact in a multiphase porous medium. In general, two main approaches exist for fracture modeling, namely the discrete crack approaches and the smeared crack approaches. The first class of methods includes adaptive re-meshing [Swenson and Ingraffea (1988); Rangarajan et al. (2014)], interface element insertion [Xu and Needleman (1994); Truster (2016)], embedded strong discontinuity [Belytschko et al. (1988); Simo et al. (1993); Jir ásek (2000); Oliver et al. (2014)], partition of unity-based enrichment [Belytschko and Black (1999); Mo ěs et al. (1999); Bordas et al. (2008)], and visibility/diffraction criterion [Organ et al. (1996); Krysl and Belytschko (1999)]. The second class of methods are formulated upon the smeared crack approaches using fixed and rotated crack models [Jir ásek and Zimmermann (1998a); Weihe et al. (1998)], continuum damage models [Pijaudier-Cabot and Bažant (1987); Peerlings et al. (1996); de Borst (2002); Cervera and Chiumenti (2006a); Cervera and Chiumenti (2006b); Jir ásek and Bauer (2012); de Borst and Verhoosel (2016)], and phase field models [Miehe et al. (2010); Borden et al. (2014); Ambati et al. (2015)], to name a few.

2.3.2.1 Discrete crack approaches

The discrete crack approaches usually consider continuous crack surfaces, and represent crack path by using level sets [Moës et al. (2002); Gravouil et al. (2002)] or other surface tracking techniques [Oliver et al. (2014); Jäger et al. (2008); Parvaneh and Foster (2016)]. However, fracture surfaces in quasi-brittle geomaterials are typically discrete and non-smooth, and they can evolve into irregular patterns such as crack branching and merging, making surface tracking techniques ineffective. By relaxing the crack path continuity requirement, alternative methods have been developed with the goal to model complicated fracture phenomena in a simplified way. For instance, the inter-element separation and cohesive interface element methods [Xu and Needleman (1994)] offer the flexibility in modeling crack growth along arbitrary finite element edges without any surface tracking procedures. However, the predicted crack patterns of these methods can be sensitive to the shape and orientation of the adopted finite element mesh. In the Cracking Particle Method (CPM) [Rabczuk and Belytschko (2004)], a set of crack segments located at nodal positions are used to describe the overall fracture surfaces. The simplicity and effectiveness of this idea has been studied in both Finite Element Method (FEM) [Remmers et al. (2003); de Borst et al. (2004); de Borst et al. (2006); Song and Belytschko (2009)] and Element Free Galerkin (EFG) method [Rabczuk and Belytschko (2004); Rabczuk and Belytschko (2007); Rabczuk et al. (2010); Rabczuk (2013)], although the latter meshfree discretization is more natural for the particle-based crack models. Nevertheless, similar to other discrete crack models, the strong discontinuities introduced at the cracked particles require subdividing quadrature cells associated with crack segments, modifying mesh topology or nodal neighbor list, or adding additional nodal degrees of freedom, leading to a greater degree of computational complexity.

2.3.2.2 Smearred crack approaches

Another type of fracture modeling introduces smearing of the sharp discontinuities over a finite domain, and the cracking effects are represented through a softening stress-strain law, which are in general called the smeared crack models [Weihe et al. (1998); de Borst (2002); de Borst et al. (2004); Jir ásek (2011)]. Compared to the discrete crack models, the smeared crack models offer the possibility of capturing a large set of complicated cracks in a simplified manner without dealing with many strong discontinuities. However, it has been observed that, when strain softening is considered in a continuum model, numerical results can become highly sensitive to the discretization (i.e., element size in FEM or nodal distance in meshfree methods). To restore the objectivity of numerical solutions, various regularization methods have been proposed. For instance, the nonlocal regularization methods [Pijaudier-Cabot and Bažant (1987); Peerlings et al. (1996); Miehe et al. (2010); Ambati et al. (2015); de Borst and Verhoosel (2016)] show promising performance, but these methods require fine meshes in cracking regions resulting in high computational cost [Heister et al. (2015)]. Besides, when the gradient type damage models [Peerlings et al. (1996); de Borst et al. (2016)] or the phase field models [Miehe et al. (2010); Borden et al. (2014); Ambati et al. (2015)] are adopted, an additional global equation coupled with the momentum equation needs to be solved for the nonlocal field variables at every time step. Chen et al. [Chen et al. (2004)] proposed a meshfree formulation to approximate the high order strain gradients by using the implicit gradient reproducing kernel conditions, but high order basis functions are required. Other issues with nonlocal models, which deserve further investigation, include the spurious initiation and growth of damage [Simone et al. (2004); Giry et al. (2011); Triantafyllou et al. (2014); Desmorat et al. (2015); Poh and Sun (2017)] and physically unjustified wave dispersion and localization properties of some nonlocal

models [Di Luzio and Bažant (2005); Bažant et al. (2016)].

A different remedy to the mesh dependency issue of smeared crack models is based on an appropriate adjustment of the local constitutive law without using nonlocal operators. For example, the crack band approach [Bažant and Oh (1983); Cervera and Chiumenti (2006a); Cervera and Chiumenti (2006b); Jir ásek and Bauer (2012)] rescales the post-peak part of the stress-strain law to adjust the bulk energy dissipation of finite elements to be consistent with the fracture energy dissipated during the fracturing process. A major advantage of this approach is that the adopted constitutive model remains local (versus the ‘nonlocal theories’), which allows the employment of many well-developed constitutive models in a unified manner. Nevertheless, it is found that the numerical solutions of standard crack band FEM can still show pathological mesh sensitivity when the mesh is not aligned with the crack propagation direction [Bažant and Lin (1988); Cervera and Chiumenti (2006a); Cervera and Chiumenti (2006b)]. In addition, the effectiveness of the regularization can be affected by both the finite element shape and domain integration schemes, thus it is not always straightforward to ensure objective energy dissipation [Jir ásek and Bauer (2012)].

2.3.2.3 Methods for hydraulic fracture simulation

There have been a number of numerical methods developed for the simulation of the hydraulic fracturing process. [Boone and Ingraffea (1990)] proposed one of the earliest computational scheme that enables staggered data transferring between a finite difference fluid flow solver and an FEM geo-mechanical solver, where crack propagation is modeled with interface elements along finite element edges. [Segura and Carol (2008); Carrier and Granet (2012)] developed a zero-thickness interface elements that have additional degrees of freedom to

take into account the hydro-mechanical coupling effects on crack propagation. These cohesive elements can be used to mesh the predicted fracture path, while usual volumetric elements can be used to mesh the neighboring porous medium; however, the fracture path has to be postulated a priori, which is a limitation of these approaches.

The re-meshing technique in conjunction with interface elements has been introduced by some researchers [Schrefler et al. (2006); Secchi et al. (2012); Fu et al. (2013)] to model the advancing cohesive cracks in a porous medium, which alleviates the restriction of fixed crack paths but at the expense of high computational cost and errors due to data projection between successive meshes.

Within the X-FEM (Extended Finite Element Method) framework, [de Borst, R ́thor ́ & Abellan (2006b); R ́thor ́ de Borst, & Abellan (2007); R ́thor ́ de Borst & Abellan (2008)] developed a hydro-mechanical coupled X-FEM formulation for the fluid flow in fractured porous media, which allows for the modeling of fluid filled cracks in arbitrary locations, irrespective of the structure of the underlying finite element mesh. Recently, the hydro-mechanical coupled X-FEM was further extended to consider finite strain effects [Irzal et al. (2013)], cohesive crack propagation [Mohammadnejad and Khoei (2013); Khoei et al. (2014)]. In addition, [Gupta and Duarte (2014)] developed an h-adaptive version of X-FEM formulation that can effectively refine the mesh near crack fronts for three-dimensional modeling of pressurized fracture propagation, while the hydro-mechanical coupling in porous geo-materials are neglected.

The aforementioned approaches all fall within the discrete crack modeling category, which represents cracks as strong discontinuities in the kinetic field and thus an approximation field that can dynamically align with moving discontinuities is required, which is achieved either

by continuously re-constructing the spatial discretization ('re-meshing' for finite element methods or 'visibility criterion' for meshfree methods), or by enriching the approximating space with discontinuous basis functions (e.g., X-FEM or enriched meshfree methods). Although the enrichment method enables the simulation of crack propagation on a fixed spatial discretization, the number of degrees of freedom increase during the simulation, and accordingly the domain integration cells crossed by cracks also need to be cut into sub-cells that are conforming to the crack surface. Therefore, the discrete crack model-based methods can become highly cumbersome for problems involving a large number of growing cracks, and additional difficulties may arise when crack branching and intersection needs to be considered. For instance, the standard Heaviside function commonly adopted in the enrichment scheme cannot be used directly for situations where cracks branch or intersect.

Therefore, recently there is an increasing trend to simulate hydraulic fracturing via the smeared crack models. This is due to the fact that smeared crack models circumvent the numerical difficulties related to moving discontinuities and allow effective handling of complex fracture patterns, and thus it has the potential to enable a large scale 3-D simulation. A coupled hydro-mechanical finite element model is developed by [Li et al. (2012)], where a damage mechanics model is used for the strength and stiffness degradation, and a stress and deformation dependent permeability is used for the fractured saturated porous materials. With this numerical scheme, progressive failure and associated fluid flow in rocks are modeled, as well as the complex cracking patterns such as branching, turning, and twisting of 3D fracture surfaces. However, the damage models adopted in [Li et al. (2012)] suffer from mesh sensitivity and thus the numerical solution may not converge as the discretization is refined. Some recent attempts have been made to simulate hydraulic fractures using the phase-field method [Wheeler et al.

(2014); Lee, Wheeler, Wick. (2016); Miehe, Mauthe, Teichtmeister (2015); Mauthe and Miehe (2017); Ehlers and Luo (2017)], which shares similarities with non-local gradient damage models. These methods are based on non-local type regularization technique and are quite effective in eliminating mesh dependency issues. However, these methods require solving a global phase field evolution equation coupled with the momentum/mass conservation equations. Moreover, the length scale parameters of phase field/non-local damage models still need further physical justification and calibration, and meanwhile they require very fine meshes to resolve the length scale parameters in the computation, thus the resulting numerical scheme is quite expensive especially for large-scale, hydro-mechanically coupled engineering problems.

2.3.3 Post-failure analysis of landslides

2.3.3.1 Mesh distortion issues in mesh-based methods

The ultimate impact of landslides depends not only on the failure initiation stage but also the post-failure process, so the run-out analysis is of great importance in landside risk assessment and mitigation design [McDougall (2016)]. However, despite the successful application of finite element/finite difference methods in predicting the onset of slope failures [Griffiths and Lane (1999); Huang and Jia (2009); Wei, Cheng, Li (2009); Wei and Cheng (2010)], these mesh-based methods often become ineffective for post-failure analysis due to mesh dependency limitations. Even if the initial mesh is carefully constructed to ensure every element is well-shaped, severe mesh distortions may eventually arise in the simulation of large deformation process. Unfortunately, the finite element approximation can no longer be built with the low-quality mesh, and the simulation has to be either terminated or continued with tedious re-meshing procedures [Belytschko, Liu, Moran, Elkhodary (2013)]. Therefore, the mesh distortion issue severely limits

the applicability of conventional numerical methods in post-failure analysis of multiphase porous media.

2.3.3.2 Meshfree methods for landslide modeling

Unlike conventional mesh-based methods, the meshfree methods have been proven to be well suited for modeling large deformation of solids, including the material separation and flow-like behavior occurred in the landslide processes, as they can naturally avoid computational difficulties associated with distorted or low-quality meshes [Chen, Pan, Wu, Liu (1996); Chen, Hillman, Chi (2017a)].

Recently, [Abe, Soga, Bandara 2013] and [Bandara and Soga 2015] developed a numerical procedure based on material point method (MPM) to solve coupled hydro-mechanical problems that undergo large deformation in saturated soils, where one single 2D Eulerian background mesh consisted of quadrilateral finite elements is adopted in conjunction with two sets of Lagrangian material points representing the soil skeleton and pore water, respectively. Later, [Bandara, Ferrari, Laloui (2016)] implemented the partially saturated condition in the hydro-mechanical MPM formulation, and proposed a special boundary treatment that switches the surface boundary conditions between Dirichlet and Neumann boundary conditions, depending on the saturation levels of the slopes subjected to rainfall infiltration. A comprehensive review of recent developments of MPM for landslide simulation can be found in [Soga et al. (2015)] and [Alonso, Yerro, Pinyol (2015)]. The smoothed particle hydrodynamics (SPH) method, on the other hand, has also been applied to investigate the failure mechanisms of saturated soil slopes [Bui and Fukagawa (2013)], earthquake-induced landslides [Huang et al. (2012); Dai et al. (2014); Huang and Dai (2014)], and rainfall-induced landslides [Zhang and

Maeda (2014)]. Despite of the simplicity of the SPH formulation, a number of numerical difficulties exist [Sweple et al. (1996); Monaghan (2000)], such as lack of linear consistency, tensile instability and inaccurate gradient estimate for stress calculation, which all require further improvements.

2.3.3.3 Domain integration techniques in meshfree methods

Despite the promising capabilities of meshfree methods for post-failure analysis of landslides, some critical numerical issues remain. One of such challenges is the domain integration technique. While Gauss quadrature rule has been commonly used in meshfree methods for the domain integration of weak form, considerable integration errors could be generated since the meshfree approximation functions are in general of rational type with often complicated overlapping support structures [Dolbow and Belytschko (1999)], and a very high order quadrature rule has to be adopted to achieve integration accuracy, which is computationally expensive. Methods such as direct nodal integration (DNI), on the other hand, could lead to instability due to rank deficiency, and also yields poor accuracy and low convergence rates [Beissel and Belytschko (1996)]. To simultaneously attain efficiency, accuracy and also stability in nodal integration, the stabilized conforming nodal integration (SCNI) method has been proposed by Chen et al. [Chen, Wu, Yoon, You (2001); Chen, Yoon, Wu (2002)] which achieves high accuracy and optimal convergence associated with approximation spaces with linear completeness. The generalization of SCNI for 2nd order bases [Duan, Li, Zhang, Wang, Gao (2012)] and for arbitrary order bases by a variational consistency condition [Chen, Hillman, Rüter (2013)] have also been proposed.

Although superior performance of SCNI has been shown in a wide range of applications,

it could become a prohibitively expensive scheme for problems involving extremely large deformation, for which conforming nodal integration zones have to be re-constructed as the semi-Lagrangian meshfree shape functions are re-evaluated when material damage and separation occurs. One way to circumvent this inconvenience is to relax the conforming condition on the smoothing zones, but the resulting quadrature scheme called stabilized non-conforming nodal integration (SNNI) violates the integration constraints [Chen, Wu, Yoon, You (2001); Chen, Hillman, Rüter (2013)]. To enhance the accuracy of SNNI and other integration schemes, the variationally consistent integration correction method has been proposed by [Chen, Hillman, Rüter (2013)], of which the key idea is to enforce arbitrary order consistency conditions to be met by modifying test functions. Nevertheless, it was found that low-energy modes can appear in SCNI or variationally consistent SNNI (VC-SNNI) based solutions, so additional stabilization is required. To this end, the modified stabilized conforming nodal integration (MSCNI) and modified stabilized non-conforming nodal integration (MSNNI) methods [Puso, Chen, Zywick, Elmer (2008)] have been developed, for which a penalty-type stabilization term involving shape function gradients evaluated at sub-cells of nodal integration zones is added to the discrete equations. As a number of additional shape function evaluation points in nodal sub-cells are needed to provide the necessary stabilization in MSNNI, the associated computational cost is very high when the semi-Lagrangian meshfree approximation [Chen and Wu (2007)] is adopted, which requires the shape functions to be re-evaluated at all the evaluation points frequently. [Hillman and Chen (2016)] introduced the naturally stabilized nodal integration method (NSNI) into the semi-Lagrangian reproducing kernel formulation, which can significantly speed up the computation by employment of implicit reproducing kernel gradients, minimal number of stabilization points and the avoidance of MSNNI type sub-cells. Although

integration techniques have been studied intensively, research on proper integration techniques for mixed formulations is rare and therefore deserves investigation.

Consider a porous medium occupying a domain Ω with boundary Γ as shown in Figure 3.1. According to the poromechanics theory [Biot (1941), Coussy (2004)], all phases are present at every point at the same time. As a result, the equations governing the deformation of a porous solid saturated with fluid can be derived from the principles of momentum and mass conservation of the mixture, which can be expressed as

$$\nabla \cdot (\boldsymbol{\sigma}'' - \alpha p \mathbf{I}) + \rho \mathbf{g} = \mathbf{0} \quad (3.1)$$

$$\alpha \nabla \cdot \frac{\partial \mathbf{u}}{\partial t} + \nabla \cdot \mathbf{q}_f + \frac{1}{Q} \frac{\partial p}{\partial t} = 0 \quad (3.2)$$

along with the following boundary conditions:

$$\mathbf{u} = \bar{\mathbf{u}} \quad \text{on } \Gamma_u \quad (3.3)$$

$$\mathbf{n}_\Gamma \cdot (\boldsymbol{\sigma}'' - \alpha p \mathbf{I}) = \bar{\mathbf{t}} \quad \text{on } \Gamma_t \quad (3.4)$$

$$p = \bar{p} \quad \text{on } \Gamma_p \quad (3.5)$$

$$-\mathbf{n}_\Gamma \cdot \mathbf{k}_f \cdot (\nabla p - \rho_f \mathbf{g}) = \mathbf{n}_\Gamma \cdot \bar{\mathbf{q}}_f \quad \text{on } \Gamma_q \quad (3.6)$$

and the initial conditions at time $t=0$:

$$\mathbf{u} = \mathbf{u}_0, \quad p = p_0 \quad (3.7)$$

where \mathbf{u} and p represent the solid displacement and the fluid pressure, respectively; $\boldsymbol{\sigma}''$ is

the effective stress, with the sign convention for tensile effective stress $\boldsymbol{\sigma}''$ and compressive fluid pressure p as positive, and the term $(\boldsymbol{\sigma}'' - \alpha p \mathbf{I})$ represents the total stress in the porous media; \mathbf{I} is a second-order identity tensor; $\rho = n_f \rho_f + (1 - n_f) \rho_s$ is the averaged mass density, in which n_f is the volume fraction of the fluid phase, often referred to as porosity, and ρ_s and ρ_f are the mass densities of the solid and fluid phases, respectively; \mathbf{g} is the gravity acceleration; the fluid storage coefficient is defined as $1/Q = (\alpha - n_f)/K_s + n_f/K_f$, in which Q is the Biot compressibility modulus, $\alpha = 1 - K/K_s$ is the Biot coefficient, K_s and K_f are the averaged bulk modulus of the solid grains and fluid, respectively, and $K = E/[3(1 - 2\nu)]$ is the drained bulk modulus of the overall solid skeleton, where E and ν are Young's modulus and Poisson's ratio of the dry porous matrix, respectively; \mathbf{q}_f is the fluid flow flux relative to the solid skeleton; \mathbf{n}_Γ is the unit outer normal vector of the boundary Γ , Γ_u and Γ_p are the essential boundaries with imposed solid displacement and fluid pressure, respectively, and Γ_t and Γ_q are the natural boundaries with imposed traction and fluid outflow flux, respectively, where $\Gamma_u \cap \Gamma_t = \Gamma_p \cap \Gamma_q = \emptyset$ and $\Gamma_u \cup \Gamma_t = \Gamma_p \cup \Gamma_q = \Gamma$; and the effective stress $\boldsymbol{\sigma}''$ can be defined through the constitutive relationship as follows

$$\boldsymbol{\sigma}'' = \mathbf{C} : \boldsymbol{\varepsilon} \quad (3.8)$$

where \mathbf{C} is the drained elastic modulus tensor of the solid skeleton, and $\boldsymbol{\varepsilon}$ is the strain tensor, defined as the symmetric part of the solid displacement gradient:

$$\boldsymbol{\varepsilon} = \nabla^s \mathbf{u} = \frac{1}{2} (\nabla \mathbf{u} + \nabla \mathbf{u}^T) \quad (3.9)$$

The barotropic fluid characterized by the fluid pressure field p is considered in the following discussions, and the fluid flow \mathbf{q}_f is then defined by the Darcy's law:

$$\mathbf{q}_f = -\mathbf{k}_f \cdot (\nabla p - \rho_f \mathbf{g}) \quad (3.10)$$

where $\mathbf{k}_f = \mathbf{k}_h / \gamma_f$ is the permeability tensor, in which \mathbf{k}_h is the hydraulic conductivity tensor and γ_f is the specific weight of the fluid. Note that the permeability tensor can be alternatively expressed as the ratio of the so-called intrinsic permeability tensor to the dynamic viscosity, and in general it can evolve with the change of void ratio, micro-cracks density and distribution, etc. For simplicity, here \mathbf{k}_f is considered to be constant and isotropic, i.e., $\mathbf{k}_f = k_f \mathbf{I}$. Substituting equation (3.10) into equation (3.2), and combining with equation (3.1), the classical u - p form of the poromechanics governing equations can be obtained, which are employed in the present study.

3.1.2 Weak form

To arrive at the weak form, two spaces of trial functions for both solid displacement and fluid pressure fields in d -dimension are defined as

$$S_u = \left\{ \mathbf{u} : \Omega \rightarrow \mathbb{R}^d \mid \mathbf{u} \in [\mathbf{H}^1]^d, \mathbf{u} = \bar{\mathbf{u}} \text{ on } \Gamma_u \right\} \quad (3.11)$$

$$S_p = \left\{ p : \Omega \rightarrow \mathbb{R} \mid p \in H^1, p = \bar{p} \text{ on } \Gamma_p \right\} \quad (3.12)$$

The corresponding spaces of test functions are

$$V_u = \left\{ \boldsymbol{\eta}: \Omega \rightarrow \mathbb{R}^d \mid \boldsymbol{\eta} \in [\mathbf{H}^1]^d, \boldsymbol{\eta} = \mathbf{0} \text{ on } \Gamma_u \right\} \quad (3.13)$$

$$V_p = \left\{ \psi: \Omega \rightarrow \mathbb{R} \mid \psi \in \mathbf{H}^1, \psi = 0 \text{ on } \Gamma_p \right\} \quad (3.14)$$

The weak form statement of the problem in Section 3.1.1 is then to find $(\mathbf{u}, \mathbf{p}) \in S_u \times S_p$ such that for all $(\boldsymbol{\eta}, \psi) \in V_u \times V_p$,

$$L_1(\boldsymbol{\eta}; \mathbf{u}, \mathbf{p}) \equiv \int_{\Omega} (\nabla^s \boldsymbol{\eta} : \boldsymbol{\sigma}' - \alpha \mathbf{p} \nabla \cdot \boldsymbol{\eta}) \, d\Omega - \int_{\Gamma_t} \boldsymbol{\eta} \cdot \bar{\mathbf{t}} \, d\Gamma - \int_{\Omega} \boldsymbol{\eta} \cdot \rho \mathbf{g} \, d\Omega = 0 \quad (3.15)$$

$$L_2(\psi; \mathbf{u}, \mathbf{p}) \equiv \int_{\Omega} \alpha \psi \nabla \cdot \frac{\partial \mathbf{u}}{\partial t} \, d\Omega + \int_{\Omega} \psi \frac{1}{Q} \frac{\partial \mathbf{p}}{\partial t} \, d\Omega + \int_{\Omega} \nabla \psi \cdot \mathbf{k}_f \cdot \nabla \mathbf{p} \, d\Omega + \int_{\Gamma_q} \psi \mathbf{n}_{\Gamma} \cdot \bar{\mathbf{q}}_f \, d\Gamma - \int_{\Omega} \nabla \psi \cdot \mathbf{k}_f \cdot \rho_f \mathbf{g} \, d\Omega = 0 \quad (3.16)$$

3.2 Reproducing Kernel Mixed Formulation

3.2.1 Reproducing kernel approximation

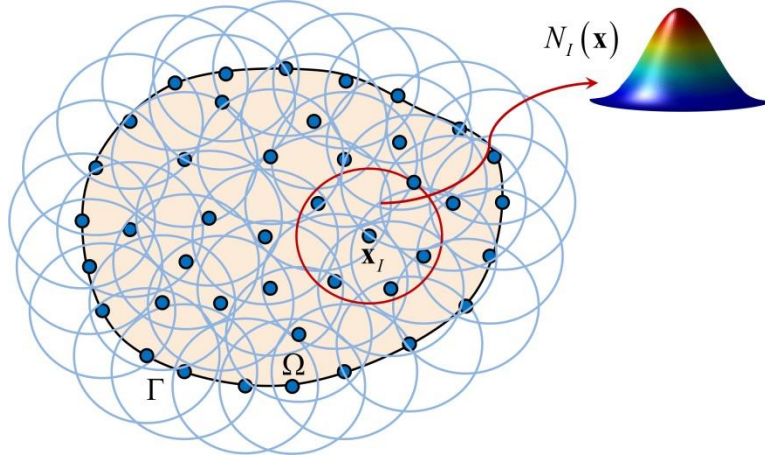


Figure 3.2 Illustration of a domain Ω discretized by meshfree particles and the reproducing kernel shape function $N_I(\mathbf{x})$ associated with node I

Let $\{\mathbf{x}_I, \mathbf{x}_I \in \Omega\}_{I=1}^{NP}$ be a set of nodes in the domain, \mathbf{x}_I is the position vector of node I , and NP is the total number of nodes. The discrete reproducing kernel approximation [Liu, Jun, Zhang (1995); Chen, Pan, Wu, Liu (1996)] of a function $f(\mathbf{x})$ in the domain Ω is as follows:

$$f^h(\mathbf{x}) = \sum_{I=1}^{NP} N_I(\mathbf{x}) f_I \quad (3.17)$$

where f_I is the coefficient, and $N_I(\mathbf{x})$ is the n^{th} order reproducing kernel shape function expressed as

$$N_I(\mathbf{x}) = C(\mathbf{x}; \mathbf{x} - \mathbf{x}_I) \Phi_a(\mathbf{x} - \mathbf{x}_I) \quad (3.18)$$

in the above equation, $C(\mathbf{x}; \mathbf{x} - \mathbf{x}_I)$ is a correction function, and $\Phi_a(\mathbf{x} - \mathbf{x}_I)$ is the kernel function that controls the locality and smoothness of the approximation, which is chosen to be the cubic spline function in the present study:

$$\Phi_a(\mathbf{x} - \mathbf{x}_I) = \begin{cases} 2/3 - 4s_I^2 + 4s_I^3 & \text{for } 0 \leq s_I \leq 1/2 \\ 4/3 - 4s_I + 4s_I^2 - 4/3 s_I^3 & \text{for } 1/2 < s_I \leq 1 \\ 0 & \text{for } s_I > 1 \end{cases} \quad (3.19)$$

where $s_I = \|\mathbf{x} - \mathbf{x}_I\|/a_I$, and a_I is the support size of node I . The correction function is defined as:

$$C(\mathbf{x}; \mathbf{x} - \mathbf{x}_I) = \mathbf{b}^T(\mathbf{x}) \mathbf{H}(\mathbf{x} - \mathbf{x}_I) \quad (3.20)$$

in which $\mathbf{H}(\mathbf{x} - \mathbf{x}_I)$ is a vector consisting of n^{th} order monomial basis functions:

$$\mathbf{H}^T(\mathbf{x} - \mathbf{x}_I) = [1, x - x_I, y - y_I, z - z_I, (x - x_I)^2, \dots, (z - z_I)^n] \quad (3.21)$$

and $\mathbf{b}(\mathbf{x})$ is the coefficient vector to be determined from the following n^{th} order discrete reproducing conditions:

$$\sum_{I=1}^{NP} N_I(\mathbf{x}) \mathbf{H}^T(\mathbf{x}_I) = \mathbf{H}^T(\mathbf{x}) \quad \text{or} \quad \sum_{I=1}^{NP} N_I(\mathbf{x}) \mathbf{H}^T(\mathbf{x} - \mathbf{x}_I) = \mathbf{H}^T(\mathbf{0}) \quad (3.22)$$

which leads to $\mathbf{b}(\mathbf{x})$ of the following form:

$$\mathbf{b}^T(\mathbf{x}) = \mathbf{H}^T(\mathbf{0}) \mathbf{A}^{-1}(\mathbf{x}) \quad (3.23)$$

where the moment matrix is defined as

$$\mathbf{A}(\mathbf{x}) = \sum_{I=1}^{NP} \mathbf{H}(\mathbf{x}-\mathbf{x}_I) \mathbf{H}^T(\mathbf{x}-\mathbf{x}_I) \Phi_a(\mathbf{x}-\mathbf{x}_I) \quad (3.24)$$

Combining equations (3.18), (3.20) and (3.23), the reproducing kernel shape function is obtained as

$$N_I(\mathbf{x}) = \mathbf{H}^T(\mathbf{0}) \mathbf{A}^{-1}(\mathbf{x}) \mathbf{H}(\mathbf{x}-\mathbf{x}_I) \Phi_a(\mathbf{x}-\mathbf{x}_I) \quad (3.25)$$

3.2.2 Reproducing kernel u - p approximation and discretization

Applying the reproducing kernel approximation to both the trial and test functions for the solid displacement and fluid pressure, we have

$$\mathbf{u}^h = \mathbf{N}^u \mathbf{U} = \sum_{I=1}^{NP} N_I \mathbf{U}_I, \quad \mathbf{p}^h = \mathbf{N}^p \mathbf{P} = \sum_{I=1}^{NP} N_I P_I \quad (3.26)$$

$$\boldsymbol{\eta}^h = \mathbf{N}^u \mathbf{c}^u = \sum_{I=1}^{NP} N_I \mathbf{c}_I^u, \quad \psi^h = \mathbf{N}^p \mathbf{c}^p = \sum_{I=1}^{NP} N_I c_I^p \quad (3.27)$$

where \mathbf{N}^u and \mathbf{N}^p are the matrices of reproducing kernel shape functions N_I using linear basis for displacement and pressure fields, respectively, and \mathbf{U} , \mathbf{P} , \mathbf{c}^u and \mathbf{c}^p are vectors containing the corresponding nodal coefficients. Substituting the approximation functions into equations (3.15) and (3.16), the following semi-discrete equations are obtained:

$$L_1(\boldsymbol{\eta}^h; \mathbf{u}^h, \mathbf{p}^h) \equiv \int_{\Omega} (\nabla^s \boldsymbol{\eta}^h : \boldsymbol{\sigma}'' - \alpha \mathbf{p}^h \nabla \cdot \boldsymbol{\eta}^h) \, d\Omega - \int_{\Gamma_t} \boldsymbol{\eta}^h \cdot \bar{\mathbf{t}} \, d\Gamma - \int_{\Omega} \boldsymbol{\eta}^h \cdot \boldsymbol{\rho} \mathbf{g} \, d\Omega = 0 \quad (3.28)$$

$$\begin{aligned}
L_2(\psi^h; \mathbf{u}^h, p^h) \equiv & \int_{\Omega} \alpha \psi^h \nabla \cdot \frac{\partial \mathbf{u}^h}{\partial t} d\Omega + \int_{\Omega} \psi^h \frac{1}{Q} \frac{\partial p^h}{\partial t} d\Omega + \\
& \int_{\Omega} \nabla \psi^h \cdot \mathbf{k}_f \cdot \nabla p^h d\Omega + \int_{\Gamma_q} \psi^h \mathbf{n}_{\Gamma} \cdot \bar{\mathbf{q}}_f d\Gamma - \int_{\Omega} \nabla \psi^h \cdot \mathbf{k}_f \cdot \rho_f \mathbf{g} d\Omega = 0
\end{aligned} \tag{3.29}$$

which leads to the following system of coupled matrix equations:

$$\mathbf{K}_{uu} \mathbf{U} - \mathbf{K}_{up} \mathbf{P} - \mathbf{F}^{ext} = \mathbf{0} \tag{3.30}$$

$$\mathbf{K}_{up}^T \frac{\partial \mathbf{U}}{\partial t} + \mathbf{K}_{pp}^{(s)} \frac{\partial \mathbf{P}}{\partial t} + \mathbf{K}_{pp}^{(H)} \mathbf{P} - \mathbf{Q}^{ext} = \mathbf{0} \tag{3.31}$$

where the matrices and vectors can be expressed as follows:

$$\text{Solid stiffness matrix} \quad \mathbf{K}_{uu} = \int_{\Omega} \mathbf{B}^{uT} \mathbf{D} \mathbf{B}^u d\Omega \tag{3.32}$$

$$\text{Coupling matrix} \quad \mathbf{K}_{up} = \int_{\Omega} \mathbf{B}^{uT} \alpha \mathbf{m} \mathbf{N}^p d\Omega, \tag{3.33}$$

$$\text{Compressibility matrix} \quad \mathbf{K}_{pp}^{(s)} = \int_{\Omega} \mathbf{N}^{pT} Q^{-1} \mathbf{N}^p d\Omega \tag{3.34}$$

$$\text{Permeability matrix} \quad \mathbf{K}_{pp}^{(H)} = \int_{\Omega} \mathbf{B}^{pT} \mathbf{k}_f \mathbf{B}^p d\Omega \tag{3.35}$$

$$\text{External force vector} \quad \mathbf{F}^{ext} = \int_{\Gamma_t} \mathbf{N}^{uT} \bar{\mathbf{t}} d\Gamma + \int_{\Omega} \mathbf{N}^{uT} \rho_f \mathbf{g} d\Omega \tag{3.36}$$

$$\text{External flow flux vector} \quad \mathbf{Q}^{ext} = - \int_{\Gamma_q} \mathbf{N}^{pT} \mathbf{n}_{\Gamma} \bar{\mathbf{q}}_f d\Gamma + \int_{\Omega} \mathbf{B}^{pT} \mathbf{k}_f \rho_f \mathbf{g} d\Omega \tag{3.37}$$

In the above equations, \mathbf{B}^u and \mathbf{B}^p are the standard gradient matrices associated with the

displacement and pressure approximation fields, respectively, \mathbf{D} is the matrix form of elastic material constants in the constitutive tensor \mathbf{C} , and $\mathbf{m} = [1 \ 1 \ 0]^T$ in equation (3.33).

3.2.3 Discrete equations

The backward Euler method is employed which ensures unconditional stability in the temporal discretization. If the problem is to be solved between an initial time t_0 and a final time t_f , a partition of the time interval is considered, resulting in a series of time increments $\Delta t_{n+1} = t_{n+1} - t_n$. Evaluating the semi-discrete equations (3.30) and (3.31) at time t_{n+1} and applying the following time marching scheme:

$$\left. \frac{\partial(\cdot)}{\partial t} \right|_{t_{n+1}} \cong \frac{\Delta(\cdot)_{n+1}}{\Delta t_{n+1}} = \frac{(\cdot)_{n+1} - (\cdot)_n}{\Delta t_{n+1}} \quad (3.38)$$

then the full discrete equations can be expressed as

$$\mathbf{K}_{uu} \mathbf{U}_{n+1} - \mathbf{K}_{up} \mathbf{P}_{n+1} - \mathbf{F}_{n+1}^{ext} = \mathbf{0} \quad (3.39)$$

$$\mathbf{K}_{up}^T \Delta \mathbf{U}_{n+1} + \mathbf{K}_{pp}^{(s)} \Delta \mathbf{P}_{n+1} + \Delta t \mathbf{K}_{pp}^{(H)} \mathbf{P}_{n+1} - \Delta t \mathbf{Q}_{n+1}^{ext} = \mathbf{0} \quad (3.40)$$

Finally, we obtain the following system of equations to solve at every time step:

$$\mathbf{J}_{n+1} \mathbf{X}_{n+1} = \mathbf{R}_{n+1} \quad (3.41)$$

where

$$\mathbf{X}_{n+1} = \begin{pmatrix} \mathbf{U}_{n+1} \\ \mathbf{P}_{n+1} \end{pmatrix} \quad (3.42)$$

$$\mathbf{J}_{n+1} = \begin{bmatrix} \mathbf{K}_{uu} & -\mathbf{K}_{up} \\ -\mathbf{K}_{up}^T & -\mathbf{K}_{pp}^{(S)} - \Delta t_{n+1} \mathbf{K}_{pp}^{(H)} \end{bmatrix} \quad (3.43)$$

$$\mathbf{R}_{n+1} = \begin{bmatrix} \mathbf{0} & \mathbf{0} \\ -\mathbf{K}_{up}^T & -\mathbf{K}_{pp}^{(S)} \end{bmatrix} \begin{pmatrix} \mathbf{U}_n \\ \mathbf{P}_n \end{pmatrix} + \begin{pmatrix} \mathbf{F}_{n+1}^{ext} \\ -\Delta t \mathbf{Q}_{n+1}^{ext} \end{pmatrix} \quad (3.44)$$

In the present study, the monolithic solution strategy is adopted by which the primary unknowns of the fully coupled equations are solved simultaneously. Alternatively, a staggered or sequential coupling scheme can be used, and then a relatively small system of equations is solved at each time before sharing its information with other solvers through iteration. However, unlike the monolithic scheme, it is non-trivial to fully capture the coupling effects by using staggered solvers and also stability and convergence difficulties may be encountered unless appropriate techniques are utilized [Xie and Wang (2014); Kim, Tchelepi, Juanes (2011)].

3.3 Fluid Pressure Projection for Meshfree Method with Nodal Integration

3.3.1 Pressure projection

When an equal-order approximation pair is adopted in the Bubnov-Galerkin approximation of the coupled problem described in previous sections, non-physical spatial oscillations can occur in the fluid pressure field when the porous medium is under nearly impermeable or undrained conditions. This problem is due to violation of the following discrete inf-sup condition [Babuska (1973); Brezzi (1974); Haga, Osnes, Langtangen (2012)]:

$$\sup_{\mathbf{u}^h \in S_u^h} \frac{\int_{\Omega} \mathbf{p}^h \nabla \cdot \mathbf{u}^h d\Omega}{\|\mathbf{u}^h\|_1} \geq C_0 \|\mathbf{p}^h\|_0 \quad \forall \mathbf{p}^h \in S_p^h \quad (3.45)$$

where C_0 is a positive constant independent of the numerical discretization. However, it has been found that equal-order approximation pairs indeed satisfy a weaker inf-sup condition [White and Borja (2008); Sun, Ostien, Salinger (2013)] expressed by

$$\sup_{\mathbf{u}^h \in S_u^h} \frac{\int_{\Omega} \mathbf{p}^h \nabla \cdot \mathbf{u}^h d\Omega}{\|\mathbf{u}^h\|_1} + \sum_{\Omega_I \in \Omega} C_1 \|\mathbf{p}^h - \Pi \mathbf{p}^h\|_{0, \Omega_I} \geq C_2 \|\mathbf{p}^h\|_0 \quad \forall \mathbf{p}^h \in S_p^h \quad (3.46)$$

where C_1 and C_2 are positive constants independent of the numerical discretization; Ω_I is a sub-domain associated with the spatial discretization, for example, it can be represented by an element domain in the finite element context; $\Pi \mathbf{p}^h$ is the L_2 projection of the fluid pressure approximation field onto a lower-order space by minimizing the following functional:

$$\Theta(\Pi \mathbf{p}^h)_{\Omega_I} = \|\mathbf{p}^h - \Pi \mathbf{p}^h\|_{L_2(\Omega_I)}^2 \quad (3.47)$$

For a linear approximation of the fluid pressure, we perform the projection to a constant field to yield

$$\Pi \mathbf{p}^h|_{\Omega_I} = \frac{1}{V_I} \int_{\Omega_I} \mathbf{p}^h \mathbf{1} \quad (3.48)$$

where V_I refers to the volume of the domain Ω_I in 3D or the area in 2D. Comparing equation (3.45) and (3.46), it can be observed that the term $C_1 \|\mathbf{p}^h - \Pi \mathbf{p}^h\|_{0, \Omega_I}$ can remedy the inherent

deficiency in the equal-order approximation pair. Based on this analogy, White and Borja [White, Borja (2008)] proposed to include a stabilization term to the bilinear finite element formulation in order to eliminate the spurious fluid pressure oscillation modes. Later, the finite element formulation using this fluid pressure projection method was further developed for large deformation poromechanical simulations [Sun, Ostien, Salinger (2013)], thermo-hydro-mechanical simulations [Sun (2015)] and the modeling of porous media with double porosity [Choo, Borja (2015)]. Similar schemes have previously been developed for stabilizing the numerical solutions of the Stokes equations [Dohrmann, Bochev (2004); Bochev, Dohrmann, Gunzburger (2006)], and for nearly incompressible elasticity problems [Chen and Pan (1996); Chen, Wu, Pan (1996); Chen, Yoon, Wang, Liu (2000)]. Along this line, the fluid pressure projection method is employed in the present study for the meshfree formulation for coupled poromechanics problems within the stabilized conforming nodal integration framework. As mentioned, an additional stabilization term is added to the variational equation (3.29) to correct the deficiency of the equal-order u - p approximation, leading to the following stabilized variational equation

$$\bar{L}_2(\psi^h; \mathbf{u}^h, p^h) \equiv L_2(\psi^h; \mathbf{u}^h, p^h) + \int_{\Omega} \varepsilon_f (\psi^h - \Pi \psi^h)(p^h - \Pi p^h) d\Omega = 0 \quad (3.49)$$

Since the reproducing kernel approximation is purely based on nodal information, i.e., there is no element domain as in the FEM context, a suitable L_2 projection operator needs to be defined. To be compatible with the stabilized conforming nodal integration (SCNI) framework to be described in the next section, we choose the SCNI nodal representative integration domain as the sub-domain Ω_I used for the operator Π . Following the same discretization procedure as introduced in previous sections, we can obtain the stabilized system of discrete equations at time

step n :

$$\bar{\mathbf{J}}_{n+1} \mathbf{X}_{n+1} = \bar{\mathbf{R}}_{n+1} \quad (3.50)$$

where

$$\bar{\mathbf{J}}_{n+1} = \begin{bmatrix} \mathbf{K}_{uu} & -\mathbf{K}_{up} \\ -\mathbf{K}_{up}^T & -\mathbf{K}_{pp}^{(S)} - \Delta t_{n+1} \mathbf{K}_{pp}^{(H)} - \Delta t_{n+1} \mathbf{S} \end{bmatrix} \quad (3.51)$$

$$\mathbf{S} = \int_{\Omega} \varepsilon_f \left[\mathbf{N}^p - \Pi \mathbf{N}^p \right]^T \left[\mathbf{N}^p - \Pi \mathbf{N}^p \right] d\Omega \quad (3.52)$$

As can be seen, the fluid pressure projection based stabilization only requires modification of the p - p block of the Jacobian with a symmetric matrix \mathbf{S} , and no stress-recovery techniques or second-order derivatives of the shape functions are needed as in the Petrov-Galerkin based stabilization approaches [Xie and Wang (2014); Wan, Durlofsky, Hughes, Aziz (2003)], and also the stability property of the time-integration scheme is not affected, unlike the fractional step algorithm [Pastor, Li, Liu, Zienkiewicz, Quecedo (2000); Li, Han, Pastor (2003)]. An estimation of the stabilization parameter ε_f following Sun et al. [Sun, Ostien, Salinger (2013)] is given as follows:

$$\varepsilon_f = \frac{1}{M'} \left\langle 1 - 3 \frac{c_v \Delta t}{h^2} \right\rangle \left(1 + \tanh \left(2 - 12 \frac{c_v \Delta t}{h^2} \right) \right) \quad (3.53)$$

where

$$c_v = k_f M' = \frac{k_f (K + 4G/3)}{(K + 4G/3)/Q + \alpha^2} \quad (3.54)$$

in which $\langle \cdot \rangle$ is the Macaulay bracket, and the Biot modulus is defined as $Q = K_s K_f / [K_f (\alpha - n_f) + K_s n_f]$, k_f is the permeability parameter, α is Biot's coefficient, n_f is the porosity, G is the shear modulus, K , K_s and K_f are the averaged bulk modulus of the solid skeleton, solid grains and fluid, respectively, as defined in Section 2.1, and h is a characteristic length depending on the numerical discretization, for which we adopt a simple definition as $h = \sqrt{A_I}$ for two dimensional problem, where A_I is the area of the representative domain of node I as discussed in next section. It can be seen from equation (3.53), as the permeability becomes high, the parameter ε_f will approach to zero by construction, therefore over diffusion due to stabilization would be avoided automatically. This property of the adopted stabilization parameter makes the projection method suitable for solving problems under different drainage conditions, as to be shown in the numerical examples in Section 3.4.

3.3.2 Stabilized conforming nodal integration for pressure projection

The domain integration for the discrete equations introduced previously can be performed by using the Gauss integration method. However, in order to obtain accurate, convergent solutions, expensive high order Gauss integration is required. Stabilized conforming nodal integration method, on the other hand, achieves high accuracy and optimal convergence, and is also computationally efficient [Chen, Wu, Yoon, You (2001); Chen, Yoon, Wu (2002)]. In this method, shape function gradients are smoothed over conforming nodal representative domains,

and domain integration is performed at each node. The smoothed gradient of the shape functions are defined as

$$\begin{aligned}
\tilde{\nabla} N_I(\mathbf{x}_L) &\equiv \frac{1}{A_L} \int_{\Omega_L} \nabla N_I(\mathbf{x}) \, d\Omega \\
&= \frac{1}{A_L} \int_{\Gamma_L} N_I(\mathbf{x}) \mathbf{n}(\mathbf{x}) \, d\Gamma \\
&\cong \frac{1}{A_L} \sum_{G=1}^{NG} N_I(\tilde{\mathbf{x}}_L^G) \mathbf{n}(\tilde{\mathbf{x}}_L^G) l_G
\end{aligned} \tag{3.55}$$

where $\tilde{\nabla}$ is the smoothed gradient operator and $\tilde{\nabla} N_I(\mathbf{x}_L)$ denotes the smoothed $\nabla N_I(\mathbf{x})$ associated with nodal point \mathbf{x}_L , Γ_L and Γ_G refer to the whole boundary and the G^{th} boundary segment of the nodal representative domain Ω_L , respectively, $A_L = \int_{\Omega_L} d\Omega$, $l_G = \int_{\Gamma_G} d\Gamma$, $\mathbf{n}(\mathbf{x})$ is the outer unit normal to Γ_L , and NG is the total number of gradient smoothing evaluation points $\tilde{\mathbf{x}}_L^G$ which rest at the centroids of the boundary segments. The nodal representative domains can be constructed by Delaunay triangulation or Voronoi diagram, as shown in Figure 3.3.

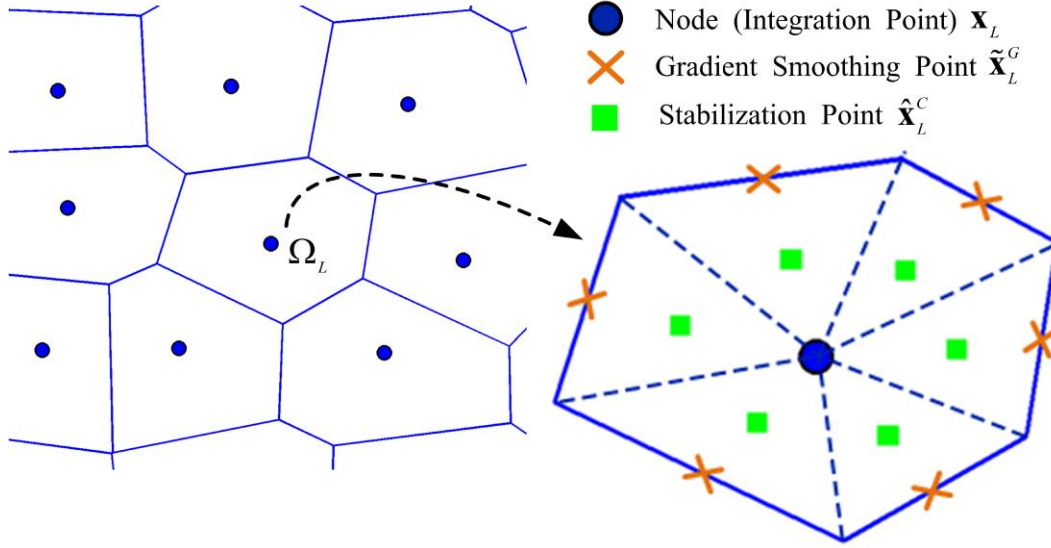


Figure 3.3 Nodal representative domain for stabilized conforming nodal integration (SCNI) and fluid pressure projection (FPP)

SCNI avoids rank deficiency in direct nodal integration, however spurious low-energy modes may still appear in the solution. Puso et al. [Puso, Chen, Zywick, Elmer (2008)] proposed to use more ‘stress points’ for stabilization which leads to the following expressions of equations (3.32)-(3.35) and (3.52) as a stabilized nodal integration:

$$\begin{aligned}
 [\mathbf{K}_{uu}]_{IJ} &= \int_{\Omega} \mathbf{B}_I^{uT} \mathbf{D} \mathbf{B}_J^u d\Omega \\
 &\cong \sum_{L=1}^{NP} \left\{ \tilde{\mathbf{B}}_I^{uT}(\mathbf{x}_L) \mathbf{D} \tilde{\mathbf{B}}_J^u(\mathbf{x}_L) A_L \right. \\
 &\quad \left. + \varepsilon_p \sum_{C \in I_L} \left[\tilde{\mathbf{B}}_I^u(\mathbf{x}_L) - \tilde{\mathbf{B}}_I^u(\hat{\mathbf{x}}_L^C) \right]^T \mathbf{D} \left[\tilde{\mathbf{B}}_J^u(\mathbf{x}_L) - \tilde{\mathbf{B}}_J^u(\hat{\mathbf{x}}_L^C) \right] A_C \right\}
 \end{aligned} \tag{3.56}$$

$$\begin{aligned}
 [\mathbf{K}_{up}]_{IJ} &= \int_{\Omega} \mathbf{B}_I^{uT} \alpha \mathbf{m} \mathbf{N}_J^p d\Omega \\
 &\cong \sum_{L=1}^{NP} \tilde{\mathbf{B}}_I^{uT}(\mathbf{x}_L) \alpha \mathbf{m} \mathbf{N}_J^p(\mathbf{x}_L) A_L
 \end{aligned} \tag{3.57}$$

$$\begin{aligned}
\left[\mathbf{K}_{pp}^{(S)} \right]_{IJ} &= \int_{\Omega} \mathbf{N}_I^{pT} \mathcal{Q}^{-1} \mathbf{N}_J^p d\Omega \\
&\cong \sum_{L=1}^{NP} \left\{ \mathbf{N}_I^{pT}(\mathbf{x}_L) \mathcal{Q}^{-1} \mathbf{N}_J^p(\mathbf{x}_L) A_L \right. \\
&\quad \left. + \varepsilon_p \sum_{C \in T_L} \left[\mathbf{N}_I^p(\mathbf{x}_L) - \mathbf{N}_I^p(\hat{\mathbf{x}}_L^C) \right]^T \mathcal{Q}^{-1} \left[\mathbf{N}_I^p(\mathbf{x}_L) - \mathbf{N}_I^p(\hat{\mathbf{x}}_L^C) \right] A_C \right\}
\end{aligned} \tag{3.58}$$

$$\begin{aligned}
\left[\mathbf{K}_{pp}^{(H)} \right]_{IJ} &= \int_{\Omega} \mathbf{B}_I^{pT} \mathbf{k}_f \mathbf{B}_J^p d\Omega \\
&\cong \sum_{L=1}^{NP} \left\{ \tilde{\mathbf{B}}_I^{pT}(\mathbf{x}_L) \mathbf{k}_f \tilde{\mathbf{B}}_J^p(\mathbf{x}_L) A_L \right. \\
&\quad \left. + \varepsilon_p \sum_{C \in T_L} \left[\tilde{\mathbf{B}}_I^p(\mathbf{x}_L) - \tilde{\mathbf{B}}_I^p(\hat{\mathbf{x}}_L^C) \right]^T \mathbf{k}_f \left[\tilde{\mathbf{B}}_J^p(\mathbf{x}_L) - \tilde{\mathbf{B}}_J^p(\hat{\mathbf{x}}_L^C) \right] A_C \right\}
\end{aligned} \tag{3.59}$$

$$\begin{aligned}
\left[\mathbf{S} \right]_{IJ} &= \int_{\Omega} \varepsilon_f \left[\mathbf{N}_I^p - \Pi \mathbf{N}_I^p \right]^T \left[\mathbf{N}_J^p - \Pi \mathbf{N}_J^p \right] d\Omega \\
&\cong \sum_{L=1}^{NP} \left\{ \varepsilon_f(\mathbf{x}_L) \left[\mathbf{N}_I^p(\mathbf{x}_L) - \Pi \mathbf{N}_I^p(\mathbf{x}_L) \right]^T \left[\mathbf{N}_J^p(\mathbf{x}_L) - \Pi \mathbf{N}_J^p(\mathbf{x}_L) \right] A_L \right. \\
&\quad \left. + \varepsilon_p \varepsilon_f(\mathbf{x}_L) \sum_{C \in T_L} \left[\mathbf{N}_I^p(\mathbf{x}_L) - \Pi \mathbf{N}_I^p(\hat{\mathbf{x}}_L^C) \right]^T \left[\mathbf{N}_J^p(\mathbf{x}_L) - \Pi \mathbf{N}_J^p(\hat{\mathbf{x}}_L^C) \right] A_C \right\}
\end{aligned} \tag{3.60}$$

where $\tilde{\mathbf{B}}_I^u$ and $\tilde{\mathbf{B}}_I^p$ are the smoothed gradient matrices associated with $\tilde{\nabla} N_I$, T_L is the set of subcells C associated with each node L , A_C is the area of the C^{th} subcell which satisfies

$A_L = \sum_{C \in T_L} A_C$, and the stabilization points $\hat{\mathbf{x}}_L^C$ rest at the centroids of the subcells as shown in

Figure 3.3. The expressions in equations (3.56)-(3.60) are considered to be of the nodal integration type since material parameters and state variables are calculated and stored at the nodal points \mathbf{x}_L only. Compared to direct nodal integration, the minor extra effort required in SCNI is to compute the shape functions and their smoothed gradients at a few stabilization points.

The stabilization parameter $\varepsilon_p = 1$, as suggested by [Puso, Chen, Zywick, Elmer (2008)], is

used in all the numerical examples in the present study.

Furthermore, recalling the L_2 projection operator Π defined in equation (3.48), we can see that all the pressure projection terms appearing in equation (3.60) indeed can be computed within the same nodal integration framework in a straightforward way:

$$\Pi \mathbf{N}_I^p(\mathbf{x}_L) = \frac{1}{A_L} \int_{\Omega_L} \mathbf{N}_I^p d\mathbf{x} \cong \frac{1}{A_L} \sum_{C \in \mathcal{I}_L} \mathbf{N}_I^p(\hat{\mathbf{x}}_L^C) A_C \quad (3.61)$$

$$\Pi \mathbf{N}_I^p(\hat{\mathbf{x}}_L^C) = \frac{1}{A_C} \int_{\Omega_C} \mathbf{N}_I^p d\mathbf{x} \cong \mathbf{N}_I^p(\hat{\mathbf{x}}_L^C) \quad (3.62)$$

which shows that shape functions evaluated at stabilization points can be used for both the fluid pressure projection and the stabilized nodal integration, saving computational cost. Since the evaluation of the pressure projection terms in equations (3.61) and (3.62) already provides most of the matrices required for the evaluation of direct shape function derivatives, the smoothed gradients at the stabilization points in equations (3.56) and (3.59) can be replaced with the direct gradients to reduce the number of gradient smoothing points. Consider that if a rectangular nodal integration domain is used for 2D problems, with SCNI the shape functions need to be evaluated at only 9 points, including the node itself, 4 stabilization points, and 4 gradient smoothing evaluation points. On the other hand, in order to achieve comparable accuracy with Gauss quadrature, both shape functions and their direct derivatives are required to be evaluated at 25 integration points at least [Chen, Hillman, Rüter (2013)]. The advantage of SCNI is more obvious in 3D applications, where 125 evaluation points are needed for Gauss quadrature using the commonly adopted hexahedron zones, while in the proposed nodal integration scheme the shape function evaluation is required at only 13 points, including the node itself, 6 stabilization

points, and 6 gradient smoothing evaluation points. Clearly, the stabilized nodally integrated meshfree method is quite attractive for solving large-scale, coupled problems because of its high efficiency and accuracy.

3.4 Numerical Examples

To verify the proposed formulation, several hydro-mechanical coupled problems are analyzed. For simplicity, the effect of gravity force is neglected, and as commonly adopted in soil mechanics the bulk modulus of the porous matrix is assumed to be much smaller than the bulk modulus of the grains, which is not a restriction of the present formulation. Linear basis is used for both the solid displacement and the fluid pressure fields, and the support size of the meshfree shape function is set to be 1.5 times the average nodal distance. Although meshfree shape functions do not have the Kronecker delta property, efficient treatments are available for the imposition of essential boundary conditions, such as Nistche's method, Lagrange multipliers, penalty method, the singular kernel method and transformation method, etc [Chen and Wang (2000); Fernández-Méndez and Huerta (2004)]. In solving the following problems, both the penalty method and the transformation method have been tested and no noticeable difference in their results was found.

In the following, the fluid pressure projection approach is denoted as FPP, and NI refers to the direct nodal integration method, whereas SCNI denotes the stabilized conforming nodal integration method.

3.4.1 Terzaghi's problem

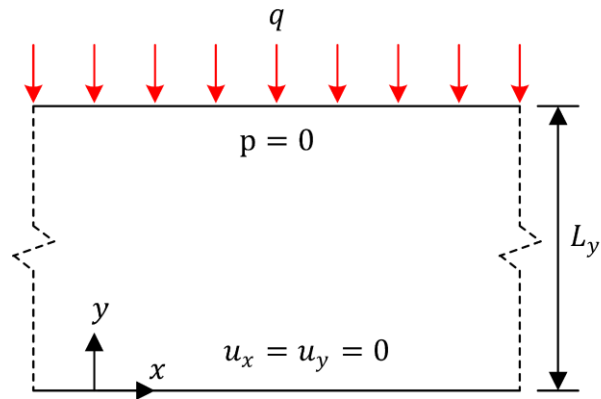


Figure 3.4 Description of Terzaghi's problem

In the first numerical test, the classical Terzaghi's consolidation problem [Verruijt, van Baars (2007)] is analyzed. As shown in Figure 3.4, a soil layer of thickness $L_y = 10.0$ m is considered to be infinitely long in the horizontal direction. At initial time, a distributed load of constant intensity q is suddenly applied which expels the pore water from the top surface. A two dimensional numerical model for the domain size 3.0×10.0 m² is used, where the horizontal displacement at the boundary is fixed. The adopted time step is $\Delta t = 1.0$ s and the material parameters are chosen as follows: Young's modulus $E = 1.0$ kPa, Poisson's ratio $\nu = 0.0$, hydraulic conductivity $k_h = 1.0 \times 10^{-5}$ m/s, specific weight of fluid $\gamma_f = 10.0$ kN/m³, and fluid bulk modulus $K_f = 2.2$ GPa.

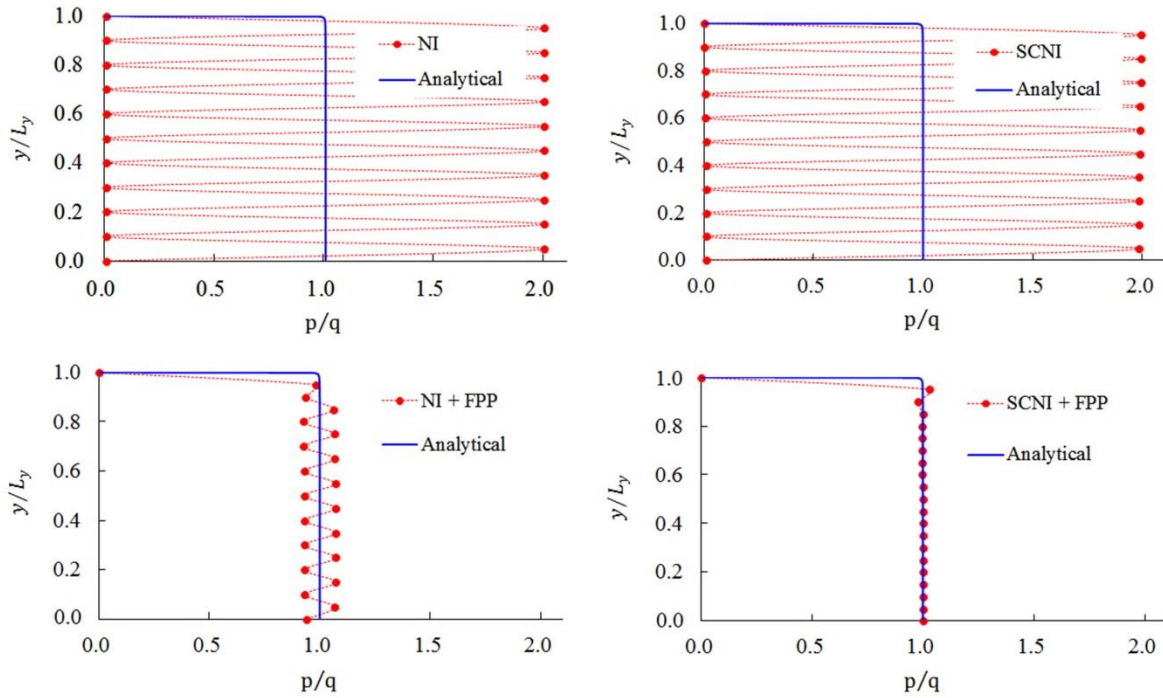


Figure 3.5 Normalized fluid pressure profile for Terzaghi's problem

The fluid pressure profile after the initial time step is shown in Figure 3.5, where 7×21 nodes are used for the different numerical formulations. It can be seen that formulations using only SCNI or NI yield severe oscillations in fluid pressure field since the requirement of inf-sup condition is not satisfied. Although this spurious oscillation can be partially alleviated by adding FPP to the NI formulation, unphysical pressure modes are still observable due to the instability caused by the direct nodal integration method. On the other hand, a stable and accurate solution is obtained by employing FPP in conjunction with SCNI, achieving a good agreement with the analytical solution. Minor overshoot using the SCNI + FPP formulation appears near the drainage boundary, which is caused by the extremely sharp pressure gradient. This phenomenon is also observed in stable finite elements and would not affect the solution in the rest of the domain as discussed in [Haga, Osnes, Langtangen (2012); White and Borja (2008)]. Numerical

results using 21, 41, and 81 nodes along the vertical direction are plotted in Figure 3.6, showing that convergence can be achieved when the spatial discretization is refined.

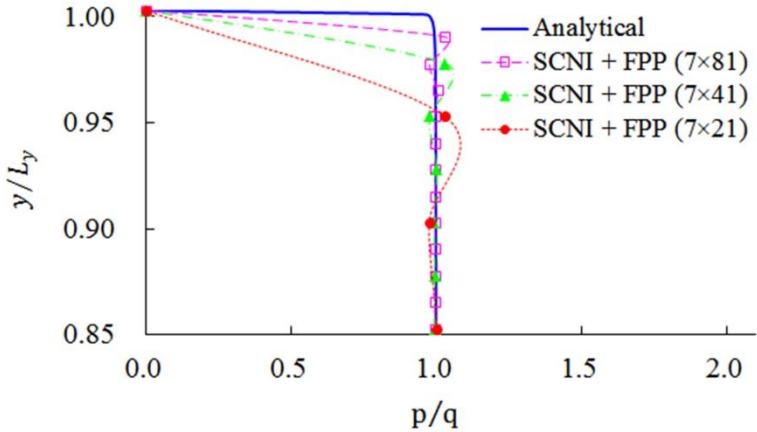


Figure 3.6 Normalized fluid pressure profile near the drainage boundary

3.4.2 Mandel’s problem

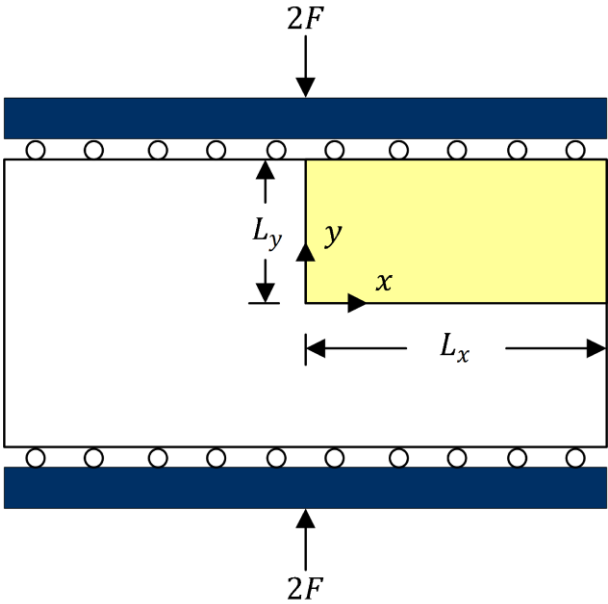


Figure 3.7 Description of Mandel’s problem

As shown in Figure 3.7, a pair of vertical loads of constant magnitude $2F$ is applied to a poroelastic soil sample through rigid and frictionless plates. The length and height of the rectangular soil sample are $2L_x$ and $2L_y$, respectively. While the two sides in lateral direction are fully drained, other boundaries are impermeable. Analytical expressions for the pressure and the vertical displacement fields are respectively derived in [Mandel (1953)] and [Abousleiman, Cheng, Cui, Detournay, Roegiers (1996)] as follows:

$$p = 2p_{0^+} \sum_{n=1}^{\infty} \frac{\sin \alpha_n}{\alpha_n - \sin \alpha_n \cos \alpha_n} \left(\cos \frac{\alpha_n x}{L_x} - \cos \alpha_n \right) \exp(-\alpha_n^2 T_D)$$

$$u_y = \left[-\frac{(1-\nu)F}{2GL_x} + \frac{(1-\nu_u)F}{GL_x} \sum_{n=1}^{\infty} \frac{\sin \alpha_n \cos \alpha_n}{\alpha_n - \sin \alpha_n \cos \alpha_n} \exp(-\alpha_n^2 T_D) \right] y$$

where $T_D = c_f t / L_x^2$ is the dimensionless time, c_f is the fluid diffusivity coefficient, G is the shear modulus, α_n are the positive solutions to the nonlinear equation $(\tan \alpha_n) / \alpha_n = (1-\nu) / (\nu_u - \nu)$, in which $\nu_u = 0.5$ for incompressible fluid, and the fluid pressure distribution at the instant of loading $p_{0^+} \equiv \lim_{t \rightarrow 0} p$ depends on both the average force density F/L_x and material parameters, for which an analytical expression can be found in [Abousleiman, Cheng, Cui, Detournay, Roegiers (1996); Phillips and Wheeler (2007)].

Considering the symmetries, only one quarter of the slab (i.e. the colored part in Figure 3.7) is modeled with $L_x = 20.0$ and $L_y = 2.0$. Symmetric conditions are enforced on the left and the bottom boundaries, whereas vertical displacement on the top is controlled by applying the analytical solution using $F = 2L_x$. Initial conditions are set as zero for both displacement

and fluid pressure fields. Incompressible fluid is assumed and material parameters are chosen from the reference [Preisig and Prevost (2011)] as $E = 1.0 \times 10^4$, $\nu = 0.0$, $\nu_u = 0.5$, $k_f = 1.0 \times 10^{-4}$, which results in $c_f = 1.0$ and $p_{0^+} = 1.0$.

The early time response of Mandel's problem has been analyzed in [Preisig and Prevost (2011)] using stabilized FE formulation, for which three different dimensionless time increments $\Delta t_D = c_f \Delta t / h^2$ of 0.01, 0.1 and 1.0 are adopted, respectively, and their study shows that the undrained behavior could lead to spurious pressure oscillations in the numerical solution when small time increment is used and thus stabilization procedure is required. To assess the performance of the present meshfree formulation, the same dimensionless time increments are also chosen here. The meshfree computation results of the normalized fluid pressure distribution along horizontal direction using 101×11 nodes are given in Figure 3.8 together with the analytical solutions and the stabilized finite element results from [Preisig and Prevost (2011)] denoted as FEM + FPL, where FPL denotes the fluid pressure Laplacian (FPL) stabilization method. It can be seen that oscillations appear for direct nodally integrated (NI) formulation even when FPP is applied, while the stable SCNI + FPP formulation can offer much satisfactory results compared with the reference solutions.

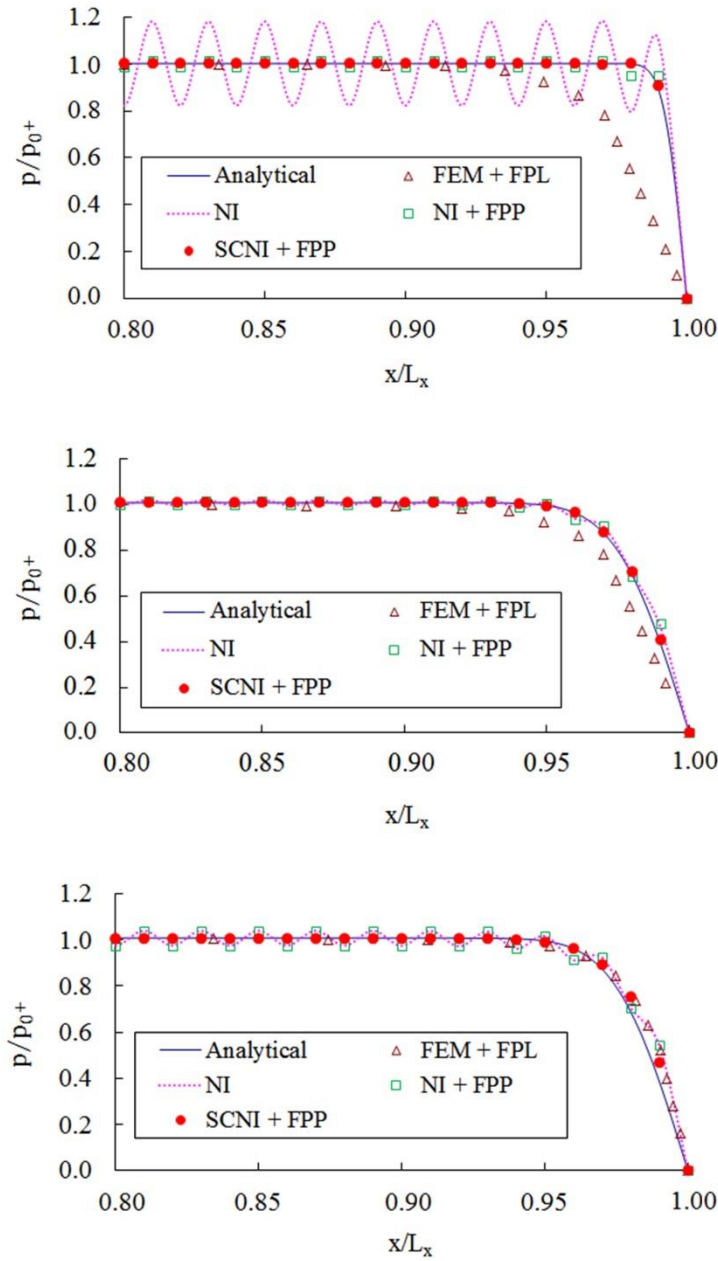


Figure 3.8 Normalized fluid pressure distribution at time $T_D = 2.0 \times 10^{-5}$ using $\Delta t_D = 0.01$ with 20 time steps (top); at $T_D = 2.0 \times 10^{-4}$ using $\Delta t_D = 0.1$ with 20 time steps (middle) and using $\Delta t_D = 1.0$ with 2 time steps (bottom)

Next, the distribution of the fluid pressure for various time instants is plotted in Figure 3.9. Again, good agreement is achieved between the analytical solutions and the SCNI + FPP meshfree formulation. An important aspect of Mandel’s problem is that near the center of the

sample the pressure initially increases beyond the instantaneous response p_{0^+} at time of loading, and it dissipates later, which is known as the Mandel-Cryer effect [Mandel (1953) ; Cryer (1963)] due to the strong hydro-mechanical coupling and is confirmed by experiments [Gibson, Knight, Taylor (1963)]. As shown in Figure 3.9, this coupling effect is well captured by the proposed stabilized meshfree formulation.

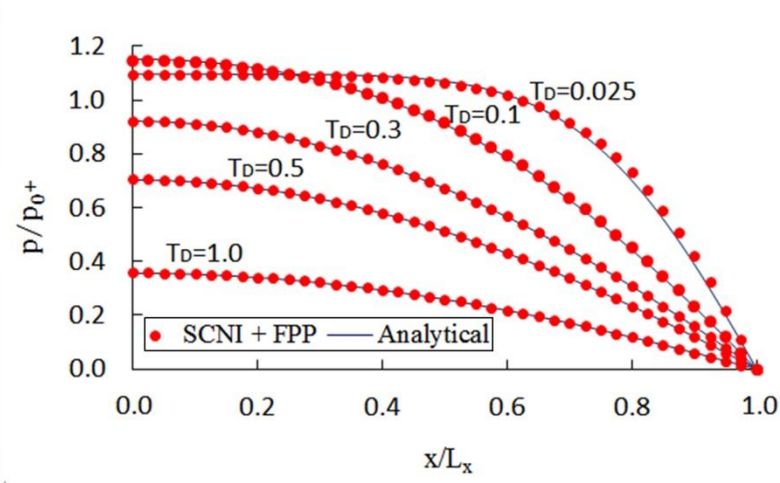


Figure 3.9 Normalized fluid pressure distribution for Mandel’s problem at various dimensionless time T_D

3.4.3 Strip load on elastic half space

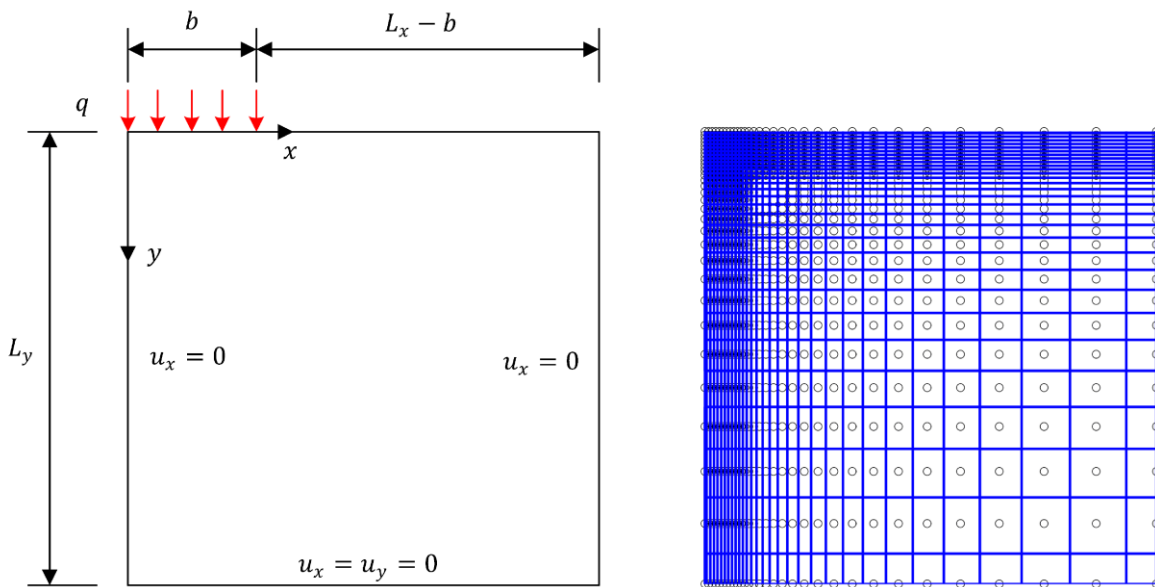


Figure 3.10 Description of the footing problem (left) and its meshfree numerical model with the Voronoi diagram (right)

A constant surface pressure of intensity $q = 10.0 \text{ kPa}$ is distributed over a width of $2b = 0.4 \text{ m}$ on the draining surface of the semi-infinite soil ground. The material parameters are as follows: Young's modulus $E = 1.0 \times 10^4 \text{ kPa}$, Poisson's ratio $\nu = 0.0$, hydraulic conductivity $k_h = 5.0 \times 10^{-8} \text{ m/s}$, specific weight of fluid $\gamma_f = 9.8 \text{ kN/m}^3$, and the pore fluid is assumed to be incompressible. Due to symmetry, only one half of the domain is modeled, as shown in Figure 3.10, where the height $L_x = 25b$ and width $L_y = 25b$ can be considered to be large enough to minimize the boundary effect in order to properly represent the infinite space.

This problem has been analyzed by [Xie and Wang (2014)] using standard RKPM via a staggered strategy for solving the system of coupled equations, while here the same coupled equations are solved in a monolithic manner by applying the proposed stabilized, nodally

integrated RKPM formulation. The same spatial discretization as that used in [Xie and Wang (2014)] is employed in this study, which consists of 31×31 non-uniformly distributed nodes. The adopted discretization is shown in Figure 3.10 along with the nodal representative integration zones. For convenience, the dimensionless time is defined as $T_D = Ek_h T / (1 + \nu) \gamma_f b^2$, and the time step size $\Delta t = 19.6$ s is chosen such that the dimensionless time increment $\Delta t_D = Ek_h \Delta t / (1 + \nu) \gamma_f b^2$ is equal to 0.025.

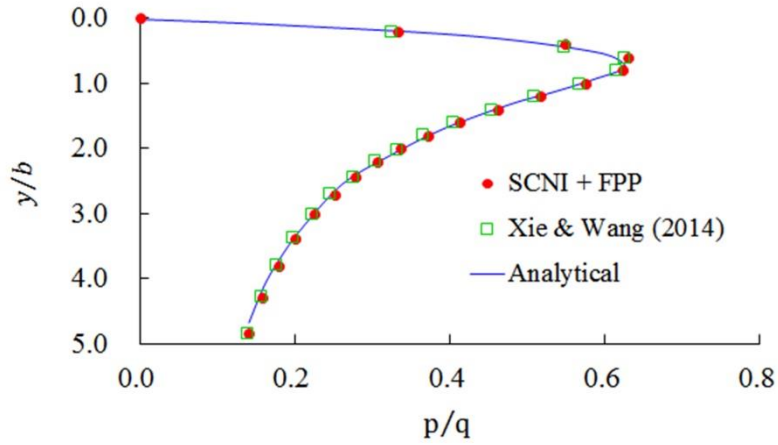


Figure 3.11 Normalized fluid pressure distribution along the central vertical line at time $T_D = 0.1$

The numerical results of pore fluid pressure at $x = 0.0$ m along the height at $T_D = 0.1$ are plotted in Figure 3.11, along with the analytical solution from [Chen (1966); Schiffman, Chen, Jordan (1969)]. As can be seen, good agreement between all the three results are obtained, which verifies the accuracy of the present approach. It should be noted that for the considered case no spurious pressure oscillations would appear even without FPP stabilization. The time history of the fluid pressure at location $x = 0.0$ m, $y = 0.2$ m is also plotted in Figure 3.12 and again the proposed meshfree formulation gives satisfactory result.

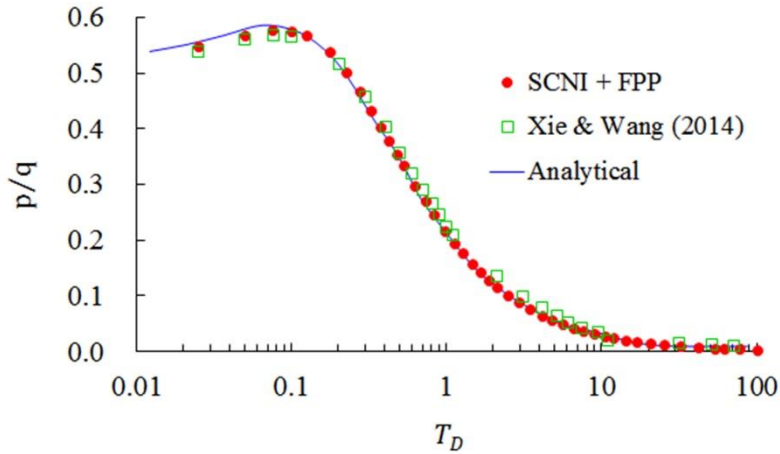


Figure 3.12 Time history of fluid pressure at location $x = 0.0$ m, $y = 0.2$ m

To further demonstrate the robustness of the stabilized meshfree formulation, we analyze a low permeable case for which $k_h = 5.0 \times 10^{-13}$ m/s is chosen and the surface boundary is treated as undrained. The spatial and temporal discretization is kept the same as before, and the numerical results using different formulations for the contours of fluid pressure and displacement fields are shown in Figure 3.13. Clearly, severe oscillations appear in the fluid pressure field without using SCNI or FPP, which would also affect the horizontal displacement field although the vertical displacement field seems not to be influenced much. On the other hand, the proposed formulation (SCNI + FPP) gives a stable solution as expected.

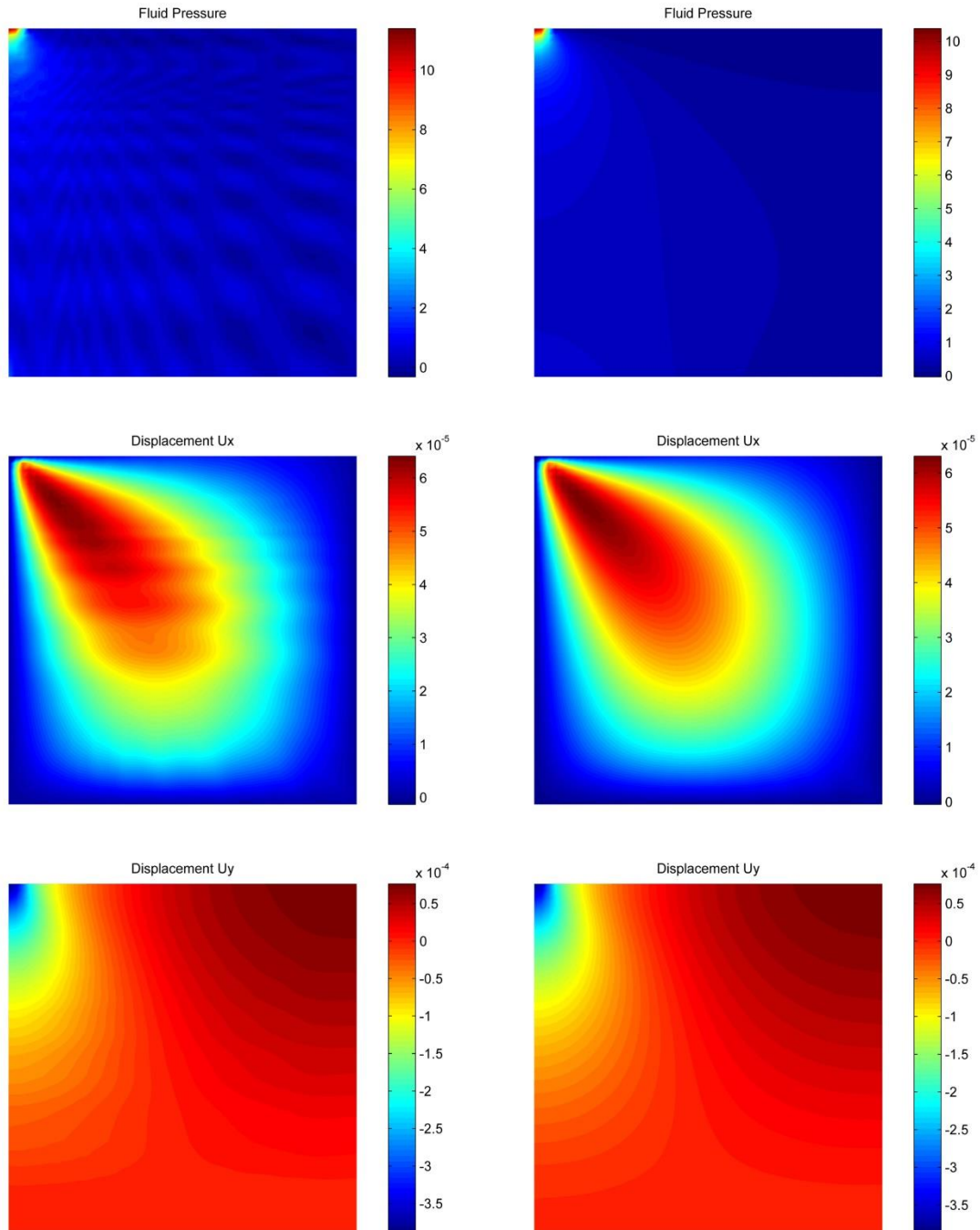


Figure 3.13 Numerical results of the fluid pressure, horizontal displacement, and vertical displacement distribution (from top to bottom) for the low permeable case, using the NI formulation (left) and the SCNI+FPF formulation (right)

Acknowledgements

Chapter 3, in part, is a reprint of the material as it appears in “Wei, Haoyan, Chen, Jiun-Shyan, & Hillman, Michael. A Stabilized Nodally Integrated Meshfree Formulation for Fully Coupled Hydro-Mechanical Analysis of Fluid-Saturated Porous Media. *Computers & Fluids*, 141, 105-115, 2016”. The dissertation author was the primary investigator and author of this paper.

Chapter 4

A Damage Particle Method for Smeared Modeling of Brittle Fracture

This chapter is organized as follows. In Section 4.1, the continuum damage model and its relation to the cohesive crack model is reviewed and used as the basis for the smeared modeling of brittle fracture. In Section 4.2, the damage particle method is introduced under a nodally integrated meshfree computational framework, where the smeared strain is defined as the boundary integral of the reproducing kernel approximated displacement field. Furthermore, the scaling of damage laws based on equivalent damage energy and fracture energy dissipations is presented. Numerical examples of benchmark problems are given in Section 4.3 to examine the effectiveness of this approach.

4.1 Continuum Damage Model

In quasi-brittle materials, the growth and coalescence of a large number of cracks are difficult to capture by the discrete crack models. Alternatively, the cracked solids can be approximated as damaged continua based on the Continuum Damage Model (CDM) that assumes the following form of the stress-strain relationship:

$$\boldsymbol{\sigma} = (\mathbb{I} - \mathbf{D}) : \bar{\boldsymbol{\sigma}} \quad (4.1)$$

where \mathbf{D} is the damage tensor, \mathbb{I} is the fourth rank identity tensor, and $\bar{\boldsymbol{\sigma}}$ is the undamaged effective stress tensor. In the present smeared crack approach, the undamaged effective stress is defined as $\bar{\boldsymbol{\sigma}}(\tilde{\boldsymbol{\varepsilon}}) = \mathbf{C}^e : \tilde{\boldsymbol{\varepsilon}}$, where \mathbf{C}^e is the elastic material moduli, and $\tilde{\boldsymbol{\varepsilon}}$ is the smeared strain to be discussed in Section 4.2. For illustration purpose, an isotropic damage model with $\mathbf{D} = D(\kappa)\mathbb{I}$ is considered, where the scalar damage variable D is defined as

$$D(\kappa) = \begin{cases} 0 & \text{for } \kappa < \kappa_o \\ 1 - \frac{\kappa_o}{\kappa} \frac{\kappa_c - \kappa}{\kappa_c - \kappa_o} & \text{for } \kappa_o \leq \kappa \leq \kappa_c \\ 1 & \text{for } \kappa_c < \kappa \end{cases} \quad (4.2)$$

where κ_o is the limit elastic strain under uniaxial tension, and κ_c is the critical equivalent strain that controls the slope of the stress-strain softening response, κ is an irreversible internal state variable which satisfies the following Kuhn-Tucker conditions:

$$\dot{\kappa} \geq 0 \quad (4.3)$$

$$\varepsilon_{eq} - \kappa \leq 0 \quad (4.4)$$

$$\dot{\kappa}(\varepsilon_{eq} - \kappa) = 0 \quad (4.5)$$

Here ε_{eq} is the equivalent strain [Mazars (1986)]

$$\varepsilon_{eq} = \sqrt{\sum_{I=1}^3 \langle \varepsilon_I^P \rangle^2} \quad (4.6)$$

where $\langle \dots \rangle$ denotes the Macaulay bracket and ε_I^P is the I^{th} principal strain.

While the present work focuses on the smeared fracture modeling, a comparison between the continuum damage and the discrete crack models is essential [Jirásek (2011); Xu and Waas (2016)]. For demonstration purposes, let us consider a model problem that involves the fracturing process of a bar with Young's modulus E , length L and cross-section area A stretched under a displacement control as shown in Figure 4.1. The body force and the Poisson effects are neglected, and the failure process is triggered by a line of weakened material in the middle of the bar.

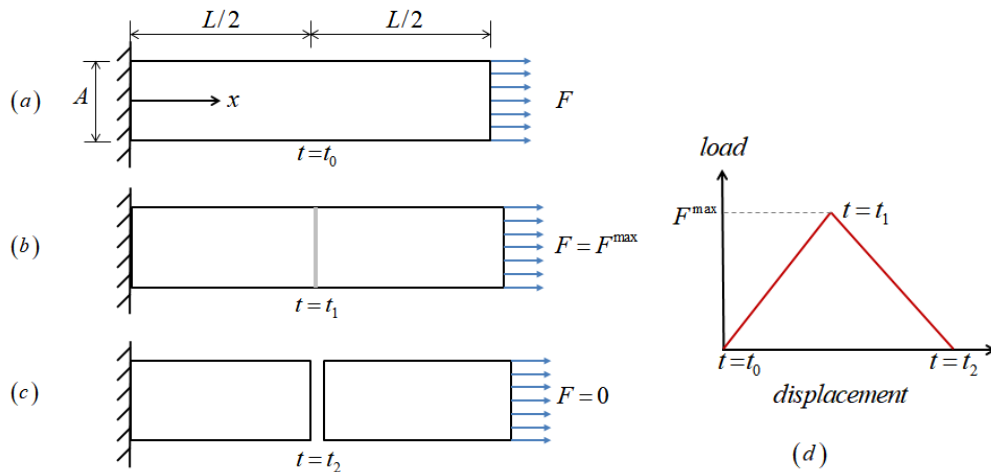


Figure 4.1 (a-c) Illustration of the failure process of a bar with weakened material at the middle cross-section and (d) the expected load-displacement response

Consider a cohesive zone model to describe the failure process corresponding to the post-peak stage of the load-displacement response ($t \geq t_1$ in Figure 4.1 (d)), the following linear cohesive traction-separation law is introduced on the cohesive crack surface:

$$\sigma = \left(1 - \frac{w}{w_c}\right) f_t \quad (4.7)$$

where $\sigma = F/A$ is the uniaxial stress, $w = u|_{x=(L/2)^+} - u|_{x=(L/2)^-}$ is the crack opening displacement at $x = L/2$, $w_c = (2G_F)/f_t$ is the critical crack opening displacement, G_F is the fracture energy and f_t is the tensile strength.

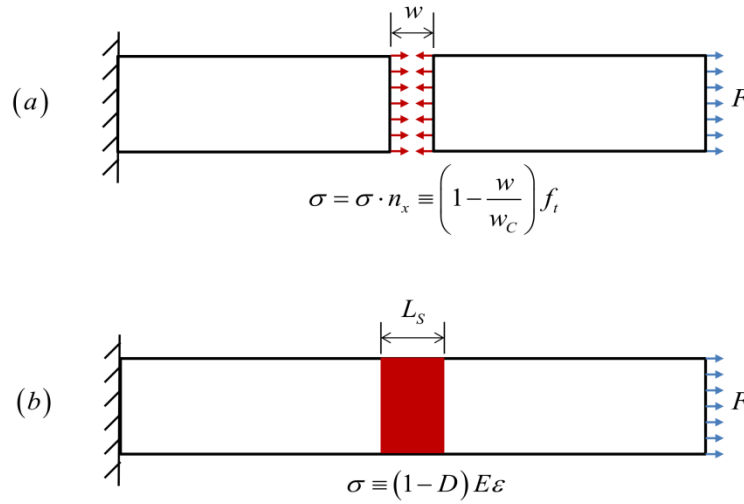


Figure 4.2 Illustration of adopting (a) the discrete cohesive zone model (CZM) and (b) the continuum damage model (CDM) for the cracked bar problem

The relation between the cohesive zone model and the continuum damage model is discussed below, which follows the analogy given in [Jir ásek (2011)]. With the cohesive law in (4.7), the total displacement u_T at the loading end of the softening bar is expressed as

$$u_T = u_E + w \quad (4.8)$$

where $u_E = \varepsilon_E L = (\sigma/E)L$ denotes the total elastic deformation of the bar, in which ε_E denotes the elastic strain. The above two equations yield the following relationship between the

total displacement u_T and the load F during the failure process

$$u_T = \frac{FL}{EA} + \frac{2G_F}{f_t} \left(1 - \frac{F}{f_t A} \right) \quad (4.9)$$

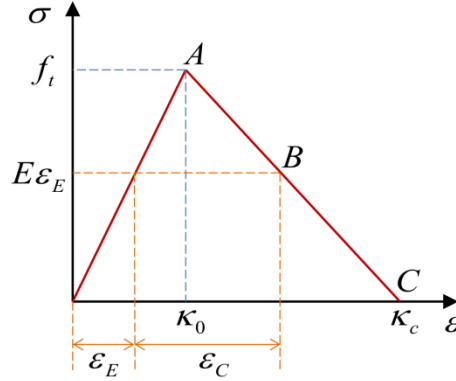


Figure 4.3 Illustration of the 1-D stress-strain relationship based on the continuum damage model, where the tensile strength is reached at point A, the complete failure occurs at point C, and point B refers to an arbitrary state at the softening stage.

Next, consider the continuum damage model described in (4.1), which can be written in the following 1-D form

$$\sigma = (1 - D)E\varepsilon = E(\varepsilon - D\varepsilon) = E\varepsilon_E \quad (4.10)$$

From the continuum damage model representation given above, an inelastic strain ε_C can be defined based on an additive decomposition of the total strain ε (see the illustration in Figure 4.3):

$$\varepsilon = \varepsilon_E + \varepsilon_C \quad (4.11)$$

where $\varepsilon_C = D\varepsilon$. Let the damage zone size be L_S as shown in Figure 4.2 (b). The total

displacement u_T of the bar with length L can be expressed as

$$u_T = \varepsilon_E (L - L_S) + (\varepsilon_E + \varepsilon_C) L_S = \varepsilon_E L + D \varepsilon L_S \quad (4.12)$$

Comparing equations (4.8) and (4.12), it is seen that the damage model can yield the same load-displacement response as that of the cohesive zone model if the following relationship holds:

$$w = D \varepsilon L_S \quad (4.13)$$

In this connection, the displacement jump w in the discrete cohesive fracture model has been “smeared” over the zone with width L_S in the damage model.

Furthermore, by equalizing the stress generated by the cohesive traction-separation law in (4.7) and the damage constitutive law in (4.10), and considering equation (4.13), the following expression for the damage evolution can be obtained.

$$D = \frac{1 - \frac{\kappa_0}{\varepsilon}}{1 - \frac{\kappa_0 L_S}{w_C}} \quad (4.14)$$

where $\kappa_0 = f_t/E$ as defined in (4.2). The above equation exactly recovers the damage law defined previously in (4.2), if the following condition is satisfied:

$$\kappa_c = w_C / L_S \quad (4.15)$$

where κ_c is the critical threshold strain. Since $w_c = (2G_F)/f_t$ represents the critical crack opening, the above equation implies that κ_c is indeed a model parameter dependent on the smeared zone size L_s . Clearly, treating κ_c as a constant parameter independent on the smeared zone size L_s will lead to unphysical prediction for this model problem. Computationally, the smeared zone size L_s is related to the adopted discretization grid size, thus a conventional numerical implementation of continuum damage models results in discretization size dependent, non-convergent solutions. Another computational issue with continuum damage models for fracture modeling is the spurious prediction of fracture patterns, which tends to appear when the crack propagation path is not aligned with the distribution of the discretization grid. To address the above issues, a damage particle method is proposed in the next section, where a dissipation energy scaling method is employed in conjunction with the smeared strain formulated under the stabilized conforming nodal integration framework to achieve a regularized smeared description of fractures.

4.2 The Damage Particle Method

4.2.1 Variational equation

Let us consider a body initially occupying the domain Ω_0 with the boundary Γ_0 , and for a material point $\mathbf{X} \in \Omega_0$, $\mathbf{x} = \mathbf{x}(\mathbf{X}, t)$ is the position of \mathbf{X} in the deformed body Ω with the boundary Γ at time t . The variational equation of linear momentum conservation with reference to the current configuration is

$$\int_{\Omega} \rho \delta \mathbf{u} \cdot \ddot{\mathbf{u}} d\Omega + \int_{\Omega} \delta \boldsymbol{\varepsilon} : \boldsymbol{\sigma} d\Omega = \int_{\Omega} \delta \mathbf{u} \cdot \mathbf{b} d\Omega + \int_{\Gamma^h} \delta \mathbf{u} \cdot \mathbf{t} d\Gamma \quad (4.16)$$

where \mathbf{u} is the displacement vector, $\boldsymbol{\varepsilon}$ is the strain tensor, $\ddot{\mathbf{u}}$ is the acceleration vector, ρ is the mass density, $\boldsymbol{\sigma}$ is the Cauchy stress tensor, \mathbf{b} is the body force vector, \mathbf{t} is the prescribed traction on the natural boundary Γ^h , and δ denotes the variation. The spatial discretization of equation (4.16) is carried out by the reproducing kernel approximation [Liu et al. (1995); Chen et al. (1996)] which is constructed based on a set of NP points $\{\mathbf{x}_I \mid \mathbf{x}_I \in \Omega\}_{I=1}^{NP}$.

The reproducing kernel approximation of the displacement field is

$$\mathbf{u}^h(\mathbf{x}, t) = \sum_{I=1}^{NP} N_I(\mathbf{x}) \mathbf{d}_I(t) \quad (4.17)$$

where $\mathbf{d}_I(t)$ is the nodal coefficient vector, and $N_I(\mathbf{x})$ is the reproducing kernel shape function introduced in the previous chapter. In the following, the effects of cracking will be treated with the continuum damage model introduced in Section 4.1, in conjunction with a regularization scheme to be described in subsequent sections.

4.2.2 Approximation of fracture surfaces by damaged particles

In the present study, the fracture is approximated by a set of discrete crack segments as shown in Figure 4.4 so as to circumvent the burden associated with modeling complex crack patterns such as crack branching and coalescence [Remmers et al. (2003); de Borst et al. (2004); de Borst et al. (2006); Song and Belytschko (2009); Rabczuk and Belytschko (2004); Rabczuk and Belytschko (2007); Rabczuk et al. (2010); Rabczuk (2013)]. In contrast to the above mentioned studies, we do not model the crack segments with discrete crack models which

require explicit treatment of discontinuities and singularities. Instead, an attempt is made here to introduce a regularized smeared crack model based on a node-based discretization, where the associated nodal representative domains can be generated by the Voronoi diagram as shown in Figure 4.4.

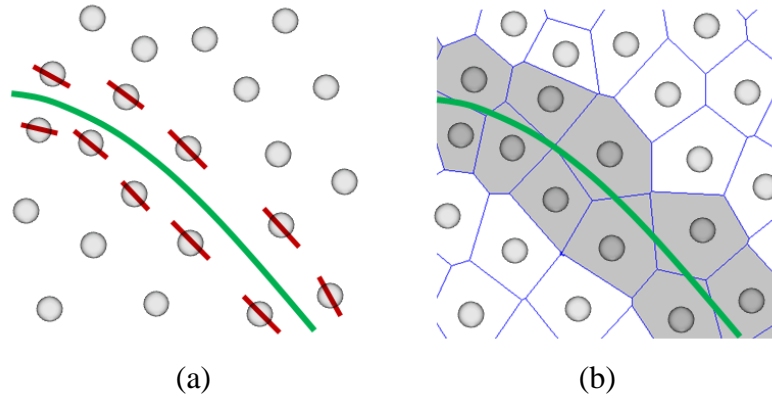


Figure 4.4 Illustration of the fracture path (green line) and its approximation based on a set of crack segments passing the nodal points of the meshfree model, where red lines in (a) represent the discrete crack segments and are modeled in a smeared manner over the representative domains in grey color associated with damaged particles in (b).

In each nodal representative domain Ω_L associated with \mathbf{x}_L (Figure 4.5), a smeared strain $\tilde{\boldsymbol{\varepsilon}}(\mathbf{x}_L)$ at \mathbf{x}_L is defined as

$$\tilde{\boldsymbol{\varepsilon}}(\mathbf{x}_L) = \frac{1}{V_L} \int_{\Omega_L} \boldsymbol{\varepsilon}(\mathbf{x}) d\Omega \quad (4.18)$$

where $V_L = \int_{\Omega_L} d\Omega$ is the volume of the nodal representative domain (or area of the nodal representative domain in two dimensions).

Further taking divergence operation of the smeared strain, we have

$$\tilde{\varepsilon}_{ij}(\mathbf{x}_L) = \frac{1}{V_L} \int_{\Omega_L} \varepsilon_{ij} d\Omega = \frac{1}{2V_L} \int_{\Omega_L} (u_{i,j} + u_{j,i}) d\Omega = \frac{1}{2V_L} \int_{\Gamma_L} (u_i n_j + u_j n_i) d\Gamma \quad (4.19)$$

where Γ_L is the boundary of the nodal representative domain Ω_L , and n_i is the i^{th} component of the outward unit normal to Γ_L as shown in Figure 4.5.

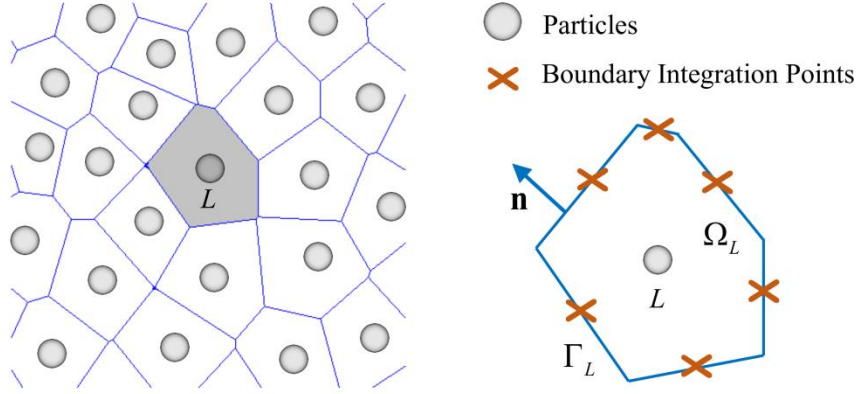


Figure 4.5 Illustration of the nodal representative domain and boundary integral for smeared strain computation

In the present approach, the smeared strain computed at each nodal representative domain is employed to determine the damage and stress states. For instance, if the continuum damage model in (1) is considered, the Cauchy stress $\boldsymbol{\sigma}(\mathbf{x}_L)$ at node \mathbf{x}_L is computed as

$$\tilde{\boldsymbol{\sigma}}(\mathbf{x}_L) = (\mathbb{I} - \mathbf{D}(\tilde{\boldsymbol{\varepsilon}}(\mathbf{x}_L))) : \bar{\boldsymbol{\sigma}}(\tilde{\boldsymbol{\varepsilon}}(\mathbf{x}_L)) \quad (4.20)$$

where $\mathbf{D}(\tilde{\boldsymbol{\varepsilon}}(\mathbf{x}_L))$ is the damage tensor and $\bar{\boldsymbol{\sigma}}(\tilde{\boldsymbol{\varepsilon}}(\mathbf{x}_L))$ is the undamaged effective stress tensor computed based on the smeared strain.

Introducing the reproducing kernel approximation of displacements defined in (4.17) into (4.19), the following approximated smeared strain $\tilde{\varepsilon}_{ij}^h(\mathbf{x}_L)$ is obtained:

$$\begin{aligned}
\tilde{\varepsilon}_{ij}^h(\mathbf{x}_L) &= \frac{1}{2V_L} \int_{\Gamma_L} (u_i^h n_j + u_j^h n_i) d\Gamma \\
&= \frac{1}{2V_L} \sum_{I \in G_L} \int_{\Gamma_L} (N_I n_j d_{iI} + N_I n_i d_{jI}) d\Gamma
\end{aligned} \tag{4.21}$$

where $G_L = \{I \mid N_I(\mathbf{x}_L) \neq 0\}$ is the set of particles whose associated reproducing kernel shape functions cover particle \mathbf{x}_L . The resulting form of the smeared strain naturally avoids taking direct derivatives of the displacement field, which is not well-defined near the boundary of the smeared cracking zone. In this work, the boundary integral in (4.21) is carried out by one-point integration over the Voronoi cell boundary as shown in Figure 4.5, but higher order quadrature can be employed if better accuracy is desired.

To capture fracture propagation, we follow the Rankin criterion which postulates the crack growth direction to be perpendicular to the maximum principal stress direction. To this end, the following criterion [Rabczuk and Belytschko (2004); Song and Belytschko (2009)] is adopted to identify the candidate damage particles near the predicted crack growth path:

$$\left| \mathbf{n}_L^D \cdot \frac{\mathbf{x}_I - \mathbf{x}_L}{\|\mathbf{x}_I - \mathbf{x}_L\|} \right| = \cos\left(\frac{\pi}{2} - \alpha_{iL}^D\right) < tol \quad \text{for } \mathbf{x}_I \in \mathbb{N}_L \tag{4.22}$$

where \mathbf{x}_L is the position vector of damaged particle L , \mathbb{N}_L is the set containing the neighboring particles of \mathbf{x}_L , which can be determined by the Voronoi cells, and \mathbf{n}_L^D is the unit normal vector of the crack segment associated with the damaged particle L , which is defined along the maximum principal stress direction at \mathbf{x}_L , α_{iL}^D is the relative angle between the position vector $\mathbf{x}_I - \mathbf{x}_L$ and the crack segment at the damaged particle L , and tol denotes a

small tolerance. The criterion (4.22) is checked at the end of every time step. For example, in the neighbor list of the damaged particle L shown in Figure 4.6, only particle P satisfies this criterion and will be considered as the candidate damage particle for the next time step.

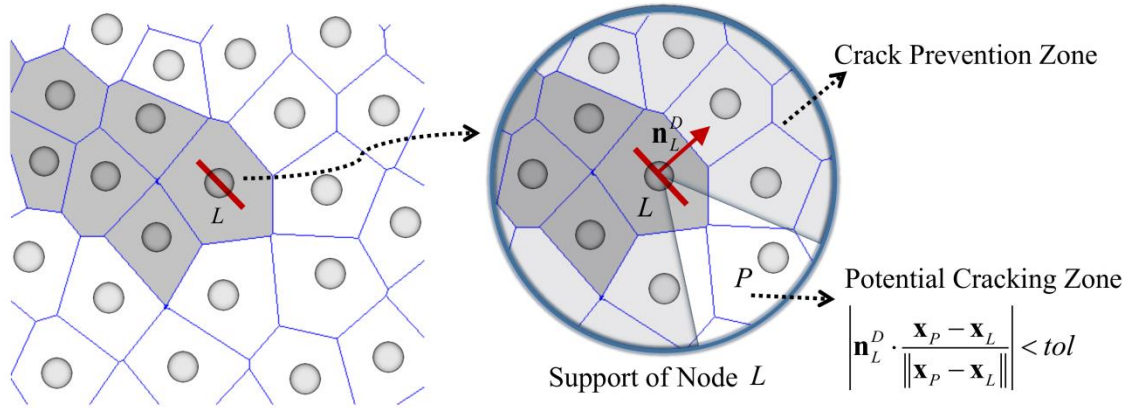


Figure 4.6 Illustration of the potential cracking zone and the crack prevention zone associated with the damaged particle L , where the red line represents the discrete crack segment located at the damaged particle L , and the representative domains associated with damaged particles are shown in dark grey color.

For each candidate damage particle, damage initiation occurs when certain measure of the smeared strain in their nodal representative domain Ω_L exceeds a threshold. For example, $\varepsilon_{eq}(\tilde{\mathbf{e}}^h) \geq \kappa_0$ for the damage law given in (4.2)-(4.6) corresponds to the formation of a crack segment. At the damage initiation, the unit normal vector \mathbf{n}_L^D corresponding to the crack segment surface is calculated based on the maximum principal stress direction at particle L as illustrated in Figure 4.6, and is fixed in the subsequent loading process.

4.2.3 Dissipation energy-based regularization

Since a set of crack segments is employed to approximate the fracture, the total energy dissipation due to all crack segments is required to satisfy the following condition

$$\sum_{L \in S_D} (G_F A_L^{eff}) = G_F A_F \quad (4.23)$$

where G_F is the fracture energy dissipated per surface area, A_F is the fracture surface area (the total length of the green line in Figure 4.4), A_L^{eff} is the “effective” surface area of the crack segment associated with the damaged particle L , and S_D is the node set that contains all the damaged particles. As the fracture processes are induced due to the deformation of materials on both sides of the fracture surface as shown in Figure 4.4, the geometric relation gives $\sum_{L \in S^D} A_L \cong 2A_F$, where A_L is the area of the intersection plane between the Voronoi cell and the surface perpendicular to the crack normal \mathbf{n}_L^D at particle L , as shown in Figure 4.7. As such, the effective surface area of the crack segment takes the following relation

$$A_L^{eff} = A_L/2 \quad (4.24)$$

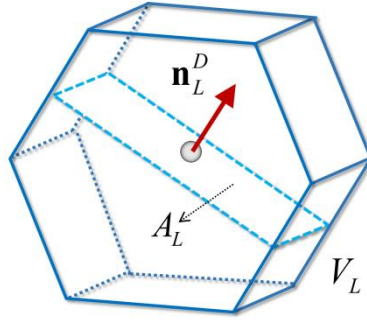


Figure 4.7 Illustration of the Voronoi cell associated with the damaged particle L , where V_L is the volume of the nodal representative domain, \mathbf{n}_L^D is the unit normal vector of the crack segment, and A_L is the area of the intersection plane between the Voronoi cell and the surface perpendicular to the vector \mathbf{n}_L^D at particle L

Hence, given the geometry of the Voronoi cell and the orientation of the crack segment,

the effective surface area A_L^{eff} can be calculated and adopted as a geometric approximation to the fracture surface.

To ensure objective energy dissipation in smeared crack modeling, a regularization approach based on the crack band theory [Bažant and Oh (1983); Cervera and Chiumenti (2006a); Cervera and Chiumenti (2006b); Jirásek and Bauer (2012)] is introduced herein. With the continuum damage model, the bulk damage energy dissipation associated with all damaged particles is related to the total surface fracture energy by the following global energy equivalence:

$$\sum_{L \in S_D} g_L V_L = G_F A_F \quad (4.25)$$

where g_L is the specific bulk energy dissipation associated with the damaged particle L . To meet the above requirement, the bulk energy dissipation associated with each damaged particle is made equal to the surface energy required to form a discrete crack segment within the nodal representative domain, that is

$$g_L V_L = G_F A_L^{eff} \quad (4.26)$$

With the damage model described in Figure 4.3 in Section 4.1, the specific bulk energy dissipation is expressed as

$$g_L = \frac{1}{2} f_t \kappa_c \quad (4.27)$$

where $f_t = E\kappa_o$ is the tensile strength. Substituting equation (4.27) into equation (4.26), the following expression for κ_c is obtained

$$\kappa_c = \frac{2G_F}{f_t} \left(\frac{A_L^{eff}}{V_L} \right) = \frac{G_F}{f_t} \left(\frac{A_L}{V_L} \right) \quad (4.28)$$

When equation (4.28) is adopted to scale the parameter κ_c , the corresponding stress-strain softening curve in Figure 4.3 is adjusted to ensure energy dissipation equivalence between each damaged particle and the associated crack segment in (4.26).

4.2.4 Meshfree discrete equations

In the present smeared modeling approach, the domain integration of the variational equation (16) is performed by the Stabilized Conforming Nodal Integration (SCNI) [Chen et al. (2001); Chen et al. (2002)] for the following reasons. As has been studied earlier, SCNI meets the integration constraints [Chen et al. (2001); Chen et al. (2013)] in the Galerkin meshfree approximation of second order partial differential equations with linear consistency. Moreover, under the SCNI framework, the domain is partitioned into conforming nodal representative volumes (e.g., Voronoi cells), which provides a node-based domain partitioning for 1) computation of the smeared strain in (4.21) without taking direct derivatives of the displacement field which are not well-defined in the smeared cracking region; 2) obtaining the effective crack surface area in the smeared crack model to transform the fracture energy into the damage energy with the aforementioned energy scaling law; and 3) allowing the displacement and damage variables to be computed at the same nodal points without the need to interpolate between variables computed at Gauss points and nodal points in the conventional finite element

approaches.

Since the internal energy $\int_{\Omega} \delta \boldsymbol{\varepsilon} : \boldsymbol{\sigma} d\Omega$ in the variational equation (6.16) is related to the fracture process of the materials, the nodally integrated discrete form of this internal energy term by the reproducing kernel approximation is discussed in the following. By introducing a nodal integration, the internal energy $\int_{\Omega} \delta \boldsymbol{\varepsilon} : \boldsymbol{\sigma} d\Omega$ is approximated as follows:

$$\int_{\Omega} \delta \boldsymbol{\varepsilon} : \boldsymbol{\sigma} d\Omega \approx \sum_{L=1}^{NP} \delta \tilde{\boldsymbol{\varepsilon}}(\mathbf{x}_L) : \boldsymbol{\sigma}(\tilde{\boldsymbol{\varepsilon}}(\mathbf{x}_L)) V_L \quad (4.29)$$

Here, $\tilde{\boldsymbol{\varepsilon}}(\mathbf{x}_L)$ is the smeared strain defined in (4.19), and V_L is the volume (or area in two dimensions) of Ω_L . Taking into account the reproducing kernel approximation of the smeared strain in (4.21), we have the following approximated smeared stress at \mathbf{x}_L for the nodal representative domain Ω_L :

$$\tilde{\boldsymbol{\sigma}}^h(\mathbf{x}_L) = \boldsymbol{\sigma}(\tilde{\boldsymbol{\varepsilon}}^h(\mathbf{x}_L)) = (\mathbb{I} - \mathbf{D}(\tilde{\boldsymbol{\varepsilon}}^h(\mathbf{x}_L))) : \mathbf{C}^e : \tilde{\boldsymbol{\varepsilon}}^h(\mathbf{x}_L) \quad (4.30)$$

where the damage state \mathbf{D} within Ω_L is determined by the smeared strain $\tilde{\boldsymbol{\varepsilon}}^h(\mathbf{x}_L)$ along with the scaled parameter κ_c based on (4.28), which ensures the energy equivalence imposed by (4.26) within a nodal representative domain. Note that the nodal volume V_L and the surface area A_L used in the dissipation energy-based scaling procedure are associated with the same Voronoi cell used for the smeared strain calculation. For convenience, the smeared stress tensor $\tilde{\boldsymbol{\sigma}}^h(\mathbf{x}_L)$ can be represented in Voigt notation as a vector

$\tilde{\boldsymbol{\Sigma}}(\mathbf{x}_L) = [\tilde{\sigma}_{11}^h(\mathbf{x}_L) \quad \tilde{\sigma}_{22}^h(\mathbf{x}_L) \quad \tilde{\sigma}_{12}^h(\mathbf{x}_L)]^T$ for two dimensional problems. Similarly, the vector form of the approximated smeared strain in (4.21) can be expressed as follows

$$[\tilde{\varepsilon}_{11}^h(\mathbf{x}_L) \quad \tilde{\varepsilon}_{22}^h(\mathbf{x}_L) \quad 2\tilde{\varepsilon}_{12}^h(\mathbf{x}_L)]^T = \sum_{I \in G_L} \tilde{\mathbf{B}}_I(\mathbf{x}_L) \mathbf{d}_I \quad (4.31)$$

where $\mathbf{d}_I = [d_{1I} \quad d_{2I}]$, and $\tilde{\mathbf{B}}_I(\mathbf{x}_L)$ is the associated smeared gradient matrix:

$$\tilde{\mathbf{B}}_I(\mathbf{x}_L) = \begin{bmatrix} \tilde{b}_{1I}(\mathbf{x}_L) & 0 \\ 0 & \tilde{b}_{2I}(\mathbf{x}_L) \\ \tilde{b}_{2I}(\mathbf{x}_L) & \tilde{b}_{1I}(\mathbf{x}_L) \end{bmatrix} \quad (4.32)$$

$$\tilde{b}_{iI}(\mathbf{x}_L) = \frac{1}{V_L} \int_{\Omega_L} N_{I,i} \, d\Omega = \frac{1}{V_L} \int_{\Gamma_L} N_I n_i \, d\Gamma \quad (4.33)$$

By introducing the reproducing kernel approximation of the smeared strain and the smeared stress, the internal force vector $\mathbf{f}_I^{\text{int}}$ for node I is computed as follows:

$$\mathbf{f}_I^{\text{int}} \approx \sum_{L=1}^{NP} \tilde{\mathbf{B}}_I^T(\mathbf{x}_L) \tilde{\boldsymbol{\Sigma}}(\mathbf{x}_L) V_L \quad (4.34)$$

Consequently, the final matrix equations are obtained as:

$$\mathbf{M}\ddot{\mathbf{d}} = \mathbf{f}^{\text{ext}} - \mathbf{f}^{\text{int}} \quad (4.35)$$

where \mathbf{M} and \mathbf{f}^{ext} are the mass matrix and the external force vector, respectively, obtained from the variational equation (4.16) by standard procedures [Chen et al. (1996)].

Remark 4.2.1 In the proposed method, the computation of displacement, strain, stress, and damage variables along with the regularization procedure in (4.26)-(4.28) are performed at the nodal points. Therefore, this approach avoids the interpolation of state and field variables between Gauss points and nodal points commonly needed in the conventional finite elements, for which the smeared cracking zone size can be affected by the number of Gauss integration points within each element domain and requires additional treatments [Jir ásek and Bauer (2012)].

Remark 4.2.2 The proposed smeared fracture modeling approach naturally fits into the SCNI framework, as the proposed smeared strain and the associated nodal integration of internal energy turn out to be equivalent to the SCNI for Galerkin meshfree methods. As a result, the strain, stress, and variational equation in the undamaged and damaged zones are computed with a unified formulation, where the SCNI strain smoothing ensures the accuracy and convergence of meshfree solutions as analyzed in [Chen et al. (2001); Chen et al. (2013)].

4.3 Numerical Examples

To validate the effectiveness of the proposed formulation, several benchmark fracture problems are analyzed. Linear basis and cubic B-spline kernel with circular nodal support size of 1.5 times the average nodal distance are adopted for constructing the reproducing kernel shape functions. The singular kernel method is used for the imposition of essential boundary conditions [Chen and Wang (2000)]. The diffraction method [Organ et al. (1996)] is employed for modeling pre-existing cracks in example problems 4.2 and 4.3 by modifying the support domain of the nodes which cover the initial cracks. An implicit incremental-iterative procedure is used for the

quasi-static problem in Example 4.1, and the explicit central difference method is adopted for time integration in the other example problems.

4.3.1 A cracked bar under tension

Smearred crack approaches provide convenience for fracture modeling as they avoid the complexities associated with explicit modeling of moving strong discontinuities. However, such methods can be ill-posed and lead to discretization sensitive numerical results, unless effective regularization techniques are employed. To examine the regularization performance of the proposed smeared fracture modeling approach, a fundamental localization test of a bar under uniaxial tension [Jirásek and Bauer (2012); Xu and Waas (2016)] is analyzed. The damage particle method is employed and the results are compared to that of the cohesive zone model as well as the unregularized particle-based damage formulation. Here, the unregularized particle-based damage formulation refers to the damage analysis based on nodally integrated reproducing kernel discretization but without adopting the regularization procedures given in (4.26)-(4.28), that is, the parameter κ_c is kept constant throughout the damage process.

A description of this model problem has been given in Section 4.1 (see Figure 4.1). In the following, the length of the bar is taken as $L=1.0\times 10^2$ with the cross-section area $A=10.0$ (dimensionless unit is used). In addition, the bar is considered to be homogeneous with Young's modulus $E=2.0\times 10^6$, fracture energy $G_F=1.885$, and tensile strength $f_t=2.0\times 10^2$ (i.e., the limit elastic strain of the damage model $\kappa_0=f_t/E=1.0\times 10^{-4}$), except for the weakened material plane at the middle cross-section where tensile fracture occurs. To achieve a smeared modeling of the fracture process, a slightly lower limit elastic strain of 99.9% κ_0 is used for

particles whose nodal representative domains intersect with the pre-defined weak plane, so that these particles are damaged once this reduced damage threshold is met. To investigate the solution sensitivity with respect to the discretization size, we adopt four models consisting of 16, 32, 64 and 128 nodes along the rod axis. Accordingly, the fracture at the middle cross-section will be captured via damage localization over the nodal representative domains containing the weak plane.

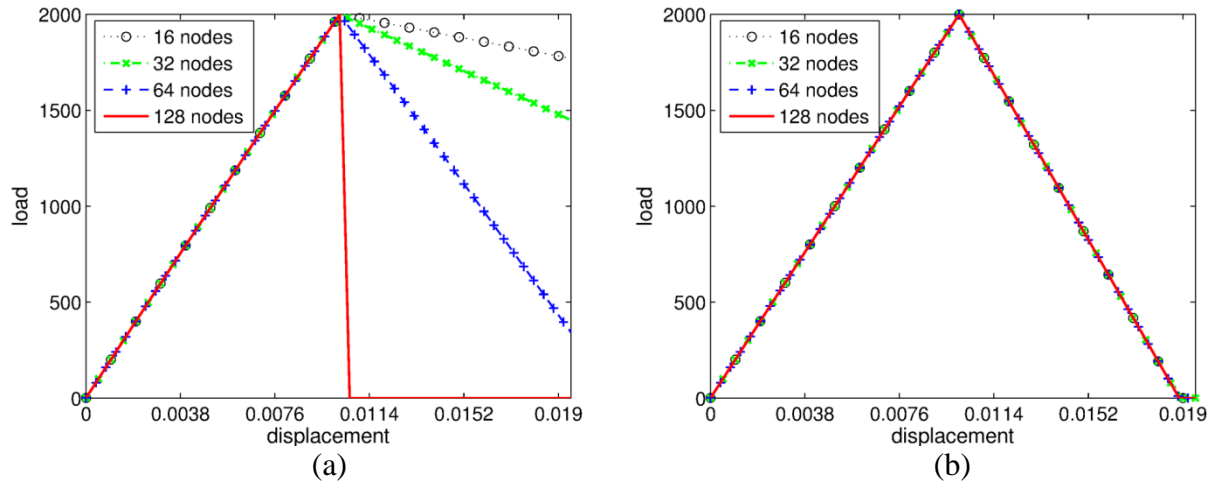


Figure 4.8 Load-displacement curve obtained from (a) unregularized particle-based damage formulation, (b) the proposed damage particle method

In Figure 4.8, the curves of the axial force versus the displacement at the loading end are plotted. It can be seen from Figure 4.8 (a) that the unregularized particle-based damage formulation suffers from discretization size dependency, i.e., the global energy dissipation (the area under the load-displacement curve) decreases spuriously as the numerical model is refined. This is expected since the specific bulk energy dissipation g_l is assigned a constant value (i.e., κ_c is treated as a constant parameter) in the un-regularized model, while the volume of the smeared cracking zone (the total nodal representative volume associated with the two damaged

particles in this model problem) shrinks as the discretization is refined. The spurious and non-convergent energy dissipation behavior of the unregularized particle-based damage formulation is effectively corrected in the damage particle method [Figure 4.8 (b)], which ensures that the global energy dissipation is always equivalent to the total fracture energy $G_F A$ dissipated during the fracturing process through appropriate scaling of the damage law. According to the cohesive zone model in equation (4.7), when the load F reduces to zero, the total displacement achieves its maximum magnitude $u_T^{\max} = 2(G_F A)/F^{\max}$ according to (4.9), where $F^{\max} = f_t A$ is the maximum magnitude of the total force (at the peak of the load-displacement curve). For the adopted parameters, $u_T^{\max} = 1.8850 \times 10^{-2}$ is the expected value, which agrees well with the numerical prediction of $u_T^{\max} = 1.8858 \times 10^{-2}$ by the damage particle method shown in Figure 4.8 (b).

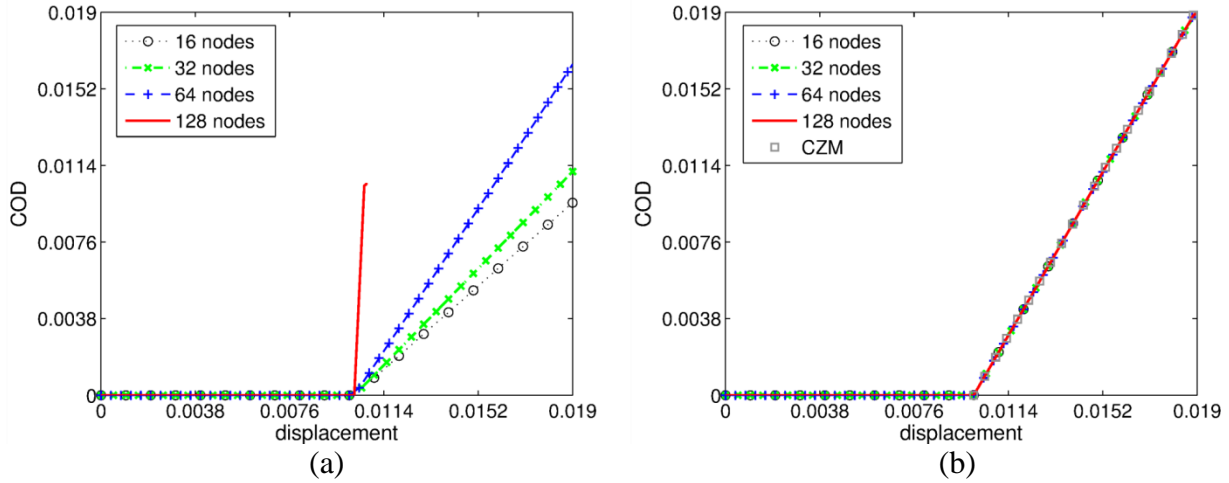


Figure 4.9 Evolution of crack opening displacement (COD) versus the displacement at the loading end of the bar, obtained from (a) unregularized particle-based damage formulation, (b) the proposed damage particle method, and CZM refers to the reference solution based on the cohesive zone model.

Furthermore, the crack opening $w = \int_{(L-L_s)/2}^{(L+L_s)/2} D \varepsilon dx$ [(4.13)] computed from the meshfree simulation is compared to the evolution of the displacement jump w from the cohesive zone model-based analysis in Figure 4.9. As expected, the prediction of the damage particle method is consistent with the discrete surface-based cohesive model, while the unregularized formulation suffers from discretization size sensitivity.

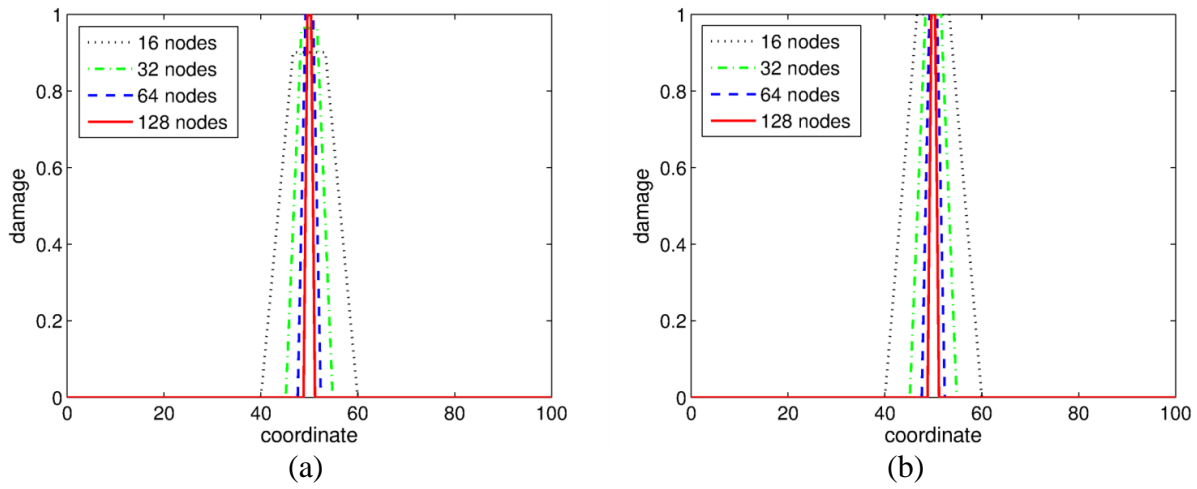


Figure 4.10 The smeared cracking zone (in terms of non-zero damage distribution along the bar) at tip displacement of u_T^{\max} , obtained from (a) unregularized particle-based damage formulation, (b) proposed damage particle method

At the end of the loading process (i.e., when the displacement at the loading end equals to u_T^{\max}), the predicted maximum magnitude of the damage variable changes as the discretization is refined in the unregularized particle-based damage formulation, as can be seen from Figure 4.10 (a). For the proposed approach, the damage variable always reaches the maximum value of one as shown in Figure 4.10 (b), which indicates the full opening of the cohesive fracture for all discretizations. Note that the width L_s of the smeared cracking zone (region with non-zero damage distribution), defined as the ratio of the nodal representative volume associated with

damaged particles to the effective surface area A_L^{eff} of the crack segment, decreases with discretization refinement since $A_L^{eff} = A/2$ is constant in this model problem. Similar behavior is observed in the crack band finite element method when the element size is reduced. However, as discussed in [Jirásek and Bauer (2012)], the smeared cracking zone width of the crack band finite element method can be affected not only by the element size and shape, but also by the integration scheme. This is because softening can localize into only some of the quadrature points within an element, which makes it cumbersome to obtain a reliable estimate of the smeared cracking zone size, especially for multi-dimensional problems. In contrast, since the damage particle method is formulated under the SCNI framework, the smeared zone size can be estimated within each nodal representative domain in a straightforward manner, allowing an effective energy scaling procedure as described in Section 4.2.

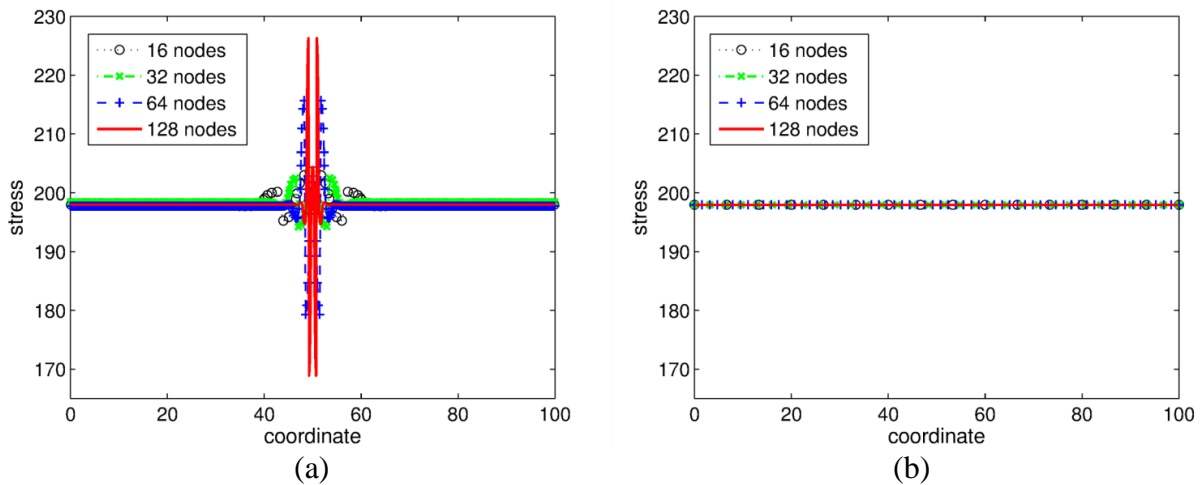


Figure 4.11 Distribution of axial stress along the bar, predicted by adopting (a) 8-Point Gauss quadrature using the direct gradient of the displacement field for strain calculation, and (b) SCNI scheme using the smeared strain

Next, the advantage of employing the smeared strain defined in (4.21) in conjunction with SCNI as the domain integration scheme is examined herein. At a time step after damage

initiation, the stress distributions obtained from 8-point Gauss quadrature and SCNI are plotted in Figure 4.11 (a) and Figure 4.11 (b), respectively. As shown in Figure 4.11 (a), when the Gauss quadrature scheme is used, severe stress oscillations appear and they cannot be eliminated with discretization refinement. This stress prediction could yield spurious damage growth in the subsequent loading steps and cause divergence in the algorithm. Similar stress oscillations have also been observed in [Jir ásek (1998b)] when the Element-Free Galerkin method is adopted for solving a similar strain localization problem. The proposed damage particle method, on the other hand, not only enhances the computational efficiency due to the nodal quadrature nature, but also reproduces the constant stress distribution in Figure 4.11 (b) as expected, and thus it is well-suited for solving smeared crack problems where localized strain exists. The effectiveness of the proposed damage particle method is attributed to the employment of the smeared strain formulated under the SCNI framework for predicting the stress and damage states, whereas the stress state yielded by the Gauss quadrature scheme is instead based on the direct derivatives of the non-smooth displacement field which is not well-defined near the smeared cracking region and thus results in spurious oscillations.

4.3.2 Kalthoff's impact problem

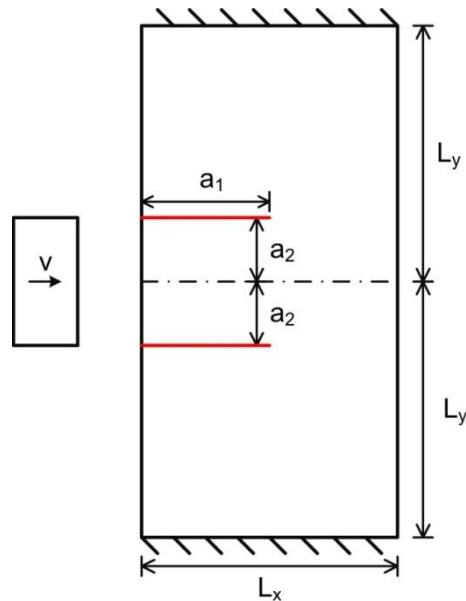


Figure 4.12 Illustration of Kalthoff's impact problem (the red lines represent initial cracks)

In this example, the fracture behavior of an edge-cracked plate under impulse loading is modeled. At a relatively low impact velocity, brittle failure with a crack propagation angle of about 70° was observed in the experiment as reported in [Kalthoff and Winkler (1987)]. Due to symmetry, only the upper half of the plate shown in Figure 4.12 is considered with edge length $L_x = L_y = 0.1$ m, and the vertical displacement is restrained on the plane of symmetry. The initial crack length is $a_1 = 0.05$ m, and the distance from the initial crack to the symmetry plane is $a_2 = 0.025$ m. An initial velocity of 16.5 m/s in the horizontal direction is introduced on the plate surface where the projectile impacts. The material parameters are as follows: fracture energy $G_F = 2.0 \times 10^4$ N/m, tensile strength $f_t = 9.5 \times 10^8$ Pa, Young's modulus $E = 1.9 \times 10^{11}$ Pa, Poisson's ratio $\nu = 0.3$, and mass density $\rho = 8.0 \times 10^3$ kN/m³.

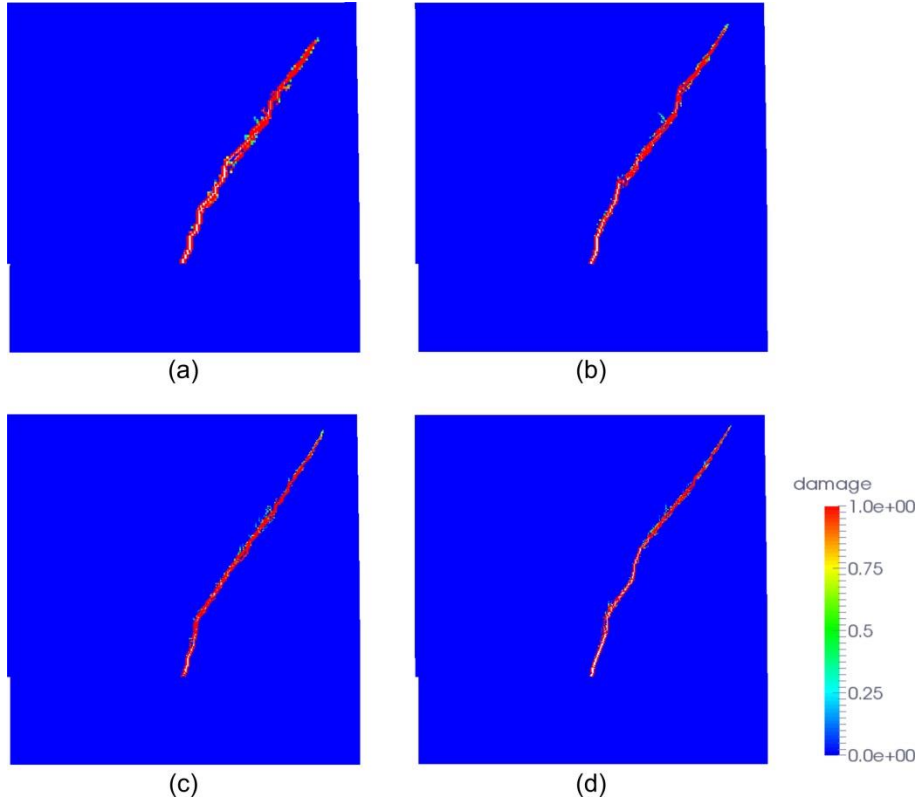


Figure 4.13 Distribution of the damage state, obtained from the damage particle method using (a) 22500 nodes, (b) 62500 nodes, (c) 122500 nodes, and (d) 202500 nodes.

To study the influence of the numerical discretization on the simulation results, models with different levels of discretization refinement are employed. The tolerance in the particle tracking criterion (4.22) is set as $tol = 0.3$. This restricts the relative angle α_{IL}^D in (4.22) between the vector $\mathbf{x}_I - \mathbf{x}_L$ and the crack segment direction to be approximately less than 20° , where \mathbf{x}_L is position of the damaged particle and \mathbf{x}_I is the position of a candidate damage particle.

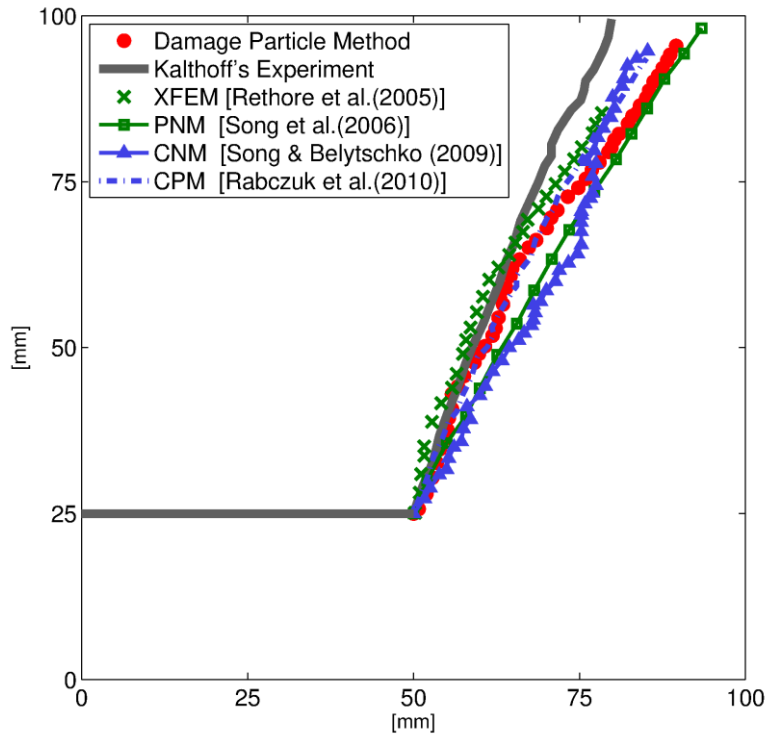


Figure 4.14 Comparison of the crack growth paths between the Kalthoff's experimental result and different numerical simulation, where XFEM, PNM, CNM and CPM denote the Extended Finite Element Method [Rethore et al. (2005)], Phantom Node Method [Song et al. (2006)], Cracking Node Method [Song and Belytschko (2009)] and Cracking Particle Method [Rabczuk et al. (2010)], respectively.

The results of predicted crack paths (shown as damage distribution) are plotted in Figure 4.13. It can be seen that consistent crack growth paths are obtained with different refinement levels of the models. Moreover, the predicted crack paths agree well with the reported results using XFEM [Rethore et al. (2005)], Phantom Node Method [Song et al. (2006)], Cracking Node Method [Song and Belytschko (2009)] and Cracking Particle Method [Rabczuk et al. (2010)], as shown in Figure 4.14.

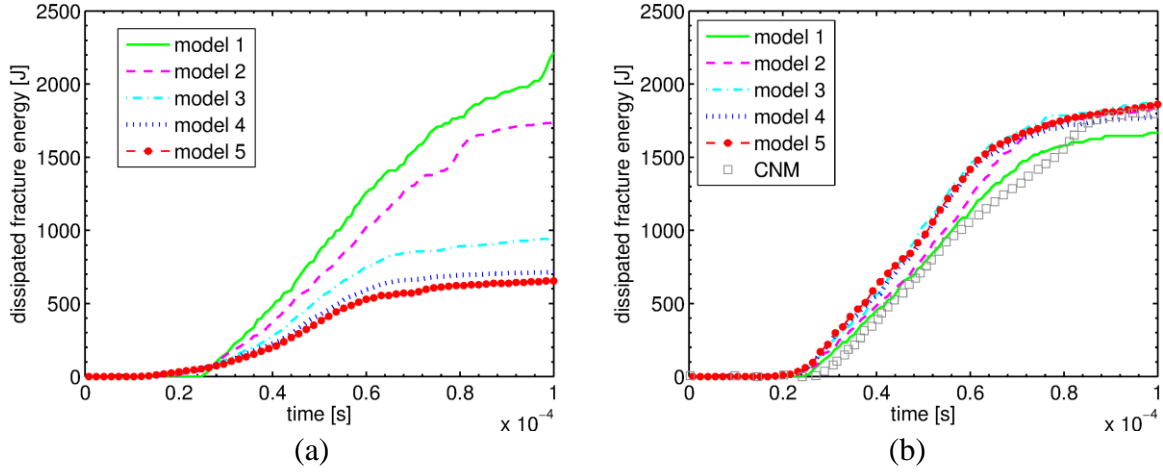


Figure 4.15 Evolution of global fracture energy dissipation, obtained from (a) unregularized particle-based damage formulation, (b) CNM (Cracking Node Method) from [Song and Belytschko (2009)] and the proposed damage particle method, where the models 1-5 consist of 10000, 22500, 62500, 122500 and 202500 nodes, respectively.

In addition to the predicted crack path, the discretization insensitive property of the proposed approach also manifests in the global energy dissipation during the crack growth process. In Figure 4.15, the time history of the global energy dissipation of the structure is plotted. Similar to the previous example analyzed in Section 4.3.1, if the damage evolution law is not scaled properly, the total energy dissipation during the structural failure process decreases as the numerical discretization is refined, as shown in Fig. 15 (a). On the other hand, objective energy dissipation is achieved by using the present damage particle method, as shown in Figure 4.15 (b). The energy dissipation predicted by the Cracking Node Method (CNM) in [Song and Belytschko (2009)] is also plotted in Figure 4.15 (b) as a reference. In the CNM, discrete crack segments are modeled with the cohesive zone model implemented with a partition of unity-based enrichment scheme. Although small discrepancies are observed in the energy dissipation time histories, the overall behaviors predicted by the proposed damage particle method and CNM agree well.

It is noted that the crack band type scaling procedure alone is insufficient to fully regularize the solution, as the crack path cannot always be predicted correctly without a proper physics-based control. If the particle tracking procedure introduced in Section 4.2.2 is not employed, the crack pattern in Figure 4.16 is obtained. Clearly, spurious damage initiation occurs at locations away from the physical fracture front, and the final crack path prediction is far from satisfactory. Therefore, both the energy scaling and the particle tracking procedures are important to achieve objective fracture modeling.

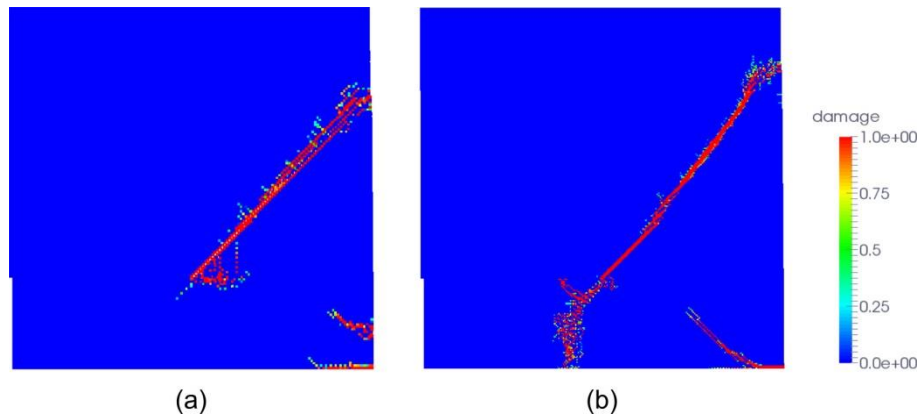


Figure 4.16 Distribution of the damage state, obtained when the damage particle tracking procedure is deactivated, using (a) 22500 nodes, (b) 62500 nodes.

4.3.3 Dynamic crack branching problem

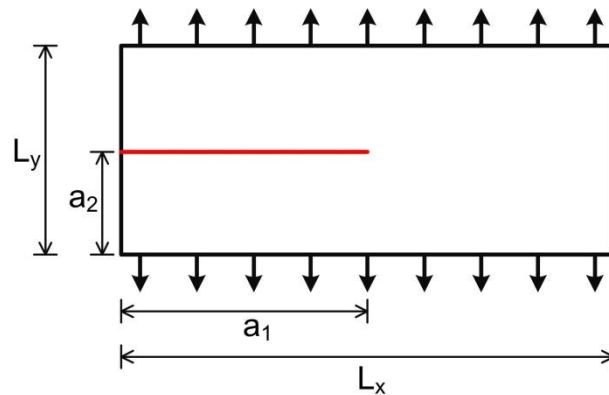


Figure 4.17 Illustration of the dynamic crack branching problem (the red line represents an initial crack)

A dynamic crack branching problem is analyzed herein, which remains challenging in finite element-based approaches [Song et al. (2008)]. As shown in Figure 4.17, a plate containing an initial edge crack is subjected to uniform tensile tractions of 1.0×10^6 Pa on its top and bottom surfaces. The length and width of the plate are $L_x = 0.1$ m and $L_y = 0.04$ m, respectively. The initial crack length is $a_1 = 0.05$ m, and the distance from the initial crack to the bottom edge of the plate is $a_2 = 0.02$ m. The material parameters are as follows: fracture energy $G_F = 3.0$ N/m, tensile strength $f_t = 2.72 \times 10^6$ Pa, Young's modulus $E = 3.2 \times 10^{10}$ Pa, Poisson's ratio $\nu = 0.2$, mass density $\rho = 2.45 \times 10^3$ kN/m³.

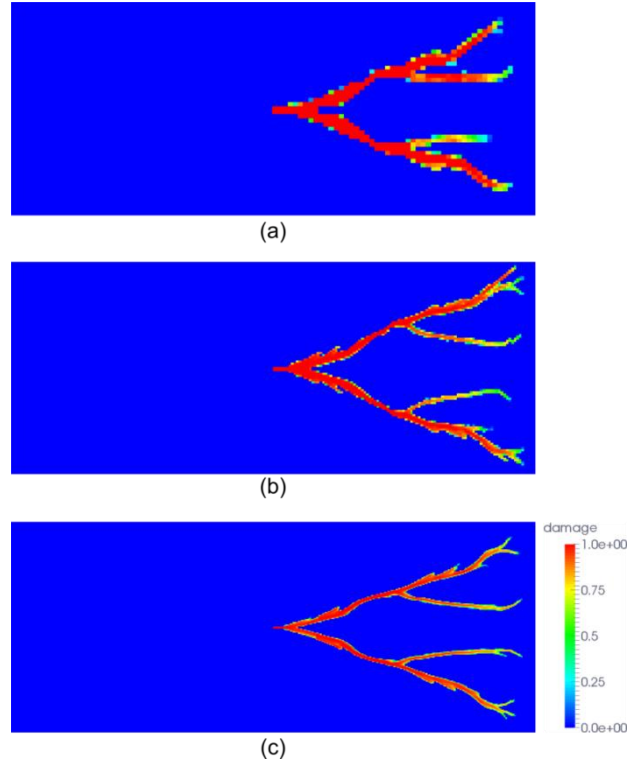


Figure 4.18 Distribution of the damage state, obtained from the damage particle method using different discretizations with the nodal distance (a) $h = 8 \times 10^{-4}$ m, (b) $h = 4 \times 10^{-4}$ m, and (c) $h = 2 \times 10^{-4}$ m, respectively.

To capture the crack branching phenomena, a relatively large tolerance $tol = 0.5$ is adopted for the search of potential damage particles, and thus a threshold of 30° for the relative angle α_{IL}^D in (4.22) is introduced. Three levels of refinement with nodal distance $h = 8 \times 10^{-4}$ m, 4×10^{-4} m, and 2×10^{-4} m are adopted in the reproducing kernel discretizations, and the predicted crack paths are shown in Figure 4.18. Due to dynamic instability, the crack branches into two major branches, and then a few minor branches also appear along the main branches. Similar crack branching patterns are obtained upon model refinement, and the simulation results agree well with the reported numerical results using the Cracking Particle Method [Rabczuk and Belytschko (2004); Rabczuk and Belytschko (2007)].

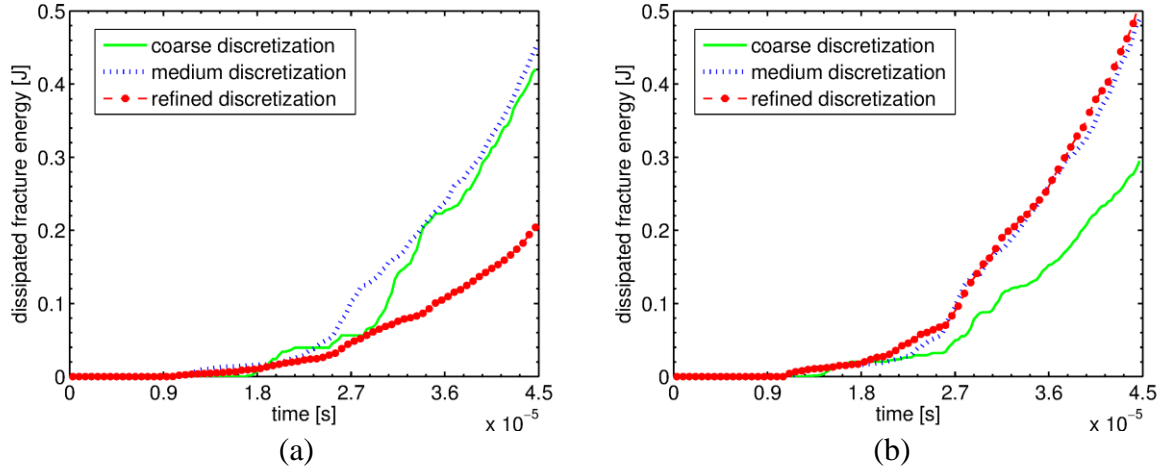


Figure 4.19 Evolution of global fracture energy dissipation, obtained from (a) unregularized particle-based damage formulation, (b) proposed damage particle method with different levels of discretization.

Time histories of the global dissipated energy are plotted in Figure 4.19. For the damage particle method, convergence in the total energy dissipation is observed when the model is refined as shown in Figure 4.19 (b), where lower energy dissipation with a relatively short crack path (see Figure 4.18 (a)) appears in the coarsest discretization. The total energy dissipation predicted by the unregularized particle-based damage formulation in Figure 4.19 (a), however, do not show a convergent behavior upon refinement of the numerical model.

Acknowledgements

Chapter 4, in part, has been submitted for publication of the material as it may appear in “Wei, Haoyan, Chen, Jiun-Shyan. A Damage Particle Method for Smeared Modeling of Brittle Fracture. International Journal for Multiscale Computational Engineering, 2018”. The dissertation author was the primary investigator and author of this paper.

Chapter 5

Application of the Damage Particle Method for Hydraulic Fracturing Simulation

This chapter is arranged as follows. Firstly, a smeared crack model that incorporates hydro-mechanical coupling effects is described in Section 5.1. Numerical implementation of the damage particle method under reproducing kernel mixed discretization is then presented in Section 5.2. In Section 5.3, several numerical problems are analyzed to demonstrate the effectiveness of the proposed method in hydraulic fracture modeling.

5.1 Smeared Crack Model for Fractured Saturated Porous Media

5.1.1 Balance equations

In this chapter, the damage particle method is introduced under the hydro-mechanically coupled modeling framework to simulate the hydraulic fracturing process. Based on the assumptions of isothermal single-phase flow and small deformation, the basic equations describing the mechanical behavior of saturated porous media consist of the momentum balance equation

$$\nabla \cdot \boldsymbol{\sigma} - \rho \ddot{\mathbf{u}} + \rho \mathbf{g} = \mathbf{0} \quad (5.1)$$

and the mass conservation equation

$$\alpha \nabla \cdot \dot{\mathbf{u}} + \nabla \cdot \mathbf{q}^w + (1/Q) \dot{p} = 0 \quad (5.2)$$

In the above equations, $\rho = n_f \rho_f + (1 - n_f) \rho_s$ is the averaged mass density, n_f is the porosity, and ρ_s and ρ_f are the mass densities of the solid and fluid phases, respectively, \mathbf{g} is the gravitational acceleration, \mathbf{q}^w is the fluid flux vector, α is the Biot coefficient, Q is the Biot compressibility modulus, \mathbf{u} is the displacement of solid, $\boldsymbol{\sigma}$ is the total Cauchy stress. On the outer surface Γ of the porous media, solid displacement $\mathbf{u} = \bar{\mathbf{u}}$ and fluid pressure $p^w = \bar{p}^w$ can be prescribed on the essential boundaries Γ_u and Γ_p , respectively, and traction $\mathbf{n}_\Gamma \cdot \boldsymbol{\sigma} = \bar{\mathbf{t}}$ and fluid outflow flux $\mathbf{n}_\Gamma \cdot \mathbf{q}^w = \mathbf{n}_\Gamma \cdot \bar{\mathbf{q}}_f$ can be imposed on the natural boundaries Γ_t and Γ_q , respectively, where \mathbf{n}_Γ is the outward unit normal vector to Γ , $\Gamma_u \cap \Gamma_t = \Gamma_p \cap \Gamma_q = \emptyset$ and $\Gamma_u \cup \Gamma_t = \Gamma_p \cup \Gamma_q = \Gamma$. At time $t=0$, initial conditions for the fluid pressure $p^w = p_0^w$ and stress $\boldsymbol{\sigma} = \boldsymbol{\sigma}_0$ are imposed, which satisfy the equilibrium condition in the reference state and reflect the loading and seepage history. In the present study, the fluid-filled cracks are represented in a smeared manner, and thus the effects of cracking on fluid flow and solid deformation are captured through the use of appropriate continuum constitutive models to be described in subsequent sections.

5.1.2 Continuum damage model for fluid-filled cracks

The constitutive law for the solid phase is introduced based upon the concept of total and effective stresses:

$$\boldsymbol{\sigma} = \boldsymbol{\sigma}'' - \alpha p \mathbf{I} \quad (5.3)$$

where $\boldsymbol{\sigma}$ is the total Cauchy stress, $\boldsymbol{\sigma}''$ is the effective stress, p is the fluid pressure, and \mathbb{I} is the 2nd order identity tensor. We have used the sign convention that tensile stress in solids and compressive pressure in fluids are positive. To capture the cracking effects on the mechanical behavior, the effective stress is expressed by a continuum damage model:

$$\boldsymbol{\sigma}'' = [\mathbb{I} - \mathbf{D}] : \bar{\boldsymbol{\sigma}}'' \quad (5.4)$$

where \mathbf{D} is the damage tensor, \mathbb{I} is the 4th rank identity tensor, $\bar{\boldsymbol{\sigma}}''$ is the undamaged effective stress governed by a linearly elastic constitutive law:

$$\bar{\boldsymbol{\sigma}}''(\tilde{\boldsymbol{\varepsilon}}) = \mathbf{C}^e : \tilde{\boldsymbol{\varepsilon}} \quad (5.5)$$

where $\tilde{\boldsymbol{\varepsilon}}$ is the smeared strain described in Chapter 4, and \mathbf{C}^e is the drained elasticity tensor. In the following, the isotropic damage model described in Chapter 4 is employed, i.e., $\mathbf{D} = D\mathbb{I}$. As the material stiffness of cracked region is reduced by the damage model, a modified Biot coefficient $\alpha = 1 - (1 - D)K/K_s$ is adopted in (5.2).

5.1.3 Cracking-enhanced permeability model

The distribution of fluid pressure p is governed by the mass conservation equation in (5.2), where the influence of cracking on fluid flow needs to be appropriately considered. Given the fluid pressure gradient ∇p , fluid flow in saturated porous media can be described by Darcy's law:

$$\mathbf{q}^w = -\mathbf{k}_f \cdot \nabla p \quad (5.6)$$

where \mathbf{k}_f is the permeability tensor, which can be written in the following form for intact and isotropic porous materials:

$$\mathbf{k}_f = k_{f0} \mathbf{I} \quad (5.7)$$

where $k_{f0} = k_h / \gamma_f$, k_h is the hydraulic conductivity and γ_f is the specific weight of the fluid.

In fractured porous media, however, an anisotropic permeability model is essential to account for the increase of fluid flow along the opened cracks under the smeared crack modeling framework [Pijaudier-Cabot et al. (2009); Miehe et al. (2015); Ma (2015)]. Along this line, the following permeability model is employed to describe the hydraulic behavior of the fractured porous media:

$$\mathbf{k}_f = (k_{fC} - k_{f0}) \mathbf{t}_C \otimes \mathbf{t}_C + k_{f0} \mathbf{I} \quad (5.8)$$

where k_{fC} represents the cracking-induced permeability along the crack path direction. In the present study, k_{fC} is derived based upon the equivalence between the fluid fluxes within the discrete fracture and over the smeared crack zone (illustrated in Figure 5.1), as described in the following.

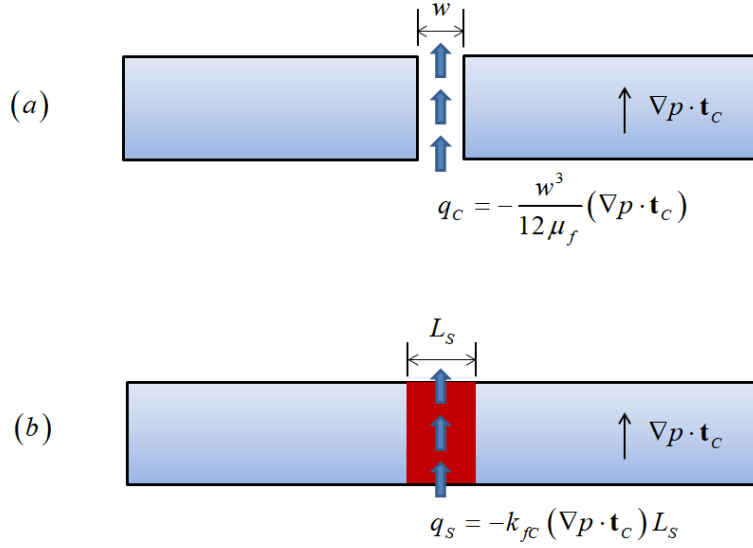


Figure 5.1 Illustration of (a) the fluid flux q_c along a discrete fracture with crack opening w and (b) the fluid flux q_s over the smeared crack zone with width L_s , where a constant fluid pressure gradient $(\nabla p \cdot \mathbf{t}_c)$ exists along the crack path direction.

Firstly, as the crack opening displacement is much smaller than the other length scales of a fracture, the fluid flow inside a discrete fracture can be approximated as laminar flow between two parallel plates which correspond to the opposite surfaces of a fracture. Assuming that the fluid is Newtonian, the total fluid flux q_c across the fracture opening can be obtained as

$$q_c = -\frac{w^3}{12\mu_f} (\nabla p \cdot \mathbf{t}_c) \quad (5.9)$$

where w is the distance between the plates (i.e., the crack opening displacement), μ_f is the dynamic viscosity of the fluid, \mathbf{t}_c is a unit vector along the crack path direction.

Next, under the smeared crack modeling framework, the fluid flux q_s along the crack path direction over the smeared crack zone can be expressed as

$$q_s = -k_{fC} (\nabla p \cdot \mathbf{t}_C) L_s \quad (5.10)$$

where L_s represents the smeared crack zone's width (along the direction perpendicular to the crack path) as illustrated in Figure 5.1. Under the damage particle-based meshfree discretization, L_s can be evaluated as the ratio between the nodal representative volume V_I and the effective surface area A_I^{eff} of the crack segment associated with damaged particle I , as defined previously in Chapter 4.

Considering (5.7) and (5.8) and further enforcing the flow flux equivalence:

$$q_s = q_C \quad (5.11)$$

the following permeability parameter which describes the hydraulic behaviors of the porous media along the crack path direction is yielded:

$$k_{fC} = \frac{w^3}{12\mu_f L_s} \quad (5.12)$$

The above expression for k_{fC} is then employed in the anisotropic permeability model in (5.8), which ensures the total fluid flux conservation within the fracture.

In the numerical simulation, the anisotropic permeability model in (5.8) is employed at each damaged particle, where the storage and computation of state and field variables are also performed. For smeared description of fractures, a direct derivation of the crack opening displacement based on the damage distribution is in general not available. Nevertheless,

following the work of [Miehe et al (2015); Mauthe and Miehe (2017)] on phase field methods along with our previous analysis on the damage particle method in Chapter 4, a smeared strain-based measure for estimating the crack aperture at damage particle I can be defined as:

$$w(\mathbf{x}_I) = DL_S(\mathbf{n}_I^D \cdot \tilde{\boldsymbol{\varepsilon}}(\mathbf{x}_I) \cdot \mathbf{n}_I^D) \quad (5.13)$$

where $\tilde{\boldsymbol{\varepsilon}}(\mathbf{x}_I)$ is the smeared strain at particle I , \mathbf{n}_I^D is the unit normal vector to the crack segment at particle I . The validity of this formulation in one-dimension has actually been demonstrated in Section 4.3.1, and its effectiveness in multi-dimensions will be further examined in Example 5.2.1. Algorithms for updating the damage state D in conjunction with the dissipation energy-based regularization follow closely the formulations introduced in Chapter 4.

5.2 Reproducing Kernel Mixed Formulation

5.2.1 Variational equations

Following a similar procedure as described in previous chapters, the variational equations can be derived for the momentum and mass balance equations in (5.1)-(5.2). By partitioning the domain Ω into conforming nodal representative domains associated with a set of points, $\Omega = \bigcup_{I=1}^{NP} \Omega_I$, where NP is the number of meshfree nodes, and introducing the reproducing kernel approximation to both the trial and test functions, the following semi-discrete form of the fluid pressure projection-based variational equations are obtained

$$\int_{\Omega} (\nabla^s \boldsymbol{\eta}^h : [\mathbb{I} - \mathbf{D}] : \bar{\boldsymbol{\sigma}}'' - \alpha p^h \nabla \cdot \boldsymbol{\eta}^h) d\Omega + \int_{\Omega} \boldsymbol{\eta}^h \cdot \rho \ddot{\mathbf{u}}^h d\Omega - \int_{\Gamma_t} \boldsymbol{\eta}^h \cdot \bar{\mathbf{t}} d\Gamma - \int_{\Omega} \boldsymbol{\eta}^h \cdot \rho \mathbf{g} d\Omega = 0 \quad (5.14)$$

$$\begin{aligned}
& \int_{\Omega} \alpha \psi^h \nabla \cdot \mathbf{u}^h d\Omega + \int_{\Omega} \psi^h \frac{1}{Q} \dot{p}^h d\Omega + \int_{\Omega} \nabla \psi^h \cdot \mathbf{k}_f \cdot \nabla p^h d\Omega - \int_{\Omega} \nabla \psi^h \cdot \mathbf{k}_f \cdot \rho_f \mathbf{g} d\Omega \\
& + \int_{\Gamma_q} \psi^h \mathbf{n}_{\Gamma} \cdot \bar{\mathbf{q}}_f d\Gamma + \int_{\Omega} \varepsilon_f (\psi^h - \Pi \psi^h) (p^h - \Pi p^h) d\Omega = 0
\end{aligned} \tag{5.15}$$

in which

$$\mathbf{u}^h = \mathbf{N}^u \mathbf{U} = \sum_{I=1}^{NP} N_I \mathbf{U}_I, \quad \boldsymbol{\eta}^h = \mathbf{N}^u \mathbf{c}^u = \sum_{I=1}^{NP} N_I \mathbf{c}_I^u \tag{5.16}$$

are the reproducing kernel approximated trial and test functions for the solid displacement, respectively, and

$$p^h = \mathbf{N}^p \mathbf{P} = \sum_{I=1}^{NP} N_I P_I, \quad \boldsymbol{\psi}^h = \mathbf{N}^p \mathbf{c}^p = \sum_{I=1}^{NP} N_I c_I^p \tag{5.17}$$

are the reproducing kernel approximated trial and test functions for fluid pressure, respectively, where \mathbf{N}^u and \mathbf{N}^p are the matrices of reproducing kernel shape functions, and \mathbf{U} , \mathbf{P} , \mathbf{c}^u and \mathbf{c}^p are vectors of the corresponding nodal coefficients; $\Pi(\cdot)$ in (5.15) denotes the L_2 projection operator for the fluid pressure approximation field, which is employed in the pressure projection-based stabilization scheme to ensure stable equal-order reproducing kernel approximation, as discussed in Chapter 3.

5.2.2 Discrete equations

For time discretization, the generalized Newmark scheme is applied to the solid motion fields:

$$\ddot{\mathbf{u}}_{n+1}^h = \frac{1}{\beta_2 \Delta t^2} \Delta \mathbf{u}_{n+1}^h - \frac{1}{\beta_2 \Delta t} \dot{\mathbf{u}}_n^h + \left(1 - \frac{1}{2\beta_2}\right) \ddot{\mathbf{u}}_n^h \quad (5.18)$$

$$\dot{\mathbf{u}}_{n+1}^h = \frac{\beta_1}{\beta_2 \Delta t} \Delta \mathbf{u}_{n+1}^h + \left(1 - \frac{\beta_1}{\beta_2}\right) \dot{\mathbf{u}}_n^h + \left(1 - \frac{\beta_1}{2\beta_2}\right) \Delta t \ddot{\mathbf{u}}_n^h \quad (5.19)$$

$$\mathbf{u}_{n+1}^h = \mathbf{u}_n^h + \Delta \mathbf{u}_{n+1}^h \quad (5.20)$$

and the generalized trapezoidal rule is applied to the fluid pressure field:

$$\dot{p}_{n+1}^h = \frac{1}{\theta \Delta t} \Delta p_n^h + \left(1 - \frac{1}{\theta}\right) \dot{p}_n^h \quad (5.21)$$

$$p_{n+1}^h = p_n^h + \Delta p_n^h \quad (5.22)$$

where Δt denotes the time step size. In the present study, the trapezoidal rule with integration parameters $\beta_1 = 1/2$, $\beta_2 = 1/4$, $\theta = 1/2$ is adopted. Substituting (5.18)-(5.22) into the spatial discrete equations (5.14)-(5.15), we obtain the following system of discrete equations:

$$\mathbf{R}_{n+1}^u \equiv \mathbf{F}_{n+1}^{(E)} - \mathbf{F}_{n+1}^{(U)} - \mathbf{M}_{n+1} \left[\frac{1}{\beta_2 \Delta t^2} \Delta \mathbf{U}_{n+1} - \frac{1}{\beta_2 \Delta t} \dot{\mathbf{U}}_n + \left(1 - \frac{1}{2\beta_2}\right) \ddot{\mathbf{U}}_n \right] + \mathbf{K}_{n+1}^{(C)} \mathbf{P} = \mathbf{0} \quad (5.23)$$

$$\begin{aligned} \mathbf{R}_{n+1}^p \equiv & \left(\frac{\beta_2 \Delta t}{\beta_1} \right) \mathbf{Q}_{n+1}^{(E)} - \frac{\beta_2 \Delta t}{\beta_1} \left(\mathbf{K}_{n+1}^{(H)} + \mathbf{S}_{n+1} \right) \mathbf{P}_{n+1} - \mathbf{K}_{n+1}^{(S)} \left(\frac{\beta_2}{\beta_1 \theta} \Delta \mathbf{P}_{n+1} + \frac{(\theta-1)\beta_2 \Delta t}{\beta_1 \theta} \Delta \dot{\mathbf{P}}_n \right) \\ & - \left[\mathbf{K}_{n+1}^{(UP)} \right]^T \left(\Delta \mathbf{U}_{n+1} - \left(1 - \frac{\beta_2}{\beta_1}\right) \Delta t \dot{\mathbf{U}}_n - \left(\frac{1}{2} - \frac{\beta_2}{\beta_1}\right) \Delta t^2 \ddot{\mathbf{U}}_n \right) = \mathbf{0} \end{aligned} \quad (5.24)$$

in which the internal force vector $\mathbf{F}_{n+1}^{(U)}$ is dependent on the damage state $D_{n+1}(\tilde{\boldsymbol{\varepsilon}}_{n+1})$ and the undamaged effective stress vector $\bar{\boldsymbol{\Sigma}}_{n+1}''$ as

$$\mathbf{F}_{n+1}^{(U)} = \int_{\Omega} \mathbf{B}^{uT} [1 - D_{n+1}(\tilde{\boldsymbol{\varepsilon}}_{n+1})] \bar{\boldsymbol{\Sigma}}_{n+1}'' d\Omega \quad (5.25)$$

where \mathbf{B}^u is the matrix consisting of the shape function gradients. In addition, the mass matrix \mathbf{M}_{n+1} , coupling matrix $\mathbf{K}_{n+1}^{(C)}$, permeability matrix $\mathbf{K}_{n+1}^{(H)}$, compressibility matrix $\mathbf{K}_{n+1}^{(S)}$, stabilization matrix \mathbf{S} , and the external force vectors $\mathbf{F}_{n+1}^{(E)}$ and $\mathbf{Q}_{n+1}^{(E)}$ are expressed as follows

$$\mathbf{M}_{n+1} = \int_{\Omega} \mathbf{N}^{uT} \rho_{n+1} \mathbf{N}^u d\Omega, \quad (5.26)$$

$$\mathbf{K}_{n+1}^{(C)} = \int_{\Omega} \mathbf{B}^{uT} \alpha_{n+1} \mathbf{m} \mathbf{N}^p d\Omega, \quad (5.27)$$

$$\mathbf{K}_{n+1}^{(H)} = \int_{\Omega} \mathbf{B}^{pT} (\mathbf{k}_f)_{n+1} \mathbf{B}^p d\Omega \quad (5.28)$$

$$\mathbf{K}_{n+1}^{(S)} = \int_{\Omega} \mathbf{N}^{pT} (1/Q_{n+1}) \mathbf{N}^p d\Omega \quad (5.29)$$

$$\mathbf{S}_{n+1} = \int_{\Omega} (\varepsilon_f)_{n+1} [\mathbf{N}^p - \Pi \mathbf{N}^p]^T [\mathbf{N}^p - \Pi \mathbf{N}^p] d\Omega \quad (5.30)$$

$$\mathbf{F}_{n+1}^{(E)} = \int_{\Gamma_t} \mathbf{N}^{uT} \bar{\mathbf{t}}_{n+1} d\Gamma + \int_{\Omega} \mathbf{N}^{uT} \rho_{n+1} \mathbf{g} d\Omega \quad (5.31)$$

$$\mathbf{Q}_{n+1}^{(E)} = - \int_{\Gamma_q} \mathbf{N}^{pT} \mathbf{n}_{\Gamma} (\bar{\mathbf{q}}_f)_{n+1} d\Gamma + \int_{\Omega} \mathbf{B}^{pT} (\mathbf{k}_f)_{n+1} \rho_f \mathbf{g} d\Omega \quad (5.32)$$

In (5.30), the parameter ε_f for the pressure projection-based stabilization follows Sun et al.

[Sun, Ostien, Salinger (2013)], which is chosen to avoid spurious pressure oscillations in uncracked and low-permeable region, as described in (3.53) and (3.54) of Section 3.3; in other region represented by damaged particles, however, the cracking-enhanced permeability is sufficiently high, and thus this parameter is locally set to zero to avoid numerical stabilization-induced over diffusion.

Finally, the incremental solid displacement $\Delta \mathbf{U}_{n+1}$ and fluid pressure $\Delta \mathbf{P}_{n+1}$ as the primary nodal unknowns can be obtained by an iterative algorithm to solve the non-linear equations (5.23)-(5.24). For the i^{th} iteration of the $(n+1)^{\text{th}}$ time step, the final system of equations are as follows

$$\mathbf{J}_{n+1}^i \begin{Bmatrix} \Delta \mathbf{U}_{n+1}^i \\ \Delta \mathbf{P}_{n+1}^i \end{Bmatrix} = \begin{Bmatrix} (\mathbf{R}_{n+1}^u)^i \\ (\mathbf{R}_{n+1}^p)^i \end{Bmatrix} \quad (5.33)$$

in which the residual vectors $(\mathbf{R}_{n+1}^u)^i = \mathbf{R}_{n+1}^u(\mathbf{U}_{n+1}^i, \mathbf{P}_{n+1}^i)$ and $(\mathbf{R}_{n+1}^p)^i = \mathbf{R}_{n+1}^p(\mathbf{U}_{n+1}^i, \mathbf{P}_{n+1}^i)$ are calculated based upon (5.23) and (5.24), where the superscript i is the iteration counter. The Jacobian matrix \mathbf{J}_{n+1}^i by consistent linearization is expressed as

$$\begin{aligned}
\mathbf{J}_{n+1}^i &= \begin{bmatrix} \frac{\partial(\mathbf{R}_{n+1}^u)^i}{\partial \mathbf{U}_{n+1}^i} & \frac{\partial(\mathbf{R}_{n+1}^u)^i}{\partial \mathbf{P}_{n+1}^i} \\ \frac{\partial(\mathbf{R}_{n+1}^p)^i}{\partial \mathbf{U}_{n+1}^i} & \frac{\partial(\mathbf{R}_{n+1}^p)^i}{\partial \mathbf{P}_{n+1}^i} \end{bmatrix} \\
&= \begin{bmatrix} \frac{1}{\beta_2 \Delta t^2} \mathbf{M}_{n+1}^i + \mathbf{K}_{n+1}^{(U)i} & -\mathbf{K}_{n+1}^{(C)i} \\ -\mathbf{K}_{n+1}^{(C)iT} - \frac{\beta_2 \Delta t}{\beta_1} \frac{\partial \mathbf{K}_{n+1}^{(H)i}}{\partial \mathbf{U}_{n+1}^i} & -\frac{\beta_2 \Delta t}{\beta_1} (\mathbf{K}_{n+1}^{(H)i} + \mathbf{S}_{n+1}^i) - \frac{\beta_2}{\beta_1 \theta} \mathbf{K}_{n+1}^{(S)i} \end{bmatrix}
\end{aligned} \tag{5.33}$$

where the sub-matrix of the tangent stiffness $\mathbf{K}_{n+1}^{(U)i}$ for the solid phase is expressed as

$$\mathbf{K}_{n+1}^{(U)i} = \int_{\Omega} \mathbf{B}^p \mathbf{T} (\mathbf{C}^d)_{n+1}^i \mathbf{B}^p d\Omega \tag{5.34}$$

with the following material tangent stiffness matrix:

$$(\mathbf{C}_{IJ}^d)_{n+1}^i = (1 - D_{n+1}^i) \mathbf{C}_{IJ}^e - \mathbf{C}_{IK}^e (\tilde{\boldsymbol{\epsilon}}_K)_{n+1}^i \left(\frac{\partial D}{\partial \mathcal{E}_{eq}} \left(\frac{\partial \mathcal{E}_{eq}}{\partial \tilde{\boldsymbol{\epsilon}}_J} \right) \right)_{n+1}^i \tag{5.35}$$

For different damage laws, analytical expression of $(\mathbf{C}_T)_{n+1}^i$ are readily available based upon the procedure described in [Jirásek and Patzák (2002)], and the derivation details are omitted here for the sake of simplicity.

As can be seen from (5.33), the Jacobian matrix is non-symmetric due to the sub-matrix

$\frac{\beta_2 \Delta t}{\beta_1} \frac{\partial \mathbf{K}_{n+1}^{(H)i}}{\partial \mathbf{U}_{n+1}^i}$ located at the left bottom ‘p-u’ block. This sub-matrix is resulted from the

nonlinear dependence of the anisotropic permeability matrix $\mathbf{K}_{pp}^{(H)}$ (defined in (5.8) and (5.12))

on the crack opening displacement w , which further depends on the damage state D and the smeared strain $\tilde{\boldsymbol{\varepsilon}}$, according to (5.13). Note that this sub-matrix is non-zero only in a very small portion of the overall Jacobian matrix \mathbf{J}_{n+1}^i associated with damaged particles, whereas it has zero value elsewhere since a constant permeability model in (5.7) is employed for undamaged regions. In order to restore the symmetry of the Jacobian matrix, this sub-matrix is omitted in the subsequent computation. By doing so, a significant amount of computer storage is saved, and high computational efficiency in solving large-scale systems of equations is achieved. Similar symmetrization treatments have been employed in previous studies [Ráthoré de Borst, Abellan (2007); Segura, Carol (2008); Khoei, Vahab, Haghghat, Moallemi (2014)] for coupled hydro-mechanical modeling of fractured porous media, where the contribution of the additional coupling term due to the cracking-enhanced fluid flow is shown to be negligible to achieve convergence, although slightly higher number of iterations are needed. With this simplification, the Jacobian matrix \mathbf{J}_{n+1}^i adopted in the present study is expressed as

$$\mathbf{J}_{n+1}^i = \begin{bmatrix} \frac{1}{\beta_2 \Delta t^2} \mathbf{M}_{n+1}^i + \mathbf{K}_{n+1}^{(U)i} & -\mathbf{K}_{n+1}^{(C)i} \\ -\mathbf{K}_{n+1}^{(C)iT} & -\frac{\beta_2 \Delta t}{\beta_1} \left(\mathbf{K}_{n+1}^{(H)i} + \mathbf{S}_{n+1}^i \right) - \frac{\beta_2}{\beta_1 \theta} \mathbf{K}_{n+1}^{(S)i} \end{bmatrix} \quad (5.36)$$

To enhance computational accuracy and efficiency, the stabilized conforming nodal integration (SCNI) scheme is applied for the domain integration of the Jacobian matrix and residual force vectors. As discussed in previous chapters, the employment of SCNI also allows the effective implementation of the dissipation energy-based regularization scheme for the computation of damage state $D_{n+1}(\tilde{\boldsymbol{\varepsilon}}_{n+1})$, which avoids the discretization size sensitivity issues.

5.3 Numerical Examples

5.3.1 Sneddon's pressurized crack problem

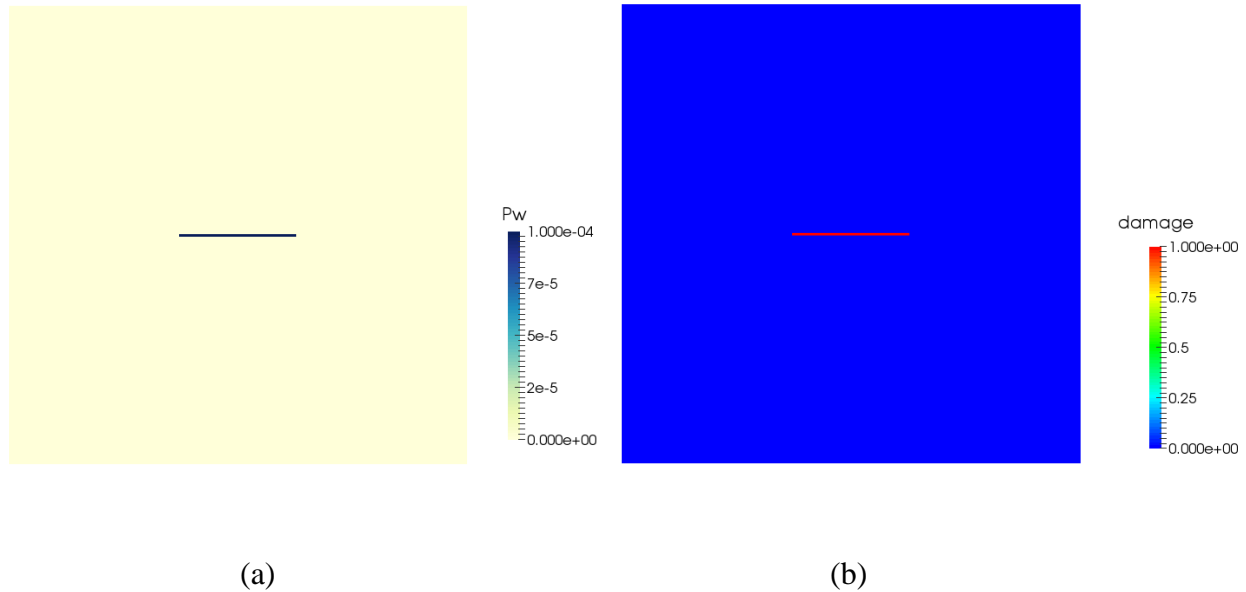


Figure 5.2 Distribution of the imposed (a) fluid pressure and (b) damage state, which indicates the location of the pre-existing crack

The first example analyzes the opening of a pre-existing crack subjected to a uniform internal pressure. A 2-D squared domain of length 4 is considered, where a straight crack with length $2c=1$ is centered at the origin and aligned with the x-axis of the Cartesian coordinate system. The elastic material properties are: Young's modulus $E=1$, Poisson's ratio $\nu=0.25$, and a uniform pressure $\bar{p}=10^{-4}$ is applied along the crack surface.

In the present study, the displacement field is restrained at the outer boundary of the square domain as an approximated boundary condition for an infinite domain problem, and the pre-existing crack is approximated by specifying the damage state $D=1$ for the particles whose

supports cover the crack location. Although the fluid flow is not considered in this example, the hydro-mechanical coupled simulation framework is still adopted, which allows the imposition of non-zero fluid pressure as the driving force to open the pre-existing crack. Specifically, we impose the fluid pressure $p = \bar{p}$ at these damaged particles and $p = 0$ elsewhere in the domain [refer to Figure 5.2].

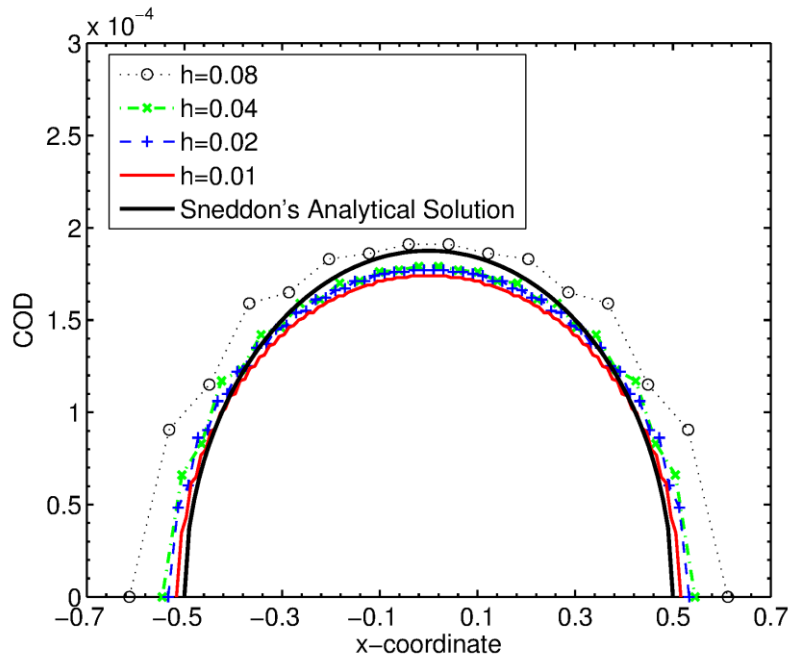


Figure 5.3 COD (Crack Opening Displacement) distribution along the crack surface, where h corresponds to the nodal distance.

Theoretical analysis of a similar pressurized crack problem has been performed in [Sneddon (1946)], and the following expression for the crack opening displacement (COD) under the plane strain condition has been obtained:

$$COD = \frac{4(1-\nu^2)\bar{p}}{E} \sqrt{c^2 - x^2} \quad (5.37)$$

The above equation has been adopted to examine the validity of smeared numerical models for

hydraulic fractures, e.g., in [Wheeler, Wick & Wollner (2014); Santillán, Juanes & Cueto-Felgueroso (2018)]. In Figure 5.3, the predicted crack opening displacement based on the equation (5.11) is plotted, using four different discretizations. As can be seen, the absolute values of the numerical solutions differ slightly from the analytical solution, which is expected as the adopted smeared crack model does not incorporate the singular stress field at the crack tips, and a low residual strength is kept in the damage model to ensure numerical convergence. Nevertheless, the damage particle method shows converge upon discretization refinement, and overall speaking, the results are in good agreement with Sneddon’s analytical solution. In addition, the distribution of the predicted displacement and stress fields plotted in Figure 5.4 (a-b) clearly demonstrates the capability of the proposed smeared approach to modeling cracks under the action of internal pressure, which is the key feature of hydraulic fractures.

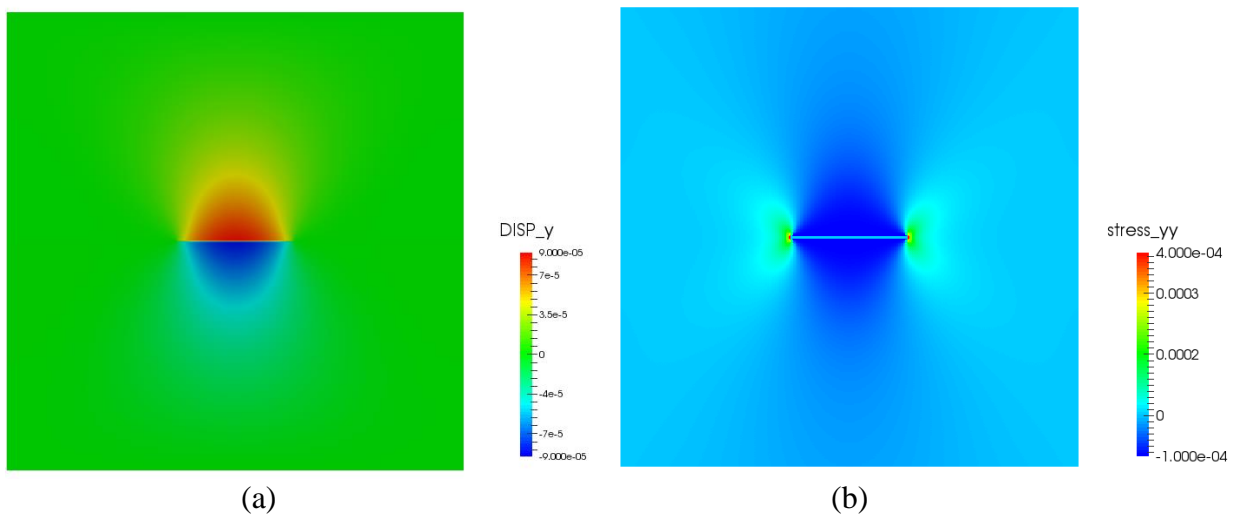


Figure 5.4 Distribution of the predicted (a) displacement in the y direction, and (b) stress component normal to the crack surface direction

5.3.2 Fluid injection-induced crack propagation in porous media

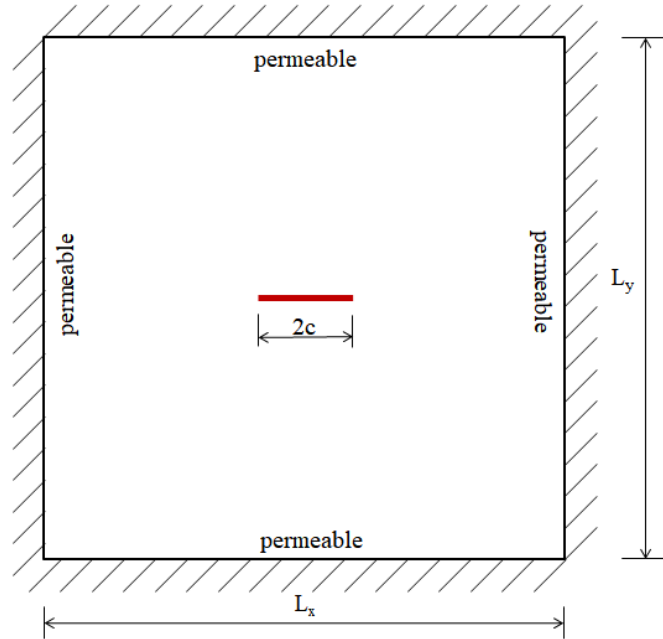


Figure 5.5 Illustration of a fluid-saturated plate with a pre-existing crack (denoted by the red line)

This example simulates hydraulic fracturing of a fluid-saturated plate subjected to fluid injection. The problem set-up follows [Ehlers and Luo (2017)] and differs from the previous Example 5.2.1 in the following aspects: (1) Instead of a single phase solid, the bulk material is treated here as fluid-saturated and permeable, and the hydro-mechanical coupling effects are incorporated in the analysis; (2) The crack is allowed to grow under the increasing pressure of the fluid injected at the central notch of the plate. The geometry and boundary conditions are displayed in Figure 5.5, where the edge length is $L_x = L_y = 1.0$ m and the initial crack has length $2c = 0.2$ m. The loading in the notch is imposed by prescribing a uniform fluid pressure of $\bar{p} = 5.5 \times 10^4 t$ (Pa), where t denotes time (with ‘second’ as the unit). The material properties are as follows: Young’s modulus $E = 2.1 \times 10^{11}$ Pa, Poisson’s ratio $\nu = 0.3$, solid mass density

$\rho^s = 3000 \text{ kg/m}^3$, fluid mass density $\rho^w = 1000 \text{ kg/m}^3$, porosity $n^f = 0.2$, hydraulic conductivity $k_h = 1 \times 10^{-8} \text{ m/s}$, specific weight of the fluid $\gamma^w = 10^4 \text{ Pa/m}$, fluid bulk modulus $K^w = 2 \times 10^9 \text{ Pa}$, solid grain bulk modulus $1 \times 10^{11} \text{ Pa}$, fracture energy $G_F = 2.7 \times 10^3 \text{ N/m}$, and tensile strength $f_t = 2.1 \times 10^7 \text{ Pa}$.

The predicted evolution of the fluid pressure and the damage state distribution is displayed in Figure 5.6. As can be seen, the fluid pressure causes the propagation of the fracture, and meanwhile the fluid pressure increases around the cracking region due to hydro-mechanical coupling which reduces the flow resistance along the fracture. These simulation results qualitatively agree well with the numerical study in [Ehlers and Luo (2017)], where the finite element-based phase field formulation (with quadratic and linear approximations for solid displacement and fluid pressure/phase field, respectively) is adopted.

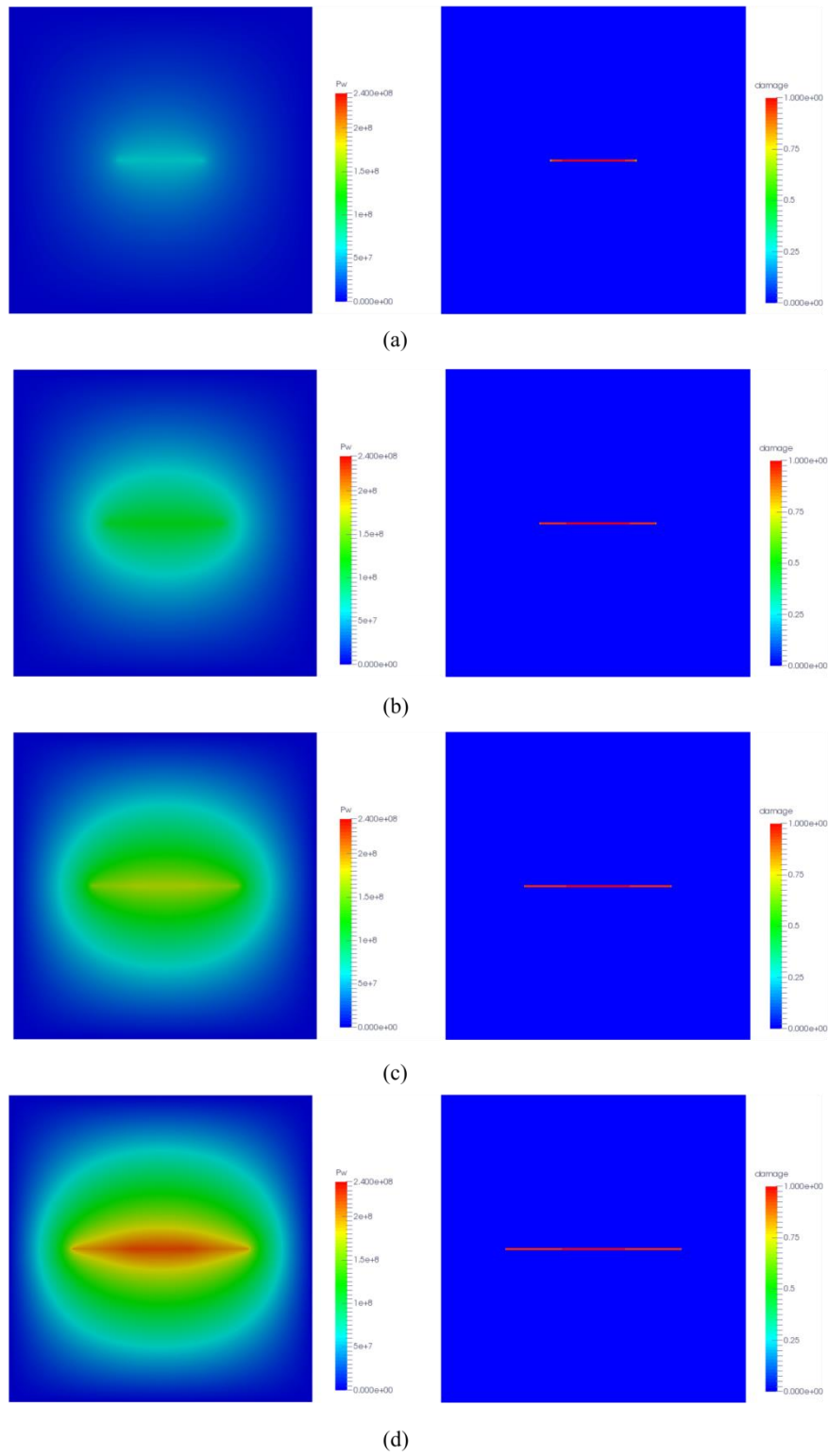


Figure 5.6 Progressive evolution of (left) the fluid pressure and (right) the damage state at time $t = 1000s, 2000s, 3000s, 4000s$ in (a)–(d) respectively.

Furthermore, Figure 5.7 displays the fluid pressure field (as the background color), along with the corresponding Darcy velocity field (as the vector plot), obtained with different levels of discretizations. It clearly shows that the fluid flows from the fracture towards the permeable boundaries. Moreover, high fluid velocities are observed in the cracking region with enhanced permeability and high pressure gradients, which is in line with the numerical results in [Ehlers and Luo (2017)]. The different levels of model refinement yield nearly identical prediction shown in Figure 5.7(a) and Figure 5.7(b), which demonstrates the convergent behavior of the proposed meshfree method for modelling hydraulic fracturing in saturated porous media.

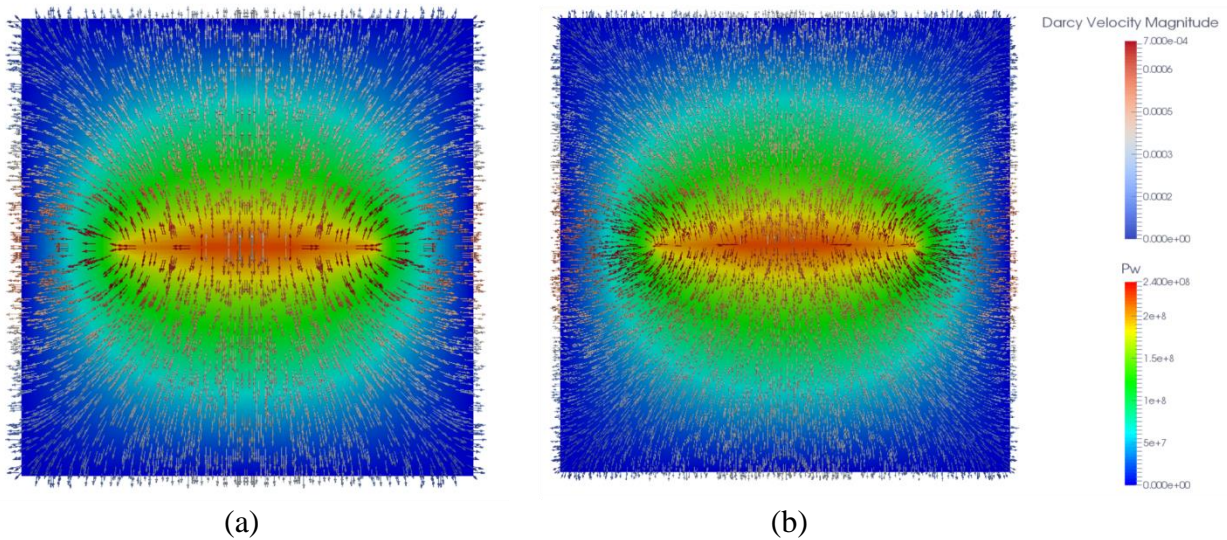


Figure 5.7 Fluid pressure and the associated Darcy velocity distribution at the end of the simulation using (a) coarse (nodal distance $h = 5 \times 10^{-3}$ m) and (b) refined ($h = 2.5 \times 10^{-3}$ m) discretizations.

5.3.3 Blanton's hydraulic fracturing tests

Hydraulic fractures are expected to cross and connect the natural fracture system to form a permeable fracture network. However, fracture arrest, diversion, or offset could occur due to the interaction between hydraulically induced and pre-existing fractures, thus the fracture growth and proppant placement can be inhibited. Therefore, prediction of these various types of fracture behaviors is important in designing an effective hydraulic fracture treatment. Over the years, a number of experimental studies have been carried out to investigate the formation of complex fracture networks due to the interaction between hydraulically induced and pre-existing fractures. For instance, the laboratory experiments in [Blanton (1982)] reveal that hydraulic fractures tend to cross pre-existing fractures only under high differential stresses and high angles of approach, while in other test cases the hydraulic fractures can be arrested by pre-existing fractures. As pointed out by [Weng (2015)], once fluid pressure exceeds the closure stress of the natural fractures, the natural fractures can open up and become a part of the hydraulic fracture network, and a pre-existing fracture can turn itself to align with the preferred crack growth direction and form a T-shaped branch when the fluid pressure flows into its crack tip. [Zhou et al. (2008)] analyzed different interaction types between hydraulic and pre-existing fractures through a series of tri-axial fracturing experiments, and concluded that the shear strength of pre-fractures is another key factor that influences the fracture propagation behavior.

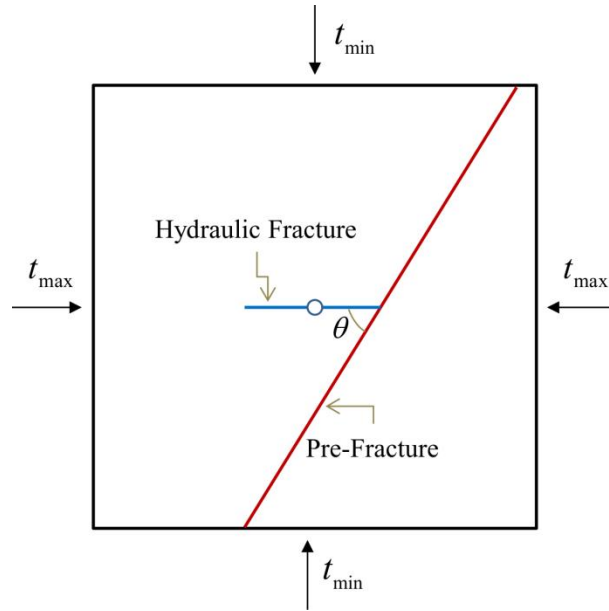


Figure 5.8 Illustration of hydraulic fracture and pre-fracture location

In the present study, the proposed meshfree formulation is applied for modeling the interaction between hydraulically induced fractures and pre-existing fractures, following the experimental work in [Blanton (1982)]. As depicted in Figure 5.8, Blanton's hydraulic fracturing experiments were run in hydrostone blocks of $0.305 \times 0.305 \times 0.381 \text{ m}^3$, where pre-existing fractures with a specified orientation were created. In addition, a central borehole was drilled for fluid injection. On the surfaces of each block, a vertical confining stress of 20 MPa was applied in all tests (along the out-of-plane direction of the 2D illustrative in Figure 5.7), while confining stresses in the horizontal directions were varied as listed in Table 5.1. As can be seen from the table, the two blocks had two tests run in each of them. This was done by switching the maximum and minimum horizontal stresses after the first test so that the second hydraulic fracture can propagate at a right angle to the first.

Table 5.1 Experimental Conditions in [Blanton (1982)]

Block #	Test #	Pre-fracture orientation θ	Maximum Horizontal Traction (MPa)	Minimum Horizontal Traction (MPa)	Observed Fracture Interaction Mode
1	CT-4	60°	12	10	Arrest
1	CT-7	30°	19	10	Arrest
2	CT-8	60°	20	5	Cross
2	CT-9	30°	20	5	Arrest

Under the plain strain assumption, a 2-D numerical model for the horizontal cross section of the hydrostone blocks is developed in the present study. A constant fluid pressure of 17 MPa and 15 MPa are imposed at the central location of the block for CT-4/CT-7 and CT-8/CT-9 tests, respectively. The horizontal tractions listed in Table 5.1 are applied on the boundary surface to generate the initial in-situ stress state. Following the experimental procedure in [Blanton (1982)], after the first hydraulic fracture grows to a desired distance, the traction boundary condition and the associated in-situ stress is modified so that another hydraulic fracture is allowed to grow in a direction perpendicular to the previous hydraulic fracture. The adopted material properties are as follows: Young's modulus $E = 1.0 \times 10^{10}$ Pa, Poisson's ratio $\nu = 0.22$, solid mass density $\rho^s = 1.9 \times 10^3$ kg/m³, fluid mass density $\rho^w = 1.0 \times 10^3$ kg/m³, porosity $n^f = 0.2$, hydraulic conductivity $k_h = 1.0 \times 10^{-8}$ m/s, specific weight of the fluid $\gamma^w = 1.0 \times 10^4$ Pa/m, fluid bulk modulus $K^w = 2.2 \times 10^9$ Pa, solid grain bulk modulus 1.0×10^{11} Pa, fracture energy $G_F = 35.0$ N/m, tensile strength $f_t = 5.0 \times 10^6$ Pa.

To incorporate the pre-existing fracture (shown as the red line in Figure 5.8) in the simulation domain, the diffraction method [Organ et al. (1996)] is introduced, which modifies the nodal support in order to capture the displacement discontinuities $[\mathbf{u}(\mathbf{x})]$ across the pre-fracture surface Γ_C . When the pre-fracture surface is in contact (i.e., $g_N \leq 0$, where $g_N(\mathbf{x}) = [\mathbf{u}(\mathbf{x})] \cdot \mathbf{n}_C(\mathbf{x})$ ($\mathbf{x} \in \Gamma_C$) denotes the aperture of the pre-fracture with outward unit normal vector \mathbf{n}_C), a penalty method [Liu and Borja (2008); Prevost and Sukumar (2016)] is adopted to impose the following frictional contact constraints:

$$t_N = p + |k_N g_N| \quad (5.38)$$

$$t_T = \begin{cases} -k_T g_T & \text{if } \|k_T g_T\| - \mu_C (t_N - p) < 0 \\ -\mu_C (t_N - p) g_T & \text{otherwise} \end{cases} \quad (5.39)$$

in which t_N and t_T are the normal and tangential components of the total traction vector applied on the pre-fracture surface Γ_C , g_N and g_T are the normal and tangential components of the displacement jump across the pre-fracture surface, k_N and k_T are the penalty parameters associated with normal and tangential contact, p is the fluid pressure in porous media, and μ_C is the frictional coefficient taken to be 0.7 in the present study. Following the geomechanics convention, a positive sign of p and t_N denotes a compressive pressure. When the pre-fracture is opened (i.e., $g_N > 0$), its surface Γ_C is subjected to the fluid pressure p only. In addition, the hydraulic behavior of an opened pre-fracture is described by the anisotropic permeability model defined in equation (5.8), where the fracture opening displacement $\omega = g_N$. On the other hand, as closed pre-fractures (i.e., $g_N < 0$) are usually poor conduits for fluid movement [Prevost and Sukumar (2016)], a permeability which is two orders of magnitude lower than the host rock's permeability is assigned to the meshfree particles whose support cover

the pre-fracture.

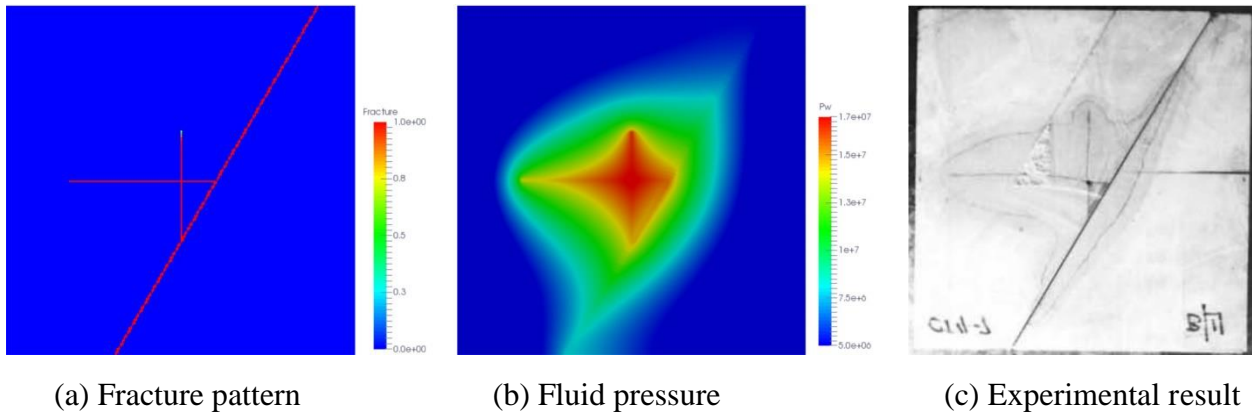


Figure 5.9 Modeling results of Blanton's CT-4/CT-7 tests where hydraulic fractures are arrested by a pre-fracture. The picture in (c) is taken from [Blanton (1982)].

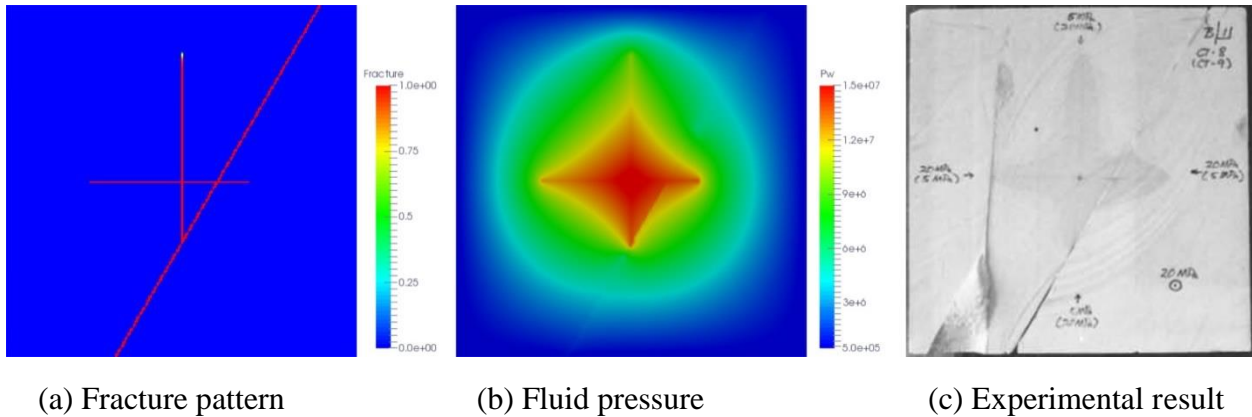


Figure 5.10 Modeling results of Blanton's CT-8/CT-9 tests where hydraulic fractures cross and arrested by a pre-fracture. The picture in (c) is taken from [Blanton (1982)].

The simulation results of the fracture pattern and fluid pressure distribution for the test cases CT-4/CT-7 and CT8/CT-9 are plotted in Figure 5.9 and Figure 5.10, respectively. It is worth to mention that, although the fractures are all visualized in red color, the hydraulic fractures and the pre-existing fractures are respectively modeled by the damaged particles and the diffraction method, as described previously. As shown in Figure 5.9, at the time of fracture intersection in the tests CT-4/CT-7, the fluid pressure is sufficiently high so that opening of the pre-existing fracture occurs, which allows fluid flow along the pre-existing fracture. As a result,

the hydraulic fractures cannot transmit to the other side of the pre-existing fracture. On the other hand, when the fluid pressure is not high enough to open up the pre-fracture, the hydraulic fracture can either be arrested or cross the pre-fracture, depending on the frictional behavior of the material interface as analyzed by [Blanton (1982)]. If the friction is high, the material on the opposite side of the interface may be fractured due to high tearing stress. As shown in Figure 5.10, the hydraulic fracture in the test CT-8 approached the pre-existing fracture at a 60° angle and crossed it with each wing growing to a nearly equal length, while the hydraulic fracture approaching the pre-fracture at a 30° angle in the test CT-9 was arrested and only one of its fracture wing kept growing to a greater length. Due to the lack of test procedure details and well-calibrated material data, the experimental results cannot be fully reproduced. Nevertheless, qualitative comparison between the computational and experimental results clearly demonstrates the effectiveness of the present numerical approach in capturing the interaction behaviors between hydraulic fractures and pre-fractures.

Chapter 6

Semi-Lagrangian Reproducing Kernel Formulation for Landslide Modeling

In this chapter, the nonlinear mathematical model for partially saturated deformable porous media is reviewed in Section 6.1. Next, the semi-Lagrangian reproducing kernel approximation and implicit gradients are discussed in Section 6.2, followed by the semi-Lagrangian meshfree u-p formulation with the naturally stabilized nodal integration in Section 6.3. Finally, numerical examples are given in Section 6.4 to show the effectiveness of the proposed approach.

6.1 Review of Nonlinear Poromechanics

The mathematical description of the physical behavior of fluid-saturated porous media was first established for quasi-static phenomena in 1941 by Biot [Biot (1941)] and later extended to dynamics [Biot (1956ab)]. Owing to increasing interest in non-linear applications, Zienkiewicz et al. [Zienkiewicz et al. (1984)] generalized Biot's theory and proposed various mathematical formulations using different assumptions, among which the so-called u-p formulation (where solid displacement and pore fluid pressure are chosen as primary variables) becomes the most popular theory because of its simplicity and effectiveness. In the present study, the nonlinear u-p formulation introduced by [Zienkiewicz et al. (1990b)] for modeling partially

saturated porous media is adopted. The basic assumption of this formulation is that the pore air pressure is treated as zero (ambient atmospheric value) at all points of the domain during loading, which implies that the resistance to the flow of air is negligibly small [Kim et al (2015)]. This simplification allows us to employ a two-field u-p formulation for modeling triphasic porous media. Note that the magnitude of pore air pressure could have an important influence under certain loading conditions [Khoei & Mohammadnejad (2011); Li & Wei (2015)], but this is out of the scope of the present study. In the following, the adopted sign convention defines tensile stress of the solid phase and compressive pressure of the fluid phase as positive quantities.

6.1.1 Kinematics

Under the partially saturated condition, the voids of the skeleton in the porous media are filled with water and air. In a continuum representation of this multiphase porous media, it is assumed that the triphasic (solid, water, air) porous body can be treated as an immiscible mixture of superimposed and interacting constituents in a spatially averaged sense. This implies that each spatial point \mathbf{X} in the current configuration Ω at time t is simultaneously occupied by material points \mathbf{X}^s , \mathbf{X}^w and \mathbf{X}^a (where the superscript s , w and a denote the solid phase, water phase and air phase, respectively) as illustrated in Figure 6.1. Meanwhile, each constituent follows its own unique Lagrangian motion function:

$$\mathbf{x} = \chi^\alpha(\mathbf{X}^\alpha, t), \quad \alpha = s, w, a \quad (6.1)$$

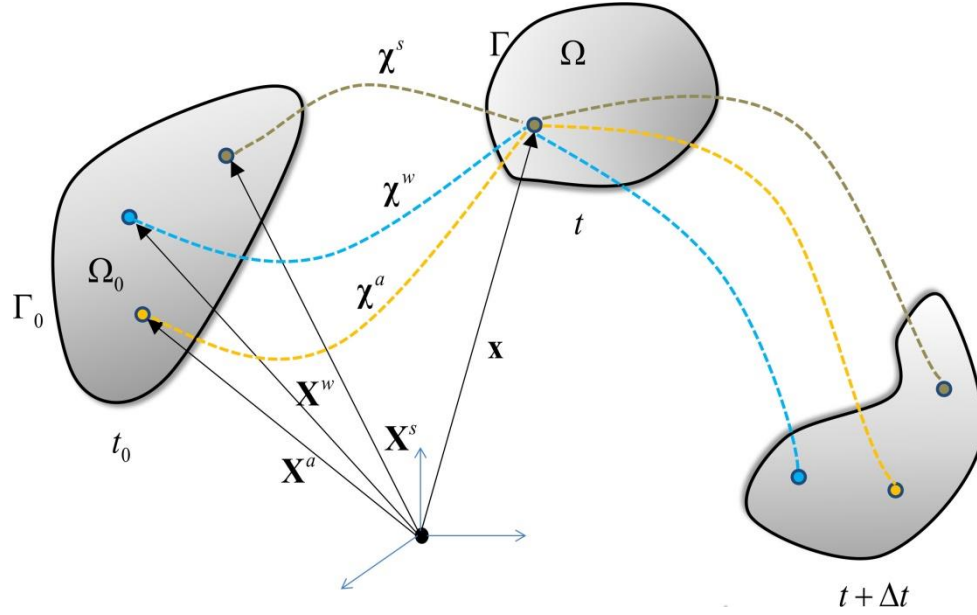


Figure 6.1 Illustration of the motion of a triphasic continuum.

Similar to single phase solids, the solid phase in the multiphase porous media can be conveniently described by a Lagrangian approach via the solid displacement $\mathbf{u} = \mathbf{x} - \mathbf{X}^s$, velocity $\mathbf{v} = \dot{\mathbf{u}}$, and acceleration $\mathbf{a} = \ddot{\mathbf{u}}$, where the superposed single and double dots denote the first and second order material time derivatives following the motion of the solid constitute, respectively. For the fluid phases, an Eulerian type description is adopted, which describes the fluid flow with reference to the moving solid skeleton in the current configuration. Hence, the water seepage velocity \mathbf{q}^w , representing the average relative velocity between the pore water and the solid, is introduced:

$$\mathbf{q}^w = n^w (\mathbf{v}^w - \mathbf{v}) \quad (6.2)$$

where n^w is the volume fraction of the water phase, \mathbf{v}^w is the water velocity. The water seepage velocity \mathbf{q}^w is chosen as the main kinematic variable for the water phase because of its

important role in the solid-fluid interaction, whereas the relative acceleration between the different constituents is very small and can be neglected, as discussed in [Zienkiewicz et al. (1999); Meroi, Schrefler, & Zienkiewicz (1995)].

6.1.2 Balance equations

Following [Zienkiewicz et al. (1990); Zienkiewicz et al. (1999)], the governing equations for a triphasic mixture include the balance of linear momentum, which can be expressed in the current configuration as

$$\nabla_{\mathbf{x}} \cdot \boldsymbol{\sigma} - \rho \ddot{\mathbf{u}} + \rho \mathbf{g} = \mathbf{0} \quad (6.3)$$

and the mass balance of water flow

$$\alpha \nabla_{\mathbf{x}} \cdot \dot{\mathbf{u}} + \nabla_{\mathbf{x}} \cdot \mathbf{q}^w + \frac{1}{Q} \dot{p}^w = 0 \quad (6.4)$$

In equations (6.3) and (6.4), $\nabla_{\mathbf{x}}$ denotes the spatial gradient operator, \mathbf{g} is the gravitational acceleration vector, ρ is the averaged mass density expressed as

$$\rho = (1 - n^f) \rho^s + n^f S^w \rho^w + n^f S^a \rho^a \approx (1 - n^f) \rho^s + n^f S^w \rho^w \quad (6.5)$$

where $n^f = n^w + n^a$ is the porosity, in which n^w and n^a are the volume fractions of water and gas phases, respectively; S^w and S^a are the degrees of water and air saturation, respectively, $S^w + S^a = 1$, and $n^f S^w$ is equivalent to the volume fraction of the water phase n^w ; ρ^s , ρ^w

and ρ^a are the real mass densities of the solid, water and gas constitues, respectively. In equation (6.5), the term of air mass $n^f S^a \rho^a$ has been omitted. The total Cauchy stress tensor $\boldsymbol{\sigma}$ in equation (6.3) is defined as

$$\boldsymbol{\sigma} = \boldsymbol{\sigma}'' - \alpha S^w p^w \mathbf{I} \quad (6.6)$$

in which $\boldsymbol{\sigma}''$ is the effective stress, the p^w represents the water pressure, \mathbf{I} is a second-order identity tensor, $\alpha = 1 - K/K^s$ is Biot's coefficient, K and K^s are the bulk modulus of the solid skeleton and the solid grain, respectively. In addition, Q in equation (6.4) is the modified compressibility modulus defined as:

$$\frac{1}{Q} = C^s + \frac{n^f S^w}{K^w} + \frac{S^w (\alpha - n^f) (S^w + C^s p^w / n^f)}{K^s} \quad (6.7)$$

where $C^s = n^f \partial S^w / \partial p^w$, and K^w is the bulk modulus of the water constitute.

6.1.3 Constitutive laws

Following the definition of the total stress given in equation (6.6) for the mixture, separate constitutive equations can be defined for the effective stress and the water pressure, respectively. For the solid phase, the Jaumann's objective rate [Meroli, Schrefler, & Zienkiewicz 1995] is adopted to take into account the large deformation effects:

$$\boldsymbol{\sigma}''^{\nabla J} = \dot{\boldsymbol{\sigma}}'' - \boldsymbol{\omega} \cdot \boldsymbol{\sigma}'' + \boldsymbol{\sigma}'' \cdot \boldsymbol{\omega} \quad (6.8)$$

in the above equation, the superscript ∇J denotes the Jaumann rate, and the spin tensor $\boldsymbol{\omega}$ is defined as

$$\boldsymbol{\omega} = \frac{1}{2}(\mathbf{L} - \mathbf{L}^T) \quad (6.9)$$

in which \mathbf{L} is the velocity gradient tensor:

$$\mathbf{L} = \nabla_x \otimes \mathbf{v} \quad (6.10)$$

The Jaumann rate of the total Cauchy stress can be calculated as follows

$$\boldsymbol{\sigma}^{\nabla J} = \mathbf{C}_T : \mathbf{D} \quad (6.11)$$

where \mathbf{C}_T is the corotational drained material moduli derived from the adopted material law, and \mathbf{D} is the tensor of rate-of-deformation:

$$\mathbf{D} = \frac{1}{2}(\mathbf{L} + \mathbf{L}^T) \quad (6.12)$$

Considering equations (6.8) and (6.11), the material time derivative of the effective stress can be written in the following incremental form:

$$\dot{\boldsymbol{\sigma}}'' = \mathbf{C}_T : \mathbf{D} + \boldsymbol{\omega} \cdot \boldsymbol{\sigma}'' - \boldsymbol{\sigma}'' \cdot \boldsymbol{\omega} \quad (6.13)$$

Regarding the fluid phase, Darcy's law is adopted to define the relationship between the water seepage velocity and the pressure gradient

$$\mathbf{q}^w = -\mathbf{k}^w \cdot (\nabla_x p^w - S^w \rho^w \mathbf{g}) \quad (6.14)$$

where $\mathbf{k}^w = (k^{rw}/\mu^w)\mathbf{k}_{in}^w$ is the permeability tensor, \mathbf{k}_{in}^w is the intrinsic permeability, μ^w and k^{rw} are the dynamic viscosity and the relative permeability of the water phase, respectively. A number of hydraulic conductivity models have been developed to describe the dependence of the permeability on the degree of water saturation S^w or soil suction $s = p^a - p^w$. In addition, the relationship between the soil suction and water content (in terms of the degree of water saturation S^w) can be provided by the soil-water characteristic curve (SWCC). Readers are referred to [Lu & Likos (2004)] for more details of different SWCC and hydraulic conductivity models for partially saturated porous materials.

6.1.4 Strong form of the u - p formulation

Expressing the total stress in equation (6.3) as the effective stress and fluid pressure with the help of equation (6.6), the momentum balance equation can be re-written as

$$\nabla_x \cdot (\boldsymbol{\sigma}'' - \alpha S^w p^w \boldsymbol{\delta}) - \rho \ddot{\mathbf{u}} + \rho \mathbf{g} = \mathbf{0} \quad (6.15)$$

Substituting (6.14) into (6.4), the mass balance equation can now be expressed as

$$\alpha \nabla_x \cdot \dot{\mathbf{u}} - \nabla_x \cdot [\mathbf{k}^w \cdot (\nabla_x p^w - S^w \rho^w \mathbf{g})] + \frac{1}{Q} \dot{p}^w = 0 \quad (6.16)$$

the above two equations form the strong form u - p formulation for a triphasic porous medium occupying a domain Ω with boundary Γ in its current configuration as shown in Figure 6.1.

The governing equations are complemented by the following boundary conditions:

$$\mathbf{u} = \bar{\mathbf{u}} \quad \text{on } \Gamma_u \quad (6.17)$$

$$\mathbf{n}_\Gamma \cdot (\boldsymbol{\sigma}'' - \alpha S^w p^w \mathbf{I}) = \bar{\mathbf{t}} \quad \text{on } \Gamma_t \quad (6.18)$$

$$p^w = \bar{p} \quad \text{on } \Gamma_p \quad (6.19)$$

$$\mathbf{n}_\Gamma \cdot \mathbf{q}^w = \mathbf{n}_\Gamma \cdot \bar{\mathbf{q}} \quad \text{on } \Gamma_q \quad (6.20)$$

and the initial conditions at time $t=0$:

$$\mathbf{u} = \mathbf{u}_0, \quad \mathbf{v} = \mathbf{v}_0, \quad \mathbf{a} = \mathbf{a}_0, \quad p^w = p_0 \quad (6.21)$$

where \mathbf{n}_Γ is the unit outer normal vector of the boundary Γ , Γ_u and Γ_p are the essential boundaries with imposed solid displacement $\bar{\mathbf{u}}$ and water fluid pressure \bar{p} , respectively, and Γ_t and Γ_q are the natural boundaries with imposed traction $\bar{\mathbf{t}}$ and water inflow flux $\bar{\mathbf{q}}$, respectively, where $\Gamma_u \cap \Gamma_t = \Gamma_p \cap \Gamma_q = \emptyset$ and $\Gamma_u \cup \Gamma_t = \Gamma_p \cup \Gamma_q = \Gamma$.

6.2 Semi-Lagrangian Reproducing Kernel Mixed Formulation

6.2.1 Semi-Lagrangian reproducing kernel approximation

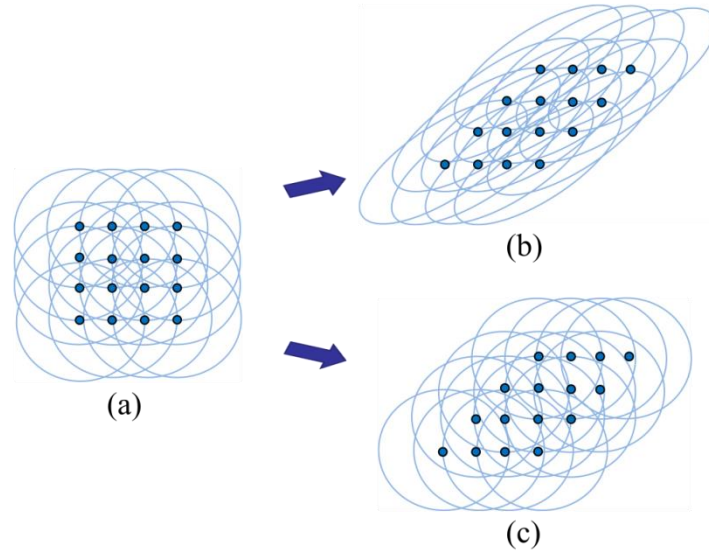


Figure 6.2 Illustration of meshfree discretization with different types of kernel functions: (a) meshfree particles with circular support in the initial configuration, (b) Lagrangian kernels in the current configuration, (c) semi-Lagrangian kernels in the current configuration.

For problems involving extreme deformation, such as material separation and flow-like behavior in the landslide processes, keeping the same set of material points in the nodal neighbor list would lead to non-physical description of the material behaviors, and also numerical difficulties arise due to the non-invertible deformation gradient. To circumvent these issues, the reproducing kernel approximation can be formulated under a semi-Lagrangian framework [Chen, & Wu (2007)], where the nodes still follow the motion of material points as a Lagrangian description, while the nodal neighbor list is updated by re-defining the kernel support coverage in the current configuration, as sketched in Figure 6.2. As a result, the semi-Lagrangian reproducing kernel approximation $f^h(\mathbf{x})$ of a function $f(\mathbf{x})$ takes the following form

$$f^h(\mathbf{X}) = \sum_{I=1}^{NP} N_I(\mathbf{X}) f_I \quad (6.22)$$

in which the semi-Lagrangian RK shape function is given as:

$$N_I(\mathbf{x}) = \mathbf{H}^T(\mathbf{0}) \cdot \mathbf{A}^{-1}(\mathbf{x}) \cdot \mathbf{H}(\mathbf{x} - \mathbf{x}_I) \Phi_a(\mathbf{x} - \mathbf{x}_I) \quad (6.23)$$

which satisfies the following n^{th} order discrete reproducing conditions in the current configuration:

$$\sum_{I=1}^{NP} N_I(\mathbf{x}) \mathbf{x}_I^\alpha = \mathbf{x}^\alpha \quad , \quad \alpha \leq n \quad (6.24)$$

In (6.23), $\mathbf{H}(\mathbf{x} - \mathbf{x}_I)$ is a vector consisting of n^{th} order monomial basis functions:

$$\mathbf{H}^T(\mathbf{x} - \mathbf{x}_I) = \left[1, \quad x - x_I, \quad y - y_I, \quad z - z_I, \quad (x - x_I)^2, \quad \dots, \quad (z - z_I)^n \right] \quad (6.25)$$

and the moment matrix is defined as follows

$$\mathbf{A}(\mathbf{x}) = \sum_{I=1}^{NP} \mathbf{H}(\mathbf{x} - \mathbf{x}_I) \otimes \mathbf{H}(\mathbf{x} - \mathbf{x}_I) \Phi_a(\mathbf{x} - \mathbf{x}_I) \quad (6.26)$$

where $\Phi_a(\mathbf{x} - \mathbf{x}_I)$ is the kernel function constructed in the current configuration. In the present study, the following cubic spline function is chosen:

$$\Phi_a(\mathbf{x} - \mathbf{x}_I) = \begin{cases} 2/3 - 4s_I^2 + 4s_I^3 & \text{for } 0 \leq s_I \leq 1/2 \\ 4/3 - 4s_I + 4s_I^2 - 4/3 s_I^3 & \text{for } 1/2 < s_I \leq 1 \\ 0 & \text{for } s_I > 1 \end{cases} \quad (6.27)$$

where $s_I = \|\mathbf{x} - \mathbf{x}_I\|/a_I$, and a_I is node I 's support size treated as a constant throughout the simulation.

Similar to the reproducing conditions in (6.24), one can also reproduce the gradients of $f(\mathbf{x})$ by enforcing the following n^{th} order discrete gradient reproducing conditions:

$$\sum_{I=1}^{NP} \mathbf{N}_I^\nabla(\mathbf{x}) \otimes \mathbf{x}_I^\alpha = \nabla_{\mathbf{x}} \otimes \mathbf{x}^\alpha, \quad \alpha \leq n \quad (6.28)$$

which results in the implicit gradient reproducing kernel shape functions:

$$N_{ii}^\nabla(\mathbf{x}) = \bar{\mathbf{H}}_i^T \cdot \mathbf{A}^{-1}(\mathbf{x}) \cdot \mathbf{H}(\mathbf{x} - \mathbf{x}_I) \Phi_a(\mathbf{x} - \mathbf{x}_I) \quad (6.29)$$

For three dimensions with linear basis, the vector $\bar{\mathbf{H}}_i$ takes on the values:

$$\bar{\mathbf{H}}_i = [0, -1, 0, 0]^T \quad (6.30)$$

$$\bar{\mathbf{H}}_i = [0, 0, -1, 0]^T \quad (6.31)$$

$$\bar{\mathbf{H}}_i = [0, 0, 0, -1]^T \quad (6.32)$$

Comparing the expressions given in equation (6.29) and equation (6.23), it can be seen that there is almost no additional cost for computing the implicit gradients, provided that the shape functions have already been constructed. Therefore, employment of the implicit gradients can significantly save computational cost compared to the expensive explicit gradients based on direct differentiation of the meshfree shape functions. Therefore, the implicit gradients are

adopted to accelerate the computation in the naturally stabilized nodal integration, to be described in Section 6.3.

6.2.2 Variational equations

The variational equations of the nonlinear dynamic u - p formulation can be expressed with reference to the current configuration as

$$\begin{aligned} L_1(\boldsymbol{\eta}^h; \mathbf{u}^h, p^h) \equiv & \int_{\Omega} \rho \boldsymbol{\eta}^h \cdot \ddot{\mathbf{u}}^h d\Omega + \int_{\Omega} (\nabla_{\mathbf{x}}^s \otimes \boldsymbol{\eta}^h : \boldsymbol{\sigma}'' - \alpha S^w p^h \nabla_{\mathbf{x}} \cdot \boldsymbol{\eta}^h) d\Omega \\ & - \int_{\Gamma_t} \boldsymbol{\eta}^h \cdot \bar{\mathbf{t}} d\Gamma - \int_{\Omega} \boldsymbol{\eta}^h \cdot \rho \mathbf{g} d\Omega = 0 \end{aligned} \quad (6.33)$$

$$\begin{aligned} L_2(\psi^h; \mathbf{u}^h, p^h) \equiv & \int_{\Omega} \alpha \psi^h \nabla_{\mathbf{x}} \cdot \dot{\mathbf{u}}^h d\Omega + \int_{\Omega} \psi^h \mathcal{Q}^{-1} \dot{p}^h d\Omega + \int_{\Omega} \nabla_{\mathbf{x}} \psi^h \cdot \mathbf{k}^w \cdot \nabla_{\mathbf{x}} p^h d\Omega \\ & - \int_{\Gamma_q} \psi^h \mathbf{n}_{\Gamma} \cdot \bar{\mathbf{q}} d\Gamma - \int_{\Omega} \nabla_{\mathbf{x}} \psi^h \cdot \mathbf{k}^w \cdot S^w \rho^w \mathbf{g} d\Omega \\ & + \int_{\Omega} \varepsilon_f (\psi^h - \Pi \psi^h) (p^h - \Pi p^h) d\Omega = 0 \end{aligned} \quad (6.34)$$

where the reproducing kernel approximations to the trial functions for both solid displacement and water pressure fields are as follows

$$\mathbf{u}^h = \sum_{I=1}^{NP} N_I \mathbf{U}_I, \quad p^h = \sum_{I=1}^{NP} N_I P_I \quad (6.35)$$

and the corresponding test functions are

$$\boldsymbol{\eta}^h = \sum_{I=1}^{NP} N_I \boldsymbol{\eta}_I^u, \quad \psi^h = \sum_{I=1}^{NP} N_I \psi_I^p \quad (6.36)$$

in which N_I is the reproducing kernel shape function defined in (6.23), and \mathbf{U}_I , P_I , $\boldsymbol{\eta}_I^u$ and

ψ_l^p are the corresponding nodal coefficients. It is noteworthy to mention that an equal-order approximation for both solid displacement and fluid pressure fields is adopted, and thus significant computational cost is saved compared to mixed order approximations. However, for low permeable materials or nearly undrained conditions, the equal-order approximation pair may lead to unstable solutions of the coupled system of equations due to violation of the inf-sup condition. To achieve a stable formulation with the equal order approximation, a fluid pressure projection-based stabilization (the last domain integral term in equation (6.34)) is added to the variational formulation.

6.2.3 Temporal discretization

If the problem is to be solved between an initial time t_0 and a final time t_f , a partition of the time interval is considered, resulting in a series of time increments $\Delta t_{n+1} = t_{n+1} - t_n$. In this study, the Newmark scheme is applied to the solid motion fields:

$$\ddot{\mathbf{u}}_{n+1}^h = \ddot{\mathbf{u}}_n^h + \Delta \ddot{\mathbf{u}}_{n+1}^h \quad (6.37)$$

$$\dot{\mathbf{u}}_{n+1}^h = \dot{\mathbf{u}}_n^h + \ddot{\mathbf{u}}_n^h \Delta t_{n+1} + \beta_1 \Delta \ddot{\mathbf{u}}_{n+1}^h \Delta t_{n+1} \quad (6.38)$$

$$\mathbf{u}_{n+1}^h = \mathbf{u}_n^h + \dot{\mathbf{u}}_n^h \Delta t_{n+1} + \frac{1}{2} \ddot{\mathbf{u}}_n^h \Delta t_{n+1}^2 + \frac{1}{2} \beta_2 \Delta \ddot{\mathbf{u}}_{n+1}^h \Delta t_{n+1}^2 \quad (6.39)$$

and the generalized trapezoidal rule is applied to the water pressure field:

$$\dot{p}_{n+1}^h = \dot{p}_n^h + \Delta \dot{p}_{n+1}^h \quad (6.40)$$

$$p_{n+1}^h = p_n^h + \dot{p}_n^h \Delta t_{n+1} + \theta \Delta \dot{p}_{n+1}^h \Delta t_{n+1} \quad (6.41)$$

Evaluating the semi-discrete equations (6.33) and (6.34) at time t_{n+1} , and setting the time integration parameters as $\beta_1 = 1/2$, $\beta_2 = 0$, $\theta = 0$, the following fully discrete equations are yielded:

$$\mathbf{M}_{n+1}^u \ddot{\mathbf{U}}_{n+1} = \mathbf{F}_{n+1}^{ue} - \mathbf{F}_{n+1}^u \quad (6.42)$$

$$\mathbf{M}_{n+1}^p \dot{\mathbf{P}}_{n+1} = \mathbf{F}_{n+1}^{pe} - \mathbf{F}_{n+1}^p \quad (6.43)$$

where

$$\mathbf{M}_{IJ}^u = \int_{\Omega} N_I \rho N_J \mathbf{I} d\Omega \quad (6.44)$$

$$\mathbf{F}_I^{ue} = \int_{\Omega} N_I \rho \mathbf{g} d\Omega + \int_{\Gamma_t} N_I \bar{\mathbf{t}} d\Gamma \quad (6.45)$$

$$\mathbf{F}_I^u = \int_{\Omega} \mathbf{B}_I^{uT} \cdot \boldsymbol{\tau}'' d\Omega - \int_{\Omega} \mathbf{B}_I^{uT} \cdot (\alpha S^w p^h \mathbf{m}) d\Omega \quad (6.46)$$

$$M_{IJ}^p = \int_{\Omega} N_I Q^{-1} N_J d\Omega \quad (6.47)$$

$$F_I^{pe} = \int_{\Omega} \mathbf{B}_I^{pT} \cdot \mathbf{k}^w \cdot (S^w \rho^w \mathbf{g}) d\Omega - \int_{\Gamma_q} N_I \mathbf{n}_{\Gamma} \cdot \bar{\mathbf{q}} d\Gamma \quad (6.48)$$

$$F_I^p = \int_{\Omega} N_I \alpha \nabla_{\mathbf{x}} \cdot \dot{\mathbf{u}}^h d\Omega + \int_{\Omega} \mathbf{B}_I^{pT} \cdot \mathbf{k}^w \cdot \nabla_{\mathbf{x}} p^h d\Omega + \int_{\Omega} \varepsilon_f (N_I - \Pi N_I) (p^h - \Pi p^h) d\Omega \quad (6.49)$$

For simplicity, the subscript $n+1$ denoting the time step has been omitted in equations

(6.44-6.49) and the remainder of this chapter. In these equations, the index variables $I, J = 1, \dots, NP$, and NP is the total number of nodes, $\boldsymbol{\tau}''$ is the effective Cauchy stress vector corresponding to the stress tensor $\boldsymbol{\sigma}''$, $\mathbf{m} = [1 \ 1 \ 1 \ 0 \ 0 \ 0]^T$, \mathbf{I} is the second order identity matrix, \mathbf{B}_I'' and \mathbf{B}_I^p are the shape function gradient matrices associated with the solid displacement and water pressure field of node I .

6.3 Naturally Stabilized Nodal Integration

As mentioned previously, the simplest domain integration scheme is the direct nodal integration (DNI), from which the internal force vectors \mathbf{F}_I'' in (6.46) and F_I^p in equation (6.49) can be evaluated as

$$\mathbf{F}_I'' \cong \sum_{L=1}^{NP} V_L \left[\mathbf{B}_I^{uT} \cdot \boldsymbol{\tau}'' - \alpha S^w p^h \mathbf{B}_I^{uT} \cdot \mathbf{m} \right] \Big|_{\mathbf{x}_L} \quad (6.50)$$

$$F_I^p \cong \sum_{L=1}^{NP} V_L \left[N_I \alpha \nabla_{\mathbf{x}} \cdot \dot{\mathbf{u}}^h + \mathbf{B}_I^{pT} \cdot \mathbf{k}^w \cdot \nabla_{\mathbf{x}} p^h + \varepsilon_f (N_I - \Pi N_I) (p^h - \Pi p^h) \right] \Big|_{\mathbf{x}_L} \quad (6.51)$$

Although the DNI quadrature scheme appears to be attractive due to its simplicity, it can cause severe numerical instabilities and non-convergent solutions. To eliminate the spurious low energy modes of nodal integration, an assumed gradient matrix $\hat{\mathbf{B}}_I''$ is introduced in [Hillman & Chen (2016)] based on the first order Taylor expansion of \mathbf{B}_I'' as

$$\hat{\mathbf{B}}_I'' \Big|_{\mathbf{x}} = \mathbf{B}_I'' \Big|_{\mathbf{x}_L} + (\mathbf{x} - \mathbf{x}_L) \cdot (\nabla_{\mathbf{x}} \otimes \mathbf{B}_I'') \Big|_{\mathbf{x}_L} \quad (6.52)$$

where the subscripts \mathbf{x} and \mathbf{x}_L represent the location of the evaluation points. Similarly, an assumed stress $\hat{\boldsymbol{\tau}}''$ based on an expansion of the effective Cauchy stress vector $\boldsymbol{\tau}''$ is also introduced:

$$\hat{\boldsymbol{\tau}}''|_{\mathbf{x}} = \boldsymbol{\tau}''|_{\mathbf{x}_L} + (\mathbf{x} - \mathbf{x}_L) \cdot (\nabla_{\mathbf{x}} \otimes \boldsymbol{\tau}'')|_{\mathbf{x}_L} \quad (6.53)$$

Replacing \mathbf{B}_I'' and $\boldsymbol{\tau}''$ in equation (6.50) with $\hat{\mathbf{B}}_I''$ and $\hat{\boldsymbol{\tau}}''$, respectively, and performing the nodal integration, the following naturally stabilized nodal quadrature version of the internal force vector \mathbf{F}_I'' is obtained

$$\begin{aligned} \mathbf{F}_I'' \cong & \sum_{L=1}^{NP} V_L \left[\mathbf{B}_I^{uT} \cdot \boldsymbol{\tau}'' - \alpha p^h \mathbf{B}_I^{uT} \cdot \mathbf{m} \right] |_{\mathbf{x}_L} \\ & + \sum_{L=1}^{NP} \left[m_{Lx} \mathbf{B}_{I,x}^{uT} : \boldsymbol{\tau}''_{,x} + m_{Ly} \mathbf{B}_{I,y}^{uT} : \boldsymbol{\tau}''_{,y} + m_{Lz} \mathbf{B}_{I,z}^{uT} : \boldsymbol{\tau}''_{,z} \right] |_{\mathbf{x}_L} \end{aligned} \quad (6.54)$$

where

$$m_{Lx} = \int_{\Omega_L} (x - x_L)^2 d\Omega \quad (6.55)$$

$$m_{Ly} = \int_{\Omega_L} (y - y_L)^2 d\Omega \quad (6.56)$$

$$m_{Lz} = \int_{\Omega_L} (z - z_L)^2 d\Omega \quad (6.57)$$

Note that, in arriving at equation (6.54), the following assumption has been adopted

$$\int_{\Omega_L} (x - x_L) d\Omega = \int_{\Omega_L} (y - y_L) d\Omega = \int_{\Omega_L} (z - z_L) d\Omega = 0 \quad (6.58)$$

which are generally satisfied when the node L is located at or near the centroid of the quadrature zone Ω_L . Following a similar procedure, an assumed gradient matrix $\hat{\mathbf{B}}_I^p$ associated with water pressure field can be expressed as

$$\hat{\mathbf{B}}_I^p \Big|_{\mathbf{x}} = \mathbf{B}_I^p \Big|_{\mathbf{x}_L} + (\mathbf{x} - \mathbf{x}_L) \cdot (\nabla_{\mathbf{x}} \otimes \mathbf{B}_I^p) \Big|_{\mathbf{x}_L} \quad (6.59)$$

In addition, an assumed water pressure gradient of the following form is introduced

$$\hat{\nabla}_{\mathbf{x}} p^h \Big|_{\mathbf{x}} = \nabla_{\mathbf{x}} p^h \Big|_{\mathbf{x}_L} + (\mathbf{x} - \mathbf{x}_L) \cdot (\nabla_{\mathbf{x}} \otimes \nabla_{\mathbf{x}} p^h) \Big|_{\mathbf{x}_L} \quad (6.60)$$

Taking equations (6.51, 6.55-6.58) into consideration, and replacing the gradient matrix \mathbf{B}_I^p and the fluid pressure gradient $\nabla_{\mathbf{x}} p$ in (6.51) with the corresponding expanded version defined in (6.59-6.60), we obtain the following internal force F_I^p based on the naturally stabilized nodal integration scheme:

$$\begin{aligned} F_I^p \cong & \sum_{L=1}^{NP} w_L \left[N_I \alpha \nabla_{\mathbf{x}} \cdot \dot{\mathbf{u}}^h + \mathbf{B}_I^{pT} \cdot \mathbf{k}^w \cdot \nabla_{\mathbf{x}} p^h + \varepsilon_f (N_I - \Pi N_I) (p^h - \Pi p^h) \right] \Big|_{\mathbf{x}_L} \\ & + \sum_{L=1}^{NP} \left[m_{Lx} \mathbf{B}_{I,x}^{pT} \cdot \mathbf{k}^w \cdot (\nabla_{\mathbf{x}} p^h)_{,x} + m_{Ly} \mathbf{B}_{I,y}^{pT} \cdot \mathbf{k}^w \cdot (\nabla_{\mathbf{x}} p^h)_{,y} + m_{Lz} \mathbf{B}_{I,z}^{pT} \cdot \mathbf{k}^w \cdot (\nabla_{\mathbf{x}} p^h)_{,z} \right] \Big|_{\mathbf{x}_L} \end{aligned} \quad (6.61)$$

As studied in [Chen et al. (2001); Chen, Hillman, & Rüter M (2013)], linear exactness in the Galerkin approximation requires: (1) first-order completeness of the trial and test functions; and (2) a quadrature scheme that satisfies integration constraints. The former completeness

requirement is obviously met by the employed RK shape functions by construction, whereas the later integration constraints are often violated by traditional quadrature schemes for meshfree methods, including Gauss integration and DNI. Although NSNI introduced in the previous section eliminates the low energy modes of under-integration schemes, its discrete version based on direct derivatives of shape functions as presented in equations (6.54) and (6.61) still does not satisfy the integration constraints, and thus additional treatments are needed to recover the integration accuracy. To this end, let us first examine the integration constraints for the mixed reproducing kernel formulation. For linear Galerkin exactness, the pressure projection stabilization term in (6.34) is not considered here since we want to examine the problem with a linear fluid pressure solution. Furthermore, we neglect the terms involving body forces and time derivatives in equations (6.33-6.34) and employ the expanded gradients and fluxes defined previously, and thus the following naturally stabilized steady state variational equations are yielded

$$\hat{L}_1(\boldsymbol{\eta}^h; \mathbf{u}^h, p^h) \equiv \int_{\Omega} \hat{\nabla}_{\mathbf{x}}^S \otimes \boldsymbol{\eta}^h : \hat{\boldsymbol{\sigma}} d\Omega - \int_{\Gamma_t} \boldsymbol{\eta}^h \cdot \bar{\mathbf{t}} d\Gamma = 0 \quad (6.62)$$

$$\hat{L}_2(\psi^h; \mathbf{u}^h, p^h) \equiv \int_{\Omega} \hat{\nabla}_{\mathbf{x}}^S \psi^h \cdot \hat{\mathbf{q}} d\Omega + \int_{\Gamma_q} \psi^h \mathbf{n}_{\Gamma} \cdot \bar{\mathbf{q}} d\Gamma = 0 \quad (6.63)$$

where $\hat{\boldsymbol{\sigma}} = \hat{\boldsymbol{\sigma}}'' - \alpha S^w p^h \hat{\boldsymbol{\delta}}$ and $\hat{\mathbf{q}} = -\mathbf{k}^w \cdot \hat{\nabla}_{\mathbf{x}}^S p^h$ represent the naturally stabilized total Cauchy stress tensor and fluid flux vector, respectively, and the symbol of superposed hat denotes the first order expanded gradient stabilization. For problems with linear solutions, the associated nodal coefficients of trial functions for solid displacement and fluid pressure can be expressed as follows

$$U_{ii} = c_{i0}^u + \sum_{k=1}^3 c_{ik}^u x_{ik} \quad (6.64)$$

$$P_I = c_0^p + \sum_{k=1}^3 c_k^p x_{ik} \quad (6.65)$$

where x_{ik} denotes the k^{th} component of the coordinates of node I , c_{ik}^u and c_k^p denote constant coefficients for solid displacement and water pressure fields, respectively. Corresponding to the above linear solutions, the fluid flux becomes a constant field and the gradient expansion-based stabilization terms vanish in equation (6.63). As a result, the 1st order integration constraints on the test function of fluid pressure field have the following form:

$$\langle \nabla_{\mathbf{x}} N_I \rangle_{\Omega} = \langle N_I \mathbf{n}_{\Gamma} \rangle_{\Gamma} \quad (6.66)$$

where $\langle \cdot \rangle_{\Omega}$ and $\langle \cdot \rangle_{\Gamma}$ denote the quadrature version of domain integral and boundary integral for the functions inside the angle brackets, respectively. Similarly, the integration constraints on the test function of the solid displacement field can be obtained from equation (6.62) as

$$\langle \nabla_{\mathbf{x}} \cdot (N_I \boldsymbol{\sigma}) \rangle_{\Omega} = \langle \mathbf{n}_{\Gamma} \cdot (N_I \boldsymbol{\sigma}) \rangle_{\Gamma} \quad (6.67)$$

where $\boldsymbol{\sigma} = \boldsymbol{\sigma}'' - \alpha p^h \boldsymbol{\delta}$ represents the total stress. If the water pressure p^h is considered to be a linear function, the total stress $\boldsymbol{\sigma}$ also becomes linear, resulting in high-order integration constraints. Satisfaction of the high-order integration constraints requires solving three 4×4 algebraic equations at every nodal point [Chen, Hillman, Rüter (2013)], which would be quite expensive in the semi-Lagrangian formulation since the shape functions are frequently

re-constructed during the simulation. To save computational time, a relaxed integration constraint is considered in the present study, where a constant total stress field $\boldsymbol{\sigma}$ is assumed, and thus integration constraints of the same form as (6.66) are yielded. Integration constraints of the form (6.66) are satisfied straightforwardly by the stabilized conforming nodal integration (SCNI) [Chen et al. (2001); Chen, Yoon, & Wu (2002)] through the construction of smoothed shape function gradients as follows:

$$\tilde{\nabla}_{\mathbf{x}} N_I(\mathbf{x}_L) = \frac{1}{V_L} \int_{\Omega_L} \nabla_{\mathbf{x}} N_I(\mathbf{x}) \, d\Omega = \frac{1}{V_L} \int_{\Gamma_L} N_I(\mathbf{x}) \mathbf{n} \, d\Gamma \quad (6.68)$$

in which $\tilde{\nabla}_{\mathbf{x}}$ is the smoothed gradient operator, Ω_L denotes the nodal representative domain constructed by Voronoi diagram, as illustrated in Figure 6.3(a).

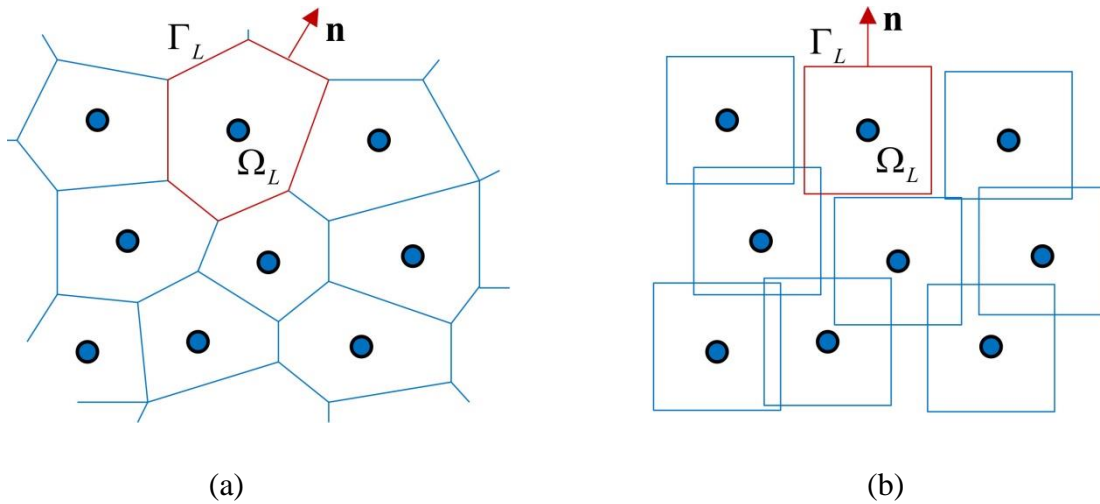


Figure 6.3 (a) Conforming nodal smoothing cells in SCNI and (b) non-conforming nodal smoothing cells in SNNI.

For problems involving extremely large deformation, however, it is ineffective to employ SCNI under the semi-Lagrangian framework as frequent re-construction of conforming subdomains in the current configuration is quite tedious. In this situation, the stabilized

non-conforming nodal integration (SNNI), as a simplified version of SCNI, is a viable approach for smoothing the gradients within non-conforming integration cells (shown in Figure 6.3(b)). As a consequence, the integration constraint (6.66) is often violated and further integration correction is needed. To this end, a modified shape function gradient of the test function ψ^h is defined, following [Chen, Hillman, & Rüter (2013)]:

$$\nabla_{\mathbf{x}}^c N_I = \nabla_{\mathbf{x}} N_I + R_I^c \zeta_I^c \quad (6.69)$$

where

$$R_I^c(\mathbf{x}) = \begin{cases} 1 & \text{if } \mathbf{x} \in \text{supp}(N_I^p) \\ 0 & \text{if } \mathbf{x} \notin \text{supp}(N_I^p) \end{cases} \quad (6.70)$$

By substitution of (6.69) into the integration constraint (6.66), the constant coefficient ζ_I^c can be obtained as

$$\zeta_{Ij}^c = \frac{\langle N_I \mathbf{n}_{\Gamma_j} \rangle_{\Gamma} - \langle N_{I,j} \rangle_{\Omega}}{\langle R_I^c \rangle_{\Omega}}, \quad j = x, y, z \quad (6.71)$$

With the corrected test function gradients in (6.69), the following modified stabilized shape function gradient matrices for test functions are yielded

$$\left(\hat{\mathbf{B}}_I^u \right)_x^c = \left(\tilde{\mathbf{B}}_I^u \right)_{x_L}^c + (\mathbf{x} - \mathbf{x}_L) \cdot \left(\nabla_{\mathbf{x}}^{\nabla} \otimes \tilde{\mathbf{B}}_I^u \right)_{x_L} \quad (6.72)$$

$$\left(\hat{\mathbf{B}}_I^p \right)_x^c = \left(\tilde{\mathbf{B}}_I^p \right)_{x_L}^c + (\mathbf{x} - \mathbf{x}_L) \cdot \left(\nabla_{\mathbf{x}}^{\nabla} \otimes \tilde{\mathbf{B}}_I^p \right)_{x_L} \quad (6.73)$$

along with the corresponding stabilized shape function gradient matrices for the trial functions

$$\hat{\mathbf{B}}_I^u|_{\mathbf{x}} = \tilde{\mathbf{B}}_I^u|_{\mathbf{x}_L} + (\mathbf{x} - \mathbf{x}_L) \cdot (\nabla_{\mathbf{x}}^{\nabla} \otimes \tilde{\mathbf{B}}_I^u)|_{\mathbf{x}_L} \quad (6.74)$$

$$\hat{\mathbf{B}}_I^p|_{\mathbf{x}} = \tilde{\mathbf{B}}_I^p|_{\mathbf{x}_L} + (\mathbf{x} - \mathbf{x}_L) \cdot (\nabla_{\mathbf{x}}^{\nabla} \otimes \tilde{\mathbf{B}}_I^p)|_{\mathbf{x}_L} \quad (6.75)$$

In (6.72-6.75), $\nabla_{\mathbf{x}}^{\nabla}$ denotes the implicit reproducing kernel gradient operator defined in (6.29), which is adopted here to accelerate the computational speed as discussed in Section 6.2.1.

Accordingly, the stabilized Cauchy stress and water pressure gradient can be expressed as

$$\hat{\boldsymbol{\tau}}^n|_{\mathbf{x}} = \tilde{\boldsymbol{\tau}}^n|_{\mathbf{x}_L} + (\mathbf{x} - \mathbf{x}_L) \cdot (\nabla_{\mathbf{x}}^{\nabla} \otimes \tilde{\boldsymbol{\tau}}^n)|_{\mathbf{x}_L} \quad (6.76)$$

$$\hat{\nabla}_{\mathbf{x}} p^h|_{\mathbf{x}} = \tilde{\nabla}_{\mathbf{x}} p^h|_{\mathbf{x}_L} + (\mathbf{x} - \mathbf{x}_L) \cdot (\nabla_{\mathbf{x}}^{\nabla} \otimes \tilde{\nabla}_{\mathbf{x}} p^h)|_{\mathbf{x}_L} \quad (6.77)$$

Consequently, the final nodally integrated discrete form of the internal forces are obtained as follows

$$\begin{aligned} \mathbf{F}_I^u &\cong \sum_{L=1}^{NP} V_L \left[(\tilde{\mathbf{B}}_I^u)^c \cdot \tilde{\boldsymbol{\tau}}^n - \alpha p^h (\tilde{\mathbf{B}}_I^u)^c \cdot \mathbf{m} \right] \Big|_{\mathbf{x}_L} \\ &+ \sum_{L=1}^{NP} \left[m_{Lx} \tilde{\mathbf{B}}_{I,x}^{uT} : \tilde{\boldsymbol{\tau}}^n_{,x} + m_{Ly} \tilde{\mathbf{B}}_{I,y}^{uT} : \tilde{\boldsymbol{\tau}}^n_{,y} + m_{Lz} \tilde{\mathbf{B}}_{I,z}^{uT} : \tilde{\boldsymbol{\tau}}^n_{,z} \right] \Big|_{\mathbf{x}_L} \end{aligned} \quad (6.78)$$

$$\begin{aligned} F_I^p &\cong \sum_{L=1}^{NP} w_L \left[N_I \alpha \tilde{\nabla}_{\mathbf{x}} \cdot \dot{\mathbf{u}}^h + (\tilde{\mathbf{B}}_I^p)^c \cdot \mathbf{k}^w \cdot \nabla_{\mathbf{x}} p^h + \varepsilon_f (N_I - \Pi N_I) (p^h - \Pi p^h) \right] \Big|_{\mathbf{x}_L} \\ &+ \sum_{L=1}^{NP} \left[m_{Lx} \tilde{\mathbf{B}}_{I,x}^p \cdot \mathbf{k}^w \cdot (\tilde{\nabla}_{\mathbf{x}} p^h)_{,x} + m_{Ly} \tilde{\mathbf{B}}_{I,y}^p \cdot \mathbf{k}^w \cdot (\tilde{\nabla}_{\mathbf{x}} p^h)_{,y} + m_{Lz} \tilde{\mathbf{B}}_{I,z}^p \cdot \mathbf{k}^w \cdot (\tilde{\nabla}_{\mathbf{x}} p^h)_{,z} \right] \Big|_{\mathbf{x}_L} \end{aligned} \quad (6.79)$$

6.4 Numerical Examples

6.4.1 Wave propagation in poroelastic media

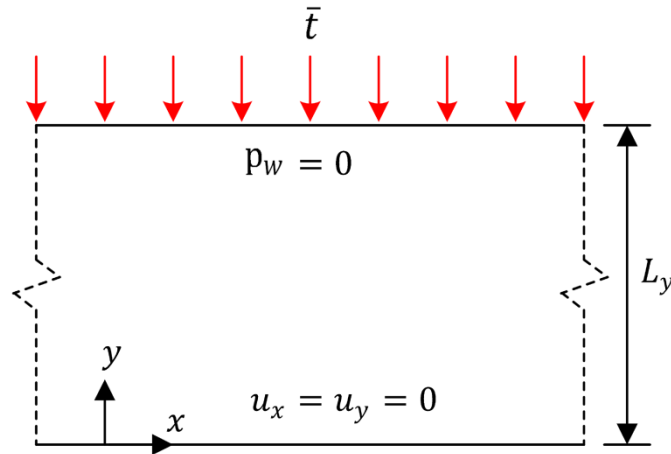


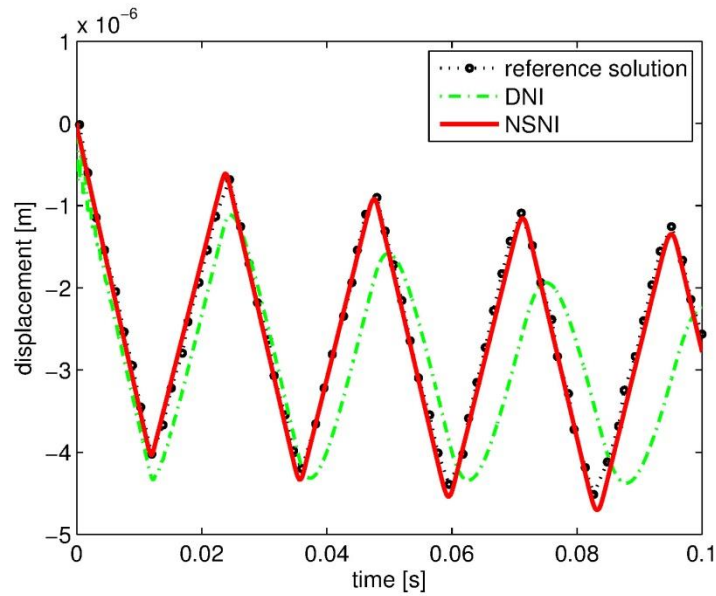
Figure 6.4 Illustration of the problem set-up of wave propagation in poroelastic media

The problem of wave propagation in fluid saturated porous media is analyzed to verify the proposed meshfree formulation. As depicted in Figure 6.4, a soil layer of height $L_y = 10\text{m}$ is considered to be infinite long in the horizontal x -direction. The top surface of the porous media is considered drained and subjected to a uniform step loading with magnitude $\bar{t} = 3\text{kN/m}^2$. Linear elastic material behavior is assumed, and soil material data from [Soares (2014)] are adopted as follows: Young's modulus 254423076.9 N/m^2 , Poisson's ratio 0.298 , mass density of solid phase 2700 kg/m^3 , mass density of fluid phase 1000kg/m^3 , porosity 0.48 , permeability $3.55 \times 10^{-9}\text{ m}^4/\text{Ns}$, bulk modulus of solid grains $1.1 \times 10^{10}\text{ N/m}^2$, and bulk modulus of fluid phase $3.3 \times 10^9\text{ N/m}^2$.

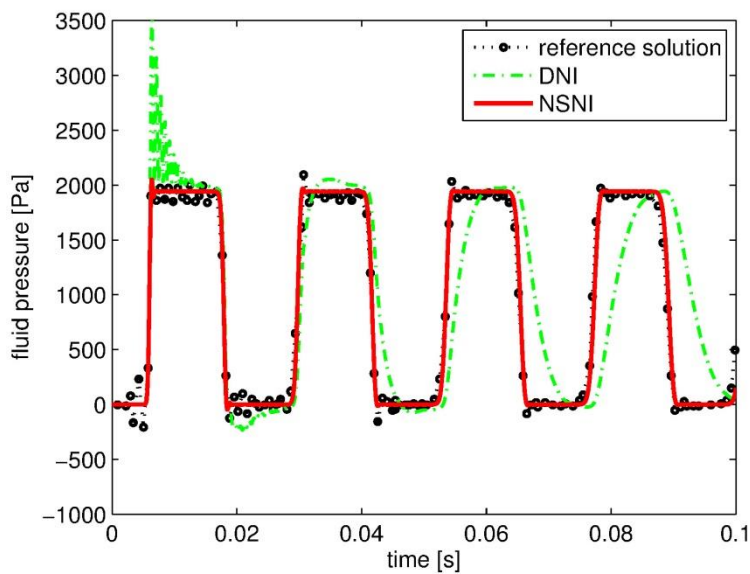
Figure 6.5 depicts the time-histories of solid displacement at the top of the column and

fluid pressure at the bottom of the column obtained from DNI- and NSNI-based RKPM formulations, respectively, as well as the reference solutions from [Soares (2014)]. The FEM results presented in [Soares (2014)] have been shown to agree well with the semi-analytical solutions of [Schanz & Cheng (2000); Schanz (2009)], except that different over-shoots and fluctuations at wave fronts are generated by the numerical Laplace inversion of latter solutions. Hence, only the FEM results of [Soares (2014)] are plotted here as the reference solutions. As shown in Figure 6.5, NSNI-based RKPM captures the dynamic response of saturated porous materials in a satisfactory manner, while DNI-based RKPM results in significant errors in the both solid displacement and fluid pressure fields, including a severe fluctuation of fluid pressure at the early time steps of the simulation.

Figure 6.6 shows the convergence behavior of NSNI-RKPM with different model refinement levels. It is clearly shown that converged solutions in both solid and fluid fields can be obtained upon refinement of the nodal discretization. In addition, the overshoot behavior at fluid pressure wave fronts is greatly alleviated in the refined model.

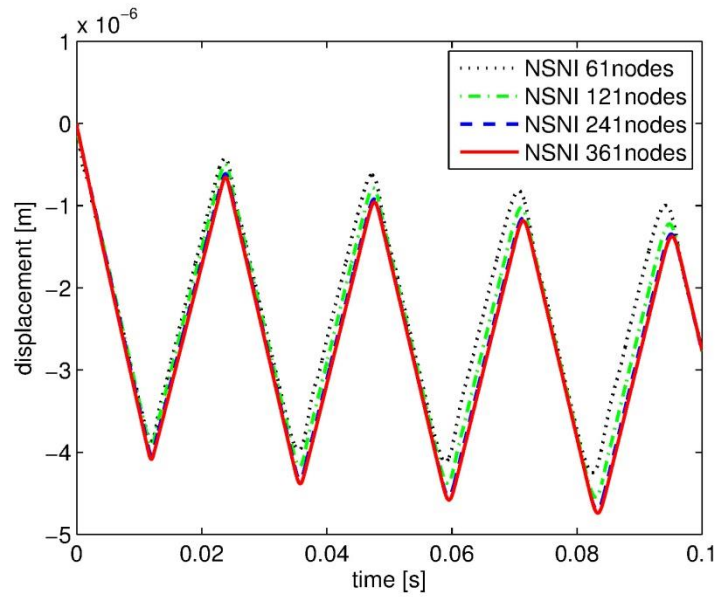


(a)

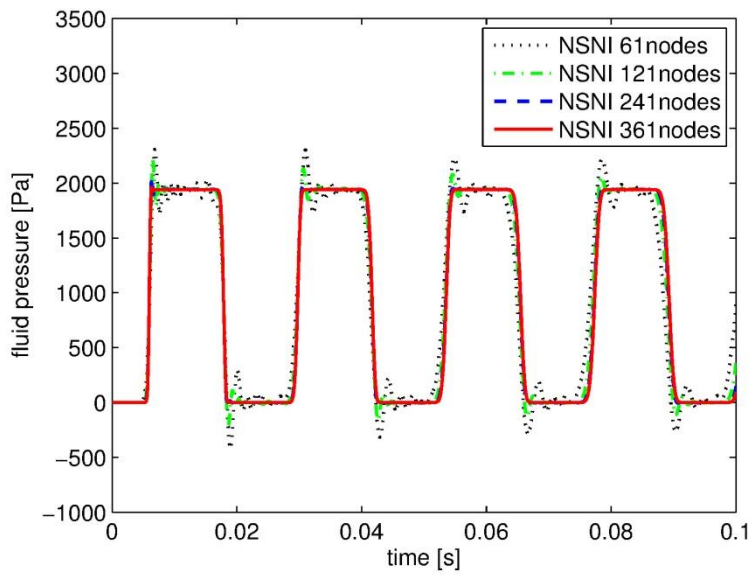


(b)

Figure 6.5 Time history of (a) the solid displacement at the top and (b) the fluid pressure at the bottom of the soil layer obtained from DNI- and NSNI-based RKPM formulations using 241 nodes along the vertical y -direction, compared with the reference solution from [Soares 2014].



(a)



(b)

Figure 6.6 Time history of (a) the solid displacement at the top and (b) the fluid pressure at the bottom of the soil column obtained from NSNI-based RKPM formulation with different nodal discretization refinement.

6.4.2 Liakopoulos' drainage experiment

The drainage experiment conducted by Liakopoulos [Liakopoulos (1965)] has been considered in many studies [Zienkiewicz et al. (1990); Khoei & Mohammadnejad (2011); Bandara et al. (2016)] as a benchmark problem to validate numerical models for unsaturated deformable porous media. In the experiment, a vertical column packed uniformly with very fine sand is instrumented to measure the water pressure along the height of the column. As shown in the schematic diagram of Figure 6.7, the column is initially saturated with a zero water pressure gradient along its height due to the uniform water flow condition. This steady water flow state is perturbed by suddenly ceasing the water supply at the top surface, and then the water pressure has to be redistributed due to the gravity induced flow, accompanied with the sand settlement.

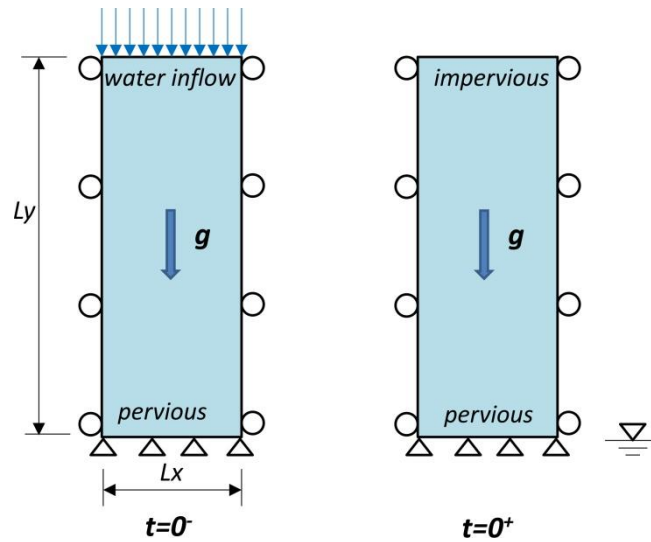


Figure 6.7 Illustration of the set-up for Liakopoulos' drainage experiment, where $L_x = 0.1$ m, $L_y = 1.0$ m, and g denotes the gravitational acceleration with magnitude 9.806 m/s^2 .

The adopted material properties taken from [Khoei & Mohammadnejad (2011)] are as follows: Young's modulus 1.3×10^6 Pa, Poisson's ratio 0.4, mass density of solid phase 2000

kg/m³, mass density of water phase 1000kg/m³, porosity 0.2975, intrinsic permeability 4.5×10⁻¹³ m², dynamic viscosity of water 1.0×10⁻³ Pa·s, bulk modulus of solid grains 1.0×10¹² N/m², and bulk modulus of water 2.0×10⁹ N/m². The degree of water saturation and the relative permeability are defined as follows:

$$S^w = 1 - 0.10152 \left(\frac{s}{\gamma^w} \right)^{2.4279} \quad (6.80)$$

$$k^{rw} = 1 - 2.207(1 - S^w) \quad (6.81)$$

where γ^w is the specific weight of water, $s = p^a - p^w$ is the suction, p^a and p^w are the air pressure and water pressure, respectively. For the initial condition, zero water pressure (fully saturated) and gravity induced initial effective stress are considered.

In Figure 6.8, the distribution of the water pressure along the height of the sand column at different time is plotted. Although some discrepancies between RKPM solutions and Liakopoulos' experimental data can be observed at the early time, the two results eventually approach each other at the later stage of the drainage process. The discrepancies between numerical solutions and experimental data at early time have also been reported in many other studies, e.g., [Zienkiewicz et al.(1990); Khoei & Mohammadnejad (2011); Bandara et al. (2016)], and they are mainly due to the adopted simplified material model. Here, the FEM results given in [Bandara et al. (2016)] are plotted in Figure 6.8 for comparison purpose. It can be seen that the water pressure distribution predicted by FEM and RKPM agrees quite well with each other. Moreover, time histories of the water pressure at the height of 0.625m and 0.975m are presented in Figure 6.9 The results of RKPM are quite satisfactory, compared to the FEM solution of [Li,

& Wei (2015)] and Liakopoulos' experimental data. As non-zero air pressure is considered in the FEM formulation of [Li & Wei (2015)], a slightly lower FEM prediction of the water pressure is obtained, compared to the presented RKPM formulation which assumes zero air pressure. Overall speaking, the obtained numerical solutions are satisfactory, and thus the effectiveness of RKPM for modeling unsaturated porous media is demonstrated.

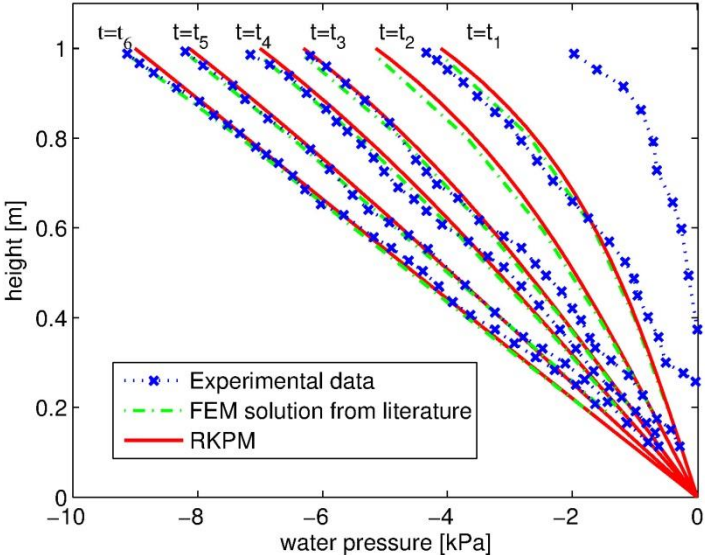


Figure 6.8 Distribution of the water pressure along the height of the sand column at different time ($t_1 = 5 \text{ min}$, $t_2 = 10 \text{ min}$, $t_3 = 20 \text{ min}$, $t_4 = 30 \text{ min}$, $t_5 = 60 \text{ min}$, $t_6 = 120 \text{ min}$), obtained from Liakopoulos' experiment, FEM [Bandara et al. (2016)], and RKPM.

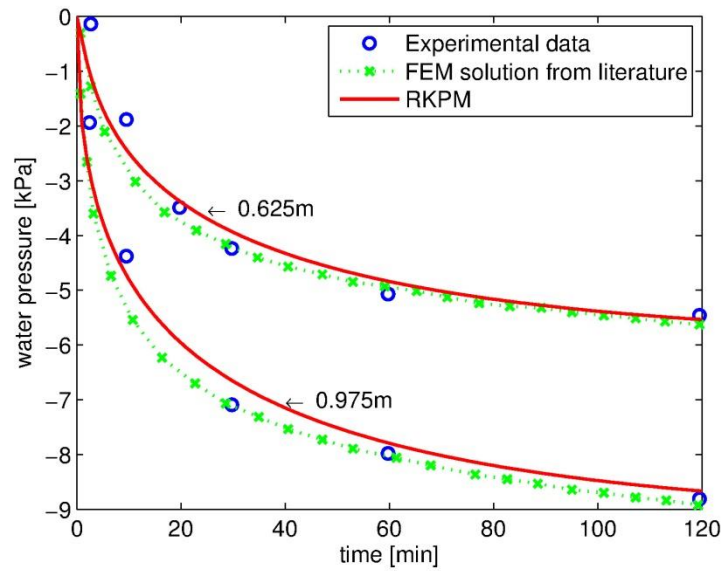


Figure 6.9 Time histories of the water pressure at the height of 0.625m and 0.975m obtained from Liakopoulos' experiment, FEM [Li & Wei (2015)], and RKPM.

6.4.3 Seepage-induced levee failure

In this example, the proposed RKPM formulation is applied for modeling a levee failure process following the experiment described in [Iseno et al. (2004); Mori (2008)]. As depicted in Figure 6.10, a seepage flow into an initially unsaturated sand levee is generated by continuously imposing a steady water pressure at the levee's back surface, so that the raised water level in the levee can induce seepage failure. In the experiment, the levee remained stable for about 13 hours during the seepage flow process. Subsequently, the material damage initiated at the levee's toe led to a progressive failure, which lasted for about 30 seconds until the complete levee failure occurs.

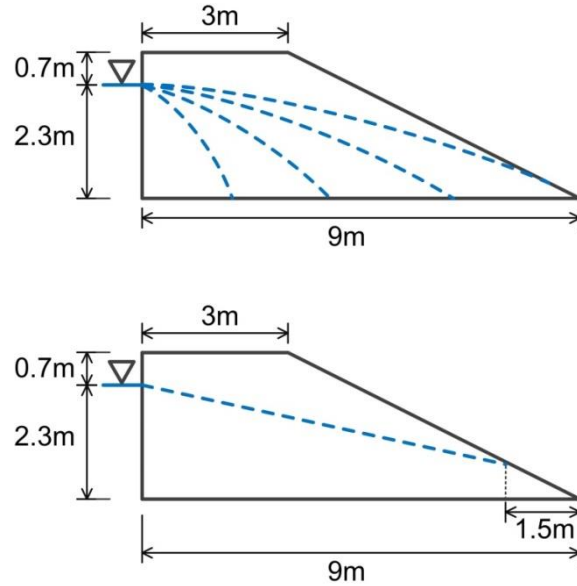


Figure 6.10 Sketch of the levee problem: (a) illustration of the water level at different seepage stages; (b) the initial state chosen for the nonlinear dynamic simulation, where the dotted blue lines represent the water levels.

Due to the lack of well documented material data for the loose sandy soil used in this experiment, material properties chosen from other literature [Khoei & Mohammadnejad (2011); Soga et al. (2015); Bandara & Soga (2015)] are adopted in the present study. This is sufficient for the purpose of demonstrating RKPM's capabilities for landslide modeling, although advanced constitutive models with calibrated material data would be essential if one intends to reproduce the soil behaviors more accurately. The adopted data are as follows: Young's modulus 1.0×10^7 Pa, Poisson's ratio 0.3, gravitational acceleration 9.806 m/s^2 , mass density of solid phase 2700 kg/m^3 , mass density of water phase 1000 kg/m^3 , porosity 0.46, permeability $5.0 \times 10^{-4} \text{ m}^2$, bulk modulus of solid grains $1.0 \times 10^{22} \text{ N/m}^2$, and bulk modulus of water $1.0 \times 10^9 \text{ N/m}^2$. The effective stress-strain relation is modeled by the Drucker-Prager plasticity model with a friction angle of 20° and cohesion of $3.0 \times 10^2 \text{ Pa}$. In addition, the van Genuchten model is employed to describe the hydraulic properties:

$$S^w = S^{rw} + (1 - S^{rw}) \left[1 + \left(\frac{\beta p^w}{\gamma^w} \right)^n \right]^{-m} \quad (6.82)$$

$$k^{rw} = S_e^{1/2} \left[1 - (1 - S_e^{1/m})^m \right]^2 \quad (6.83)$$

in which S^w is degree of water saturation, k^{rw} is the relative permeability, $S_e = (S^w - S^{rw}) / (1 - S^{rw})$ is the effective water saturation, $S^{rw} = 0.0842$ denotes the irreducible water saturation, and the empirical parameters are chosen as $n = 2$, $m = 1 - 1/n$, $\beta = 0.7 \text{ m}^{-1}$.

As the focus here is on the post-failure analysis, the initial condition for the dynamic simulation is chosen to be the critical seepage flow state when material failure is about to occur, i.e., after 13 hours in the experiment. To this end, a steady state calculation is first performed with the imposition of the water level depicted in Figure 6.10(b) as an additional constraint, following the procedure described in [Zienkiewicz et al. (1999)]. The pore water pressure and effective stress in an equilibrium state obtained from this static analysis step are then used as the initial value in the subsequent nonlinear dynamic simulation.

The simulation results of water pressure and equivalent plastic strain distribution during the progressive failure process are shown in Figure 6.11. It can be seen that the main shear bands initiate near the toe and then propagate towards the upper surface of the levee, accompanied by a few branches. The final collapsed shape of the levee looks similar to that of the experiment. It is noteworthy to mention that, for this levee failure problem, more advanced soil constitutive models with calibrated material property data are required to further enhance the accuracy of the numerical prediction. Nevertheless, it still can be clearly seen from these simulation results that

RKPM is capable of modeling the nonlinear hydro-mechanically coupled failure mechanisms, including complicated shear band patterns and extremely large formation processes, which pose significant challenges for traditional mesh-based numerical methods.

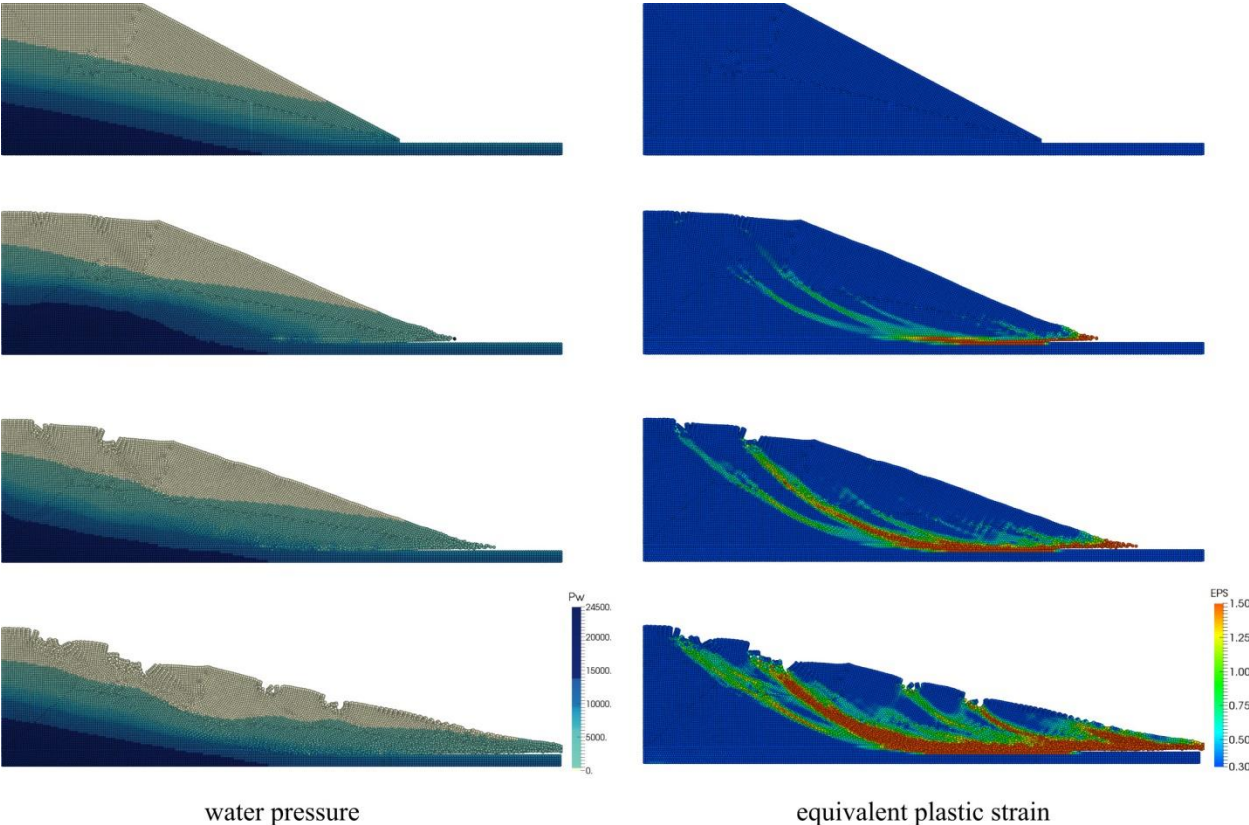


Figure 6.11 The RKPM simulation results of (left) water pressure and (right) equivalent plastic strain distribution in the levee during the progressive failure process.

Chapter 7

Conclusions and Future Work

In this chapter, conclusions of the present work are given in Section 7.1, followed by recommendations for future research in Section 7.2.

7.1 Conclusions

A stable and efficient meshfree method is proposed to solve the fully coupled hydro-mechanical problems. It has been shown that the fluid pressure projection method can be naturally integrated within the stabilized conforming nodal integration framework, and thus the non-physical fluid pressure oscillation due to violation of the inf-sup condition as well as the spurious low-energy modes due to nodal integration can both be eliminated in a cost effective way. Several benchmark problems have been analyzed and the results demonstrate the excellent performance of the stabilized meshfree formulation.

Under the semi-Lagrangian framework, the developed reproducing kernel mixed formulation is extended for nonlinear modeling of partially saturated porous media with application to landslide simulation. The naturally stabilized nodal integration has been employed to achieve accelerated, stable and convergent solution. The developed method has been verified and validated against benchmark problems, and the post-failure process of a partially saturated levee is modelled to demonstrate the method's capability in handling hydro-mechanically

coupled extremely large deformation.

In addition, a smeared crack approach for fracture modeling under nodally integrated reproducing kernel discretization has been presented. The smeared strain in a nodal representative domain is defined as the boundary integral of displacements to avoid the ambiguity of taking direct derivatives of non-smooth displacements in the cracking region. With this definition of smeared strain at the nodal representative domain, the stabilized conforming nodal integration previously proposed for optimal convergence in the Galerkin solution of second order PDEs with linear consistency can be naturally employed in the damage analysis under a unified framework. In the proposed method, the computation of displacement, strain, stress, and damage variables along with the regularization procedure are all performed at the nodal points. As such, this approach does not require interpolation of state and field variables between Gauss points and nodal points commonly needed in the conventional finite elements.

Under this framework, a scaling law is naturally introduced to ensure that the bulk energy dissipated over the nodal representative volume is consistent with the surface fracture energy of the crack segment. Since the present approach is free from mesh entanglement, the energy-based scaling procedure can be performed in a straightforward manner within each nodal representative domain. This is different from the conventional crack band finite element methods, where the regularization behavior can be affected by both element shapes and integration schemes.

Furthermore, the capability of the damage particle method in modelling hydraulic fracturing in saturated porous media has been demonstrated. Hydro-mechanical coupling is considered by introducing the regularized damage model to describe the effective stress in conjunction with a cracking-enhanced anisotropic permeability model. The method has been

applied to model several fluid injection-induced fracture problems, and satisfactory performance has been obtained. It is anticipated that this smeared crack modeling approach is promising for modeling more complicated hydraulic fracturing processes where numerous propagating fractures may intersect, because cumbersome treatments (e.g., constantly adding new degrees of freedom/cutting quadrature cells, or solving additional global partial differential equations, etc.) commonly needed in conventional methods have been effectively avoided in the proposed approach.

7.2 Recommendations for Future Research

The recommendations for future research are summarized as follows:

- 1) The simplicity of the damage particle method makes it suitable for capturing multiple propagating fractures. With the unique features of the reproducing kernel approximation, the method can be further extended for modeling extreme deformation problems (e.g., the impact-fragmentation process).
- 2) Further speed-up of the landslide simulation can be achieved by developing seamless blending of Lagrangian and semi-Lagrangian approximation [Pasetto, Chen, Wei (2017)] in the mixed formulation, which can greatly reduce the computational cost associated with frequent re-construction of the shape functions throughout the domain.
- 3) To better capture the hydro-mechanically coupled material failure behaviors, advanced constitutive models for geomaterials can be implemented under the developed meshfree computational framework.

References

1. Abe, K., Soga, K., & Bandara, S. (2013). Material point method for coupled hydromechanical problems. *Journal of Geotechnical and Geoenvironmental Engineering*, 140(3), 04013033.
2. Abousleiman, Y., Cheng, A. D., Cui, L., Detournay, E., & Roegiers, J. C. (1996). Mandel's problem revisited. *Geotechnique*, 46(2), 187-195.
3. Alonso, E. E., Yerro, A., & Pinyol, N. M. (2015). Recent developments of the Material Point Method for the simulation of landslides. In *IOP Conference Series: Earth and Environmental Science* (Vol. 26, No. 1, p. 012003). IOP Publishing.
4. Ambati, M., Gerasimov, T., & De Lorenzis, L. (2015). A review on phase-field models of brittle fracture and a new fast hybrid formulation. *Computational Mechanics*, vol. 55, no. 2, pp. 383-405.
5. Babuska, I. (1973). The finite element method with Lagrange multipliers. *Numer Math* 20: 179-192.
6. Bandara, S., & Soga, K. (2015). Coupling of soil deformation and pore fluid flow using material point method. *Computers and Geotechnics*, 63, 199-214.
7. Bandara, S., Ferrari, A., & Laloui, L. (2016). Modelling landslides in unsaturated slopes subjected to rainfall infiltration using material point method. *International Journal for Numerical and Analytical Methods in Geomechanics*, 40(9), 1358-1380.
8. Bažant, Z. P., & Oh, B. H. (1983). Crack band theory for fracture of concrete. *Mater Struct.*, vol. 16, pp. 155-77.
9. Bažant, Z. P., & Lin, F. B. (1988). Nonlocal smeared cracking model for concrete fracture. *Journal of Structural Engineering*, vol. 114, no. 11, pp. 2493-2510.
10. Bažant, Z. P., & Pijaudier-Cabot, G. (1988). Nonlocal continuum damage, localization instability and convergence. *ASME J Appl Mech*, vol. 55, pp. 287-293.
11. Bažant, Z. P., Salviato, M., Chau, V. T., Viswanathan, H., & Zubelewicz, A. (2014). Why fracking works. *Journal of Applied Mechanics*, 81(10), 101010.
12. Bažant, Z. P., Luo, W., Chau, V. T., & Bessa, M. A. (2016). Wave Dispersion and Basic Concepts of Peridynamics Compared to Classical Nonlocal Damage Models. *Journal of Applied Mechanics*, vol. 83, no. 11, 111004.

13. Beissel, S., & Belytschko, T. (1996). Nodal integration of the element-free Galerkin method. *Computer methods in applied mechanics and engineering*, 139(1-4), 49-74.
14. Belytschko, T., Fish, J., & Engelmann, B. E. (1988). A finite element with embedded localization zones. *Computer Methods in Applied Mechanics and Engineering*, vol. 70, pp. 59–89.
15. Belytschko, T., Lu, Y. Y., & Gu, L. (1994). Element-free Galerkin methods. *International journal for numerical methods in engineering*, 37(2), 229-256.
16. Belytschko, T., Lu, Y. Y., Gu, L., & Tabbara, M. (1995). Element-free Galerkin methods for static and dynamic fracture. *International Journal of Solids and Structures*, 32(17-18), 2547-2570.
17. Belytschko, T., Krongauz, Y., Fleming, M., Organ, D., & Liu, W. K. (1996). Smoothing and accelerated computations in the element free Galerkin method. *Journal of Computational and Applied Mathematics*, 74(1-2), 111-126.
18. Belytschko, T., & Black, T. (1999). Elastic crack growth in finite elements with minimal remeshing. *International Journal for Numerical Methods in Engineering*, vol. 45, no. 5, pp. 601–620.
19. Belytschko, T., Liu, W. K., Moran, B., & Elkhodary, K. (2013). *Nonlinear finite elements for continua and structures*. John wiley & sons.
20. Biot, M. A. (1941). General theory of three-dimensional consolidation. *Journal of applied physics*, 12(2), 155-164.
21. Biot, M. A. (1956a). Theory of Propagation of Elastic Waves in a Fluid - Saturated Porous Solid. I. Low - Frequency Range. *The Journal of the Acoustical Society of America*, 28(2), 168-178.
22. Biot, M. A. (1956b). Theory of propagation of elastic waves in a fluid-saturated porous solid. II. Higher frequency range. *Journal of the Acoustical Society of America*, 28(2), 179-191.
23. Blanton, T. L. (1982). An experimental study of interaction between hydraulically induced and pre-existing fractures. In *SPE unconventional gas recovery symposium*. Society of Petroleum Engineers.
24. Bochev, P. B., Dohrmann, C. R., & Gunzburger, M. D. (2006). Stabilization of low-order mixed finite elements for the Stokes equations. *SIAM Journal on Numerical Analysis*, 44(1), 82-101.

25. Boone, T. J., & Ingraffea, A. R. (1990). A numerical procedure for simulation of hydraulically - driven fracture propagation in poroelastic media. *International Journal for Numerical and Analytical Methods in Geomechanics*, 14(1), 27-47.
26. Bordas, S., Rabczuk, T., & Zi, G. (2008). Three-dimensional crack initiation, propagation, branching and junction in non-linear materials by an extended meshfree method without asymptotic enrichment. *Eng Fract Mech*, vol. 75, no. 5, pp. 943–960.
27. Borden, M. J., Hughes, T. J., Landis, C. M., & Verhoosel, C. V. (2014). A higher-order phase-field model for brittle fracture: Formulation and analysis within the isogeometric analysis framework. *Computer Methods in Applied Mechanics and Engineering*, vol. 273, pp. 100-118.
28. Brezzi, F. (1974). On the existence, uniqueness and approximation of saddle-point problem arising from Lagrangian multipliers. *ESAIM Math Model Numer Anal* 8(2): 129-151.
29. Bui, H. H., Fukagawa, R., Sako, K., & Ohno, S. (2008). Lagrangian meshfree particles method (SPH) for large deformation and failure flows of geomaterial using elastic–plastic soil constitutive model. *International Journal for Numerical and Analytical Methods in Geomechanics*, 32(12), 1537-1570.
30. Bui, H. H., & Fukagawa, R. (2013). An improved SPH method for saturated soils and its application to investigate the mechanisms of embankment failure: Case of hydrostatic pore - water pressure. *International Journal for numerical and analytical methods in geomechanics*, 37(1), 31-50.
31. Carrier, B., & Granet, S. (2012). Numerical modeling of hydraulic fracture problem in permeable medium using cohesive zone model. *Engineering fracture mechanics*, 79, 312-328.
32. Cervera, M., & Chiumenti, M. (2006a). Smearred crack approach: back to the original track. *International journal for numerical and analytical methods in geomechanics*, vol. 30, no. 12, pp. 1173-1199.
33. Cervera, M., & Chiumenti, M. (2006b). Mesh objective tensile cracking via a local continuum damage model and a crack tracking technique. *Computer methods in applied mechanics and engineering*, vol. 196, no. 1, pp. 304-320.
34. Chen, A.T.F. (1966). Plane strain and axisymmetric primary consolidation of saturated clays. Ph.D. Thesis, Rensselaer Polytechnic Institute, Troy, New York.
35. Chen, J. S., Pan, C., Wu, C. T., & Liu, W. K. (1996a). Reproducing kernel particle methods for large deformation analysis of nonlinear structures. *Comput Meth Appl Mech Eng*, vol. 139, no. 1, pp. 195-227.

36. Chen, J. S., & Pan, C. (1996b). A pressure projection method for nearly incompressible rubber hyperelasticity, Part I: Theory. *Journal of applied mechanics*, 63(4), 862-868.
37. Chen, J. S., Wu, C. T., & Pan, C. (1996c). A pressure projection method for nearly incompressible rubber hyperelasticity, part II: Applications. *Journal of applied mechanics*, 63(4), 869-876.
38. Chen, J. S., Yoon, S., Wang, H. P., & Liu, W. K. (2000a). An improved reproducing kernel particle method for nearly incompressible finite elasticity. *Computer methods in applied mechanics and engineering*, 181(1-3), 117-145.
39. Chen, J. S., & Wang, H. P. (2000b). New boundary condition treatments in meshfree computation of contact problems. *Comput Meth Appl Mech Eng*, vol. 187, no. 3, pp. 441-468.
40. Chen, J. S., Wu, C. T., & Belytschko, T. (2000c). Regularization of material instabilities by meshfree approximations with intrinsic length scales. *International Journal for Numerical Methods in Engineering*, 47(7), 1303-1322.
41. Chen, J. S., Wu, C. T., Yoon, S., & You, Y. (2001). A stabilized conforming nodal integration for Galerkin meshfree methods. *Int J Numer Meth Eng*, vol. 50, no. 2, pp. 435-466.
42. Chen, J. S., Yoon, S., & Wu, C. T. (2002). Non-linear version of stabilized conforming nodal integration for Galerkin mesh-free methods. *Int J Numer Meth Eng*, vol. 53, no. 12, pp. 2587-2615.
43. Chen, J. S., Zhang, X., & Belytschko, T. (2004). An implicit gradient model by a reproducing kernel strain regularization in strain localization problems. *Comput Meth Appl Mech Eng*, vol. 193, no. 27, pp. 2827-2844.
44. Chen, J. S., & Wu, Y. (2007). Stability in Lagrangian and semi-Lagrangian reproducing kernel discretizations using nodal integration in nonlinear solid mechanics. *Advances in Meshfree Techniques*, 55-76.
45. Chen, J. S., Hillman, M., & Rüter, M. (2013). An arbitrary order variationally consistent integration method for Galerkin meshfree methods. *Int J Numer Meth Eng*, vol. 95, no. 5, pp. 387-418.
46. Chen, J. S., & Belytschko, T. (2015). Meshless and meshfree methods. In *Encyclopedia of applied and computational mathematics* (pp. 886-894). Springer Berlin Heidelberg.
47. Chen, J. S., Hillman, M., & Chi, S. W. (2017a). Meshfree Methods: Progress Made after 20 Years. *Journal of Engineering Mechanics*, vol. 143, no. 4, 04017001.

48. Chen, J. S., Liu, W. K., Hillman, M., Chi, S. W., Lian, Y., & Bessa, M. A. (2017b). Reproducing Kernel Approximation and Discretization. *Encyclopedia of Computational Mechanics, Second Edition* [Eds. Erwin Stein, René de Borst, and Thomas J. R. Hughes], John Wiley & Sons, Ltd., Chapter 20, pp. 1-41.
49. Choo, J., & Borja, R. I. (2015). Stabilized mixed finite elements for deformable porous media with double porosity. *Computer Methods in Applied Mechanics and Engineering*, 293, 131-154.
50. Coussy, O. (2004). *Poromechanics*. Wiley: New York.
51. Cryer, C. W. (1963). A comparison of the three-dimensional consolidation theories of Biot and Terzaghi. *The Quarterly Journal of Mechanics and Applied Mathematics*, 16(4), 401-412.
52. Dai, Z., Huang, Y., Cheng, H., & Xu, Q. (2014). 3D numerical modeling using smoothed particle hydrodynamics of flow-like landslide propagation triggered by the 2008 Wenchuan earthquake. *Engineering Geology*, 180, 21-33.
53. de Borst, R. (2002). Fracture in quasi-brittle materials: a review of continuum damage-based approaches. *Engineering fracture mechanics*, vol. 69, no. 2, pp. 95-112.
54. de Borst, R., Remmers, J. J. C., Needleman, A., & Abellan, M. A. (2004). Discrete vs smeared crack models for concrete fracture: bridging the gap. *International Journal for Numerical and Analytical Methods in Geomechanics*, vol. 28, no. 7-8, pp. 583-607.
55. de Borst, R., Remmers, J. J. C., & Needleman, A. (2006a). Mesh-independent discrete numerical representations of cohesive-zone models. *Engineering Fracture Mechanics*, vol. 73, pp. 160-177.
56. de Borst, R., Ráthoré J., & Abellan, M. A. (2006b). A numerical approach for arbitrary cracks in a fluid-saturated medium. *Archive of Applied Mechanics*, 75(10-12), 595-606.
57. de Borst, R., & Verhoosel, C. V. (2016). Gradient damage vs phase-field approaches for fracture: Similarities and differences. *Computer Methods in Applied Mechanics and Engineering*, vol. 312, pp. 78-94.
58. de Vree, J. H. P., Brekelmans, W. A. M., & Gils, M. A. J. (1995). Comparison of nonlocal approaches in continuum damage mechanics. *Comput Struct*, vol. 55, pp. 581-588.
59. Desmorat, R., Gatuíngt, F., & Jirásek, M. (2015). Nonlocal models with damage-dependent interactions motivated by internal time. *Engineering Fracture Mechanics*, vol. 142, pp. 255-275.

60. Di Luzio, G., & Bažant, Z. P. (2005). Spectral analysis of localization in nonlocal and over-nonlocal materials with softening plasticity or damage. *International Journal of Solids and Structures*, vol. 42, no. 23, 6071-6100.
61. Dohrmann, C. R., & Bochev, P. B. (2004). A stabilized finite element method for the Stokes problem based on polynomial pressure projections. *International Journal for Numerical Methods in Fluids*, 46(2), 183-201.
62. Dolbow, J., & Belytschko, T. (1999). Numerical integration of the Galerkin weak form in meshfree methods. *Computational mechanics*, 23(3), 219-230.
63. Duan, Q., Li, X., Zhang, H., Wang, B., & Gao, X. (2012). Quadratically consistent one-point (QC1) quadrature for meshfree Galerkin methods. *Computer Methods in Applied Mechanics and Engineering*, 245, 256-272.
64. Ehlers, W., & Luo, C. (2017). A phase-field approach embedded in the Theory of Porous Media for the description of dynamic hydraulic fracturing. *Computer Methods in Applied Mechanics and Engineering*, 315, 348-368.
65. Fernández-Méndez, S., & Huerta, A. (2004). Imposing essential boundary conditions in mesh-free methods. *Computer methods in applied mechanics and engineering*, 193(12-14), 1257-1275.
66. Fu, P., Johnson, S. M., & Carrigan, C. R. (2013). An explicitly coupled hydro-geomechanical model for simulating hydraulic fracturing in arbitrary discrete fracture networks. *International Journal for Numerical and Analytical Methods in Geomechanics*, 37(14), 2278-2300.
67. Gawin, D., Baggio, P., & Schrefler, B. A. (1995). Coupled heat, water and gas flow in deformable porous media. *International Journal for numerical methods in fluids*, 20(8 - 9), 969-987.
68. Gibson, R.E., Knight, K., & Taylor, P.W. (1963). A critical experiment to examine theories of three-dimensional consolidation. In: *Proceedings of the European Conference on Soil Mechanics and Foundation Engineering*, Wiesbaden.
69. Giry, C., Dufour, F., & Mazars, J. (2011). Stress-based nonlocal damage model. *International Journal of Solids and Structures*, vol. 48, no. 25, pp. 3431-3443.
70. Gravouil, A., Moës, N., & Belytschko, T. (2002). Non-planar 3D crack growth by the extended finite element and level sets - Part II: Level set update. *Int J Numer Meth Eng*, vol. 53, no. 11, pp. 2569–2586.
71. Griffiths, D. V., & Lane, P. A. (1999). Slope stability analysis by finite elements.

Geotechnique, 49(3), 387-403.

72. Gupta, P., & Duarte, C. A. (2014). Simulation of non-planar three-dimensional hydraulic fracture propagation. *International Journal for Numerical and Analytical Methods in Geomechanics*, 38(13), 1397-1430.
73. Haga, J. B., Osnes, H., & Langtangen, H. P. (2012). On the causes of pressure oscillations in low - permeable and low - compressible porous media. *International Journal for Numerical and Analytical Methods in Geomechanics*, 36(12), 1507-1522.
74. Haque, U., da Silva, P. F., Lee, J., Benz, S., Auflič, M. J., & Blum, P. (2017). Increasing Fatal Landslides in Europe. In *Workshop on World Landslide Forum* (pp. 505-512). Springer, Cham.
75. Heister, T., Wheeler, M. F., & Wick, T. (2015). A primal-dual active set method and predictor-corrector mesh adaptivity for computing fracture propagation using a phase-field approach. *Computer Methods in Applied Mechanics and Engineering*, vol. 290, pp. 466-495.
76. Hillman, M., & Chen, J. S. (2016). An accelerated, convergent, and stable nodal integration in Galerkin meshfree methods for linear and nonlinear mechanics. *International Journal for Numerical Methods in Engineering*, 107(7), 603-630.
77. Hua, L. (2011). Stable element-free Galerkin solution procedures for the coupled soil-pore fluid problem. *International Journal for Numerical Methods in Engineering*, 86(8), 1000-1026.
78. Huang, M., & Jia, C. Q. (2009). Strength reduction FEM in stability analysis of soil slopes subjected to transient unsaturated seepage. *Computers and Geotechnics*, 36(1-2), 93-101.
79. Huang, Y., Zhang, W., Xu, Q., Xie, P., & Hao, L. (2012). Run-out analysis of flow-like landslides triggered by the Ms 8.0 2008 Wenchuan earthquake using smoothed particle hydrodynamics. *Landslides*, 9(2), 275-283.
80. Huang, Y., & Dai, Z. (2014). Large deformation and failure simulations for geo-disasters using smoothed particle hydrodynamics method. *Engineering Geology*, 168, 86-97.
81. Irzal, F., Remmers, J. J., Huyghe, J. M., & de Borst, R. (2013). A large deformation formulation for fluid flow in a progressively fracturing porous material. *Computer Methods in Applied Mechanics and Engineering*, 256, 29-37.
82. Iseno, H., Kohashi, H., Furumoto, K., Mori, H., & Ohno, M. (2004). Large model tests of levee reinforcement method with toe drain for seepage failure. In *Proc., Annual Symp. of Japanese Geotechnical Society* (Vol. 39, pp. 1255-1256).

83. Jäger, P., Steinmann, P., & Kuhl, E. (2008). On local tracking algorithms for the simulation of three-dimensional discontinuities. *Computational Mechanics*, vol. 42, no. 3, pp. 395-406.
84. Jamison, W., & Azad, A. (2017). The hydraulic fracture–natural fracture network configuration in shale reservoirs: Geological limiting factors. *Journal of Petroleum Science and Engineering*, 159, 205-229.
85. Jha, B., & Juanes, R. (2007). A locally conservative finite element framework for the simulation of coupled flow and reservoir geomechanics. *Acta Geotechnica*, 2(3), 139-153.
86. Jiříšek, M., & Zimmermann T. (1998a). Analysis of rotating crack model. *Journal of engineering mechanics*, vol. 124, no. 8, pp. 842-851.
87. Jiříšek, M. (1998b). Element-Free Galerkin Method Applied To Strain-Softening Materials. *Proc. Computational Modelling of Concrete Structures (EURO-C)*, ed. R. de Borst, N. Bicanic, H. Mang, and G. Meschke, Balkema, Rotterdam, pp. 311-319.
88. Jiříšek, M. (2000). Comparative study on finite elements with embedded discontinuities, *Comput. Methods Appl. Mech. Engrg*, vol. 188, pp. 307–330.
89. Jiříšek, M., & Patzák, B. (2002). Consistent tangent stiffness for nonlocal damage models. *Computers & structures*, 80(14-15), 1279-1293.
90. Jiříšek, M. (2011). Damage and smeared crack models. In *Numerical modeling of concrete cracking*. Springer, Vienna, pp. 1-49.
91. Jiříšek, M., & Bauer, M. (2012). Numerical aspects of the crack band approach. *Computers & Structures*, vol. 110, pp. 60-78.
92. Kalthoff, J. F., & Winkler, S. (1987). Failure mode transition at high rates of shear loading. *International conference on impact loading and dynamic behavior of materials*, vol 1, pp 185-19.
93. Karim, M. R., Nogami, T., & Wang, J. G. (2002). Analysis of transient response of saturated porous elastic soil under cyclic loading using element-free Galerkin method. *International Journal of Solids and Structures*, 39(24), 6011-6033.
94. Khoei, A. R., Azami, A. R., & Haeri, S. M. (2004). Implementation of plasticity based models in dynamic analysis of earth and rockfill dams: A comparison of Pastor–Zienkiewicz and cap models. *Computers and Geotechnics*, 31(5), 384-409.
95. Khoei, A. R., & Mohammadnejad, T. (2011). Numerical modeling of multiphase fluid flow in deforming porous media: A comparison between two-and three-phase models for

- seismic analysis of earth and rockfill dams. *Computers and Geotechnics*, 38(2), 142-166.
96. Khoei, A. R., Vahab, M., Haghghat, E., & Moallemi, S. (2014). A mesh-independent finite element formulation for modeling crack growth in saturated porous media based on an enriched-FEM technique. *International Journal of Fracture*, 188(1), 79-108.
 97. Khoshghalb, A., & Khalili, N. (2010). A stable meshfree method for fully coupled flow-deformation analysis of saturated porous media. *Computers and Geotechnics*, 37(6), 789-795.
 98. Kim, J., Tchelepi, H. A., & Juanes, R. (2011). Stability and convergence of sequential methods for coupled flow and geomechanics: Fixed-stress and fixed-strain splits. *Computer Methods in Applied Mechanics and Engineering*, 200(13-16), 1591-1606.
 99. Kim, J., Wang, W., & Regueiro, R. A. (2015). Hybrid time integration and coupled solution methods for nonlinear finite element analysis of partially saturated deformable porous media at small strain. *International Journal for Numerical and Analytical Methods in Geomechanics*, 39(10), 1073-1103.
 100. Krysl, P., & Belytschko, T. (1997). Element-free Galerkin method: Convergence of the continuous and discontinuous shape functions. *Computer methods in applied mechanics and engineering*, 148(3-4), 257-277.
 101. Krysl, P., & Belytschko, T. (1999). The element free Galerkin method for dynamic propagation of arbitrary 3-D cracks. *Int J Numer Meth Eng*, vol. 44, no. 6, pp. 767-800.
 102. Laloui, L., Klubertanz, G., & Vulliet, L. (2003). Solid-liquid-air coupling in multiphase porous media. *International Journal for Numerical and Analytical Methods in Geomechanics*, 27(3), 183-206.
 103. Lee, S., Wheeler, M. F., & Wick, T. (2016). Pressure and fluid-driven fracture propagation in porous media using an adaptive finite element phase field model. *Computer Methods in Applied Mechanics and Engineering*, 305, 111-132.
 104. Li, L. C., Tang, C. A., Li, G., Wang, S. Y., Liang, Z. Z., & Zhang, Y. B. (2012). Numerical simulation of 3D hydraulic fracturing based on an improved flow-stress-damage model and a parallel FEM technique. *Rock Mechanics and rock engineering*, 45(5), 801-818.
 105. Li, S., & Liu, W.K. (2004). *Meshfree Particle Methods*. Springer-Verlag Berlin Heidelberg.
 106. Li, W., & Wei, C. (2015). An efficient finite element procedure for analyzing three-phase porous media based on the relaxed Picard method. *International Journal for Numerical Methods in Engineering*, 101(11), 825-846.

107. Li, X., Han, X., & Pastor, M. (2003). An iterative stabilized fractional step algorithm for finite element analysis in saturated soil dynamics. *Computer Methods in Applied Mechanics and Engineering*, 192(35-36), 3845-3859.
108. Liakopoulos, A.C. (1965). Transient flow through unsaturated porous media. PhD Thesis, University of California, Berkley.
109. Liu, F., & Borja, R. I. (2008). A contact algorithm for frictional crack propagation with the extended finite element method. *International Journal for Numerical methods in engineering*, 76(10), 1489-1512.
110. Liu, W. K., Jun, S., & Zhang, Y. F. (1995). Reproducing kernel particle methods. *Int J Numer Meth Fluid*, vol. 20, no. 8-9, pp. 1081-1106.
111. Lu, N., & Likos, W. J. (2004). *Unsaturated soil mechanics*. Wiley.
112. Ma, J. (2015). Review of permeability evolution model for fractured porous media. *Journal of Rock Mechanics and Geotechnical Engineering*, 7(3), 351-357.
113. Mandel, J. (1953). Consolidation des sols. *G éotechnique* 3(7): 287-299.
114. Mauthe, S., & Miehe, C. (2017). Hydraulic fracture in poro-hydro-elastic media. *Mechanics Research Communications*, 80, 69-83.
115. Mazars, J. (1986). A description of micro- and macro-scale damage of concrete structures. *J Eng Fract Mech*, vol. 25, pp. 729–737.
116. Meroi, E. A., Schrefler, B. A., & Zienkiewicz, O. C. (1995). Large strain static and dynamic semisaturated soil behaviour. *International Journal for Numerical and Analytical Methods in Geomechanics*, 19(2), 81-106.
117. McDougall, S. (2016). 2014 Canadian Geotechnical Colloquium: Landslide runout analysis-current practice and challenges. *Canadian Geotechnical Journal*, 54(5), 605-620.
118. Miehe, C., Welschinger F., & Hofacker M. (2010). Thermodynamically consistent phase-field models of fracture: variational principles and multi-field FE implementations. *Int J Numer Methods Eng*, vol. 83, pp. 1273–1311.
119. Miehe, C., Mauthe, S., & Teichtmeister, S. (2015). Minimization principles for the coupled problem of Darcy–Biot-type fluid transport in porous media linked to phase field modeling of fracture. *Journal of the Mechanics and Physics of Solids*, 82, 186-217.
120. Mo ̇s, N., Dolbow, J., & Belytschko, T. (1999). A finite element method for crack growth without remeshing. *International Journal for Numerical Methods in Engineering*, vol. 46,

no. 1, pp. 131–150.

121. Moš, N., Gravouil, A., & Belytschko, T. (2002). Non-planar 3D crack growth by the extended finite element and level sets - Part I: Mechanical model. *Int J Numer Meth Eng*, vol. 53, no. 11, pp. 2549–2568.
122. Mohammadnejad, T., & Khoei, A. R. (2013). An extended finite element method for hydraulic fracture propagation in deformable porous media with the cohesive crack model. *Finite Elements in Analysis and Design*, 73, 77-95.
123. Monaghan, J. J. (2000). SPH without a tensile instability. *Journal of Computational Physics*, 159(2), 290-311.
124. Montgomery, C. T., & Smith, M. B. (2010). Hydraulic fracturing: history of an enduring technology. *Journal of Petroleum Technology*, 62(12), 26-40.
125. Mori, H. (2008). The SPH method to simulate river levee failures. Master's thesis, Univ. of Cambridge, Cambridge, U.K.
126. Murakami, A., Kawabata, H., & Aoyama, S. (2000) EFGM analysis for saturated soil. In: *Proceedings of the 10th International Conference on Computer Methods and Advances in Geomechanics*. Tucson.
127. Oliaei, M. N., Soga, K., & Pak, A. (2009). Some numerical issues using element - free Galerkin mesh - less method for coupled hydro - mechanical problems. *International journal for numerical and analytical methods in geomechanics*, 33(7), 915-938.
128. Oliver, J., Dias, I. F., & Huespe, A. E. (2014). Crack-path field and strain-injection techniques in computational modeling of propagating material failure. *Computer Methods in Applied Mechanics and Engineering*, vol. 274, pp. 289-348.
129. Organ, D., Fleming, M., Terry, T., & Belytschko, T. (1996). Continuous meshless approximations for nonconvex bodies by diffraction and transparency. *Computational mechanics*, vol. 18, no. 3, pp. 225-235.
130. Palciauskas, V. V., & Domenico, P. A. (1982). Characterization of drained and undrained response of thermally loaded repository rocks. *Water Resources Research*, 18(2), 281-290.
131. Parvaneh, S. M., & Foster, C. D. (2016). On numerical aspects of different updating schedules for tracking fracture path in strain localization modeling. *Engineering Fracture Mechanics*, vol. 152, pp. 26-57.
132. Pasetto, M., Chen, J. S., & Wei, H. (2017) Coupled Lagrangian and semi-Lagrangian RKPM. *Engineering Mechanics Institute Conference*, San Diego, USA.

133. Pastor, M., Li, T., Liu, X., Zienkiewicz, O. C., & Quecedo, M. (2000). A fractional step algorithm allowing equal order of interpolation for coupled analysis of saturated soil problems. *Mechanics of Cohesive - frictional Materials: An International Journal on Experiments, Modelling and Computation of Materials and Structures*, 5(7), 511-534.
134. Pastor, M., Haddad, B., Sorbino, G., Cuomo, S., & Drempetic, V. (2009). A depth - integrated, coupled SPH model for flow - like landslides and related phenomena. *International Journal for numerical and analytical methods in geomechanics*, 33(2), 143-172.
135. Pedroso, D. M. (2015). A consistent u-p formulation for porous media with hysteresis. *International Journal for Numerical Methods in Engineering*, 101(8), 606-634.
136. Peerlings, R. H. J., de Borst, R., Brekelmans, W. A. M., & de Vree, J. H. P. (1996). Gradient-enhanced damage for quasi-brittle materials. *Int J Numer Methods Eng*, vol. 39, pp. 3391–3403.
137. Petley, D. (2012). Global patterns of loss of life from landslides. *Geology*, 40(10), 927-930.
138. Phillips, P. J., & Wheeler, M. F. (2007). A coupling of mixed and continuous Galerkin finite element methods for poroelasticity I: the continuous in time case. *Computational Geosciences*, 11(2), 131.
139. Pijaudier-Cabot, G., & Bažant, Z. P. (1987). Nonlocal damage theory. *J Eng Mech*, vol. 118, pp. 1512–1533.
140. Pijaudier-Cabot, G., Dufour, F., & Choinska, M. (2009). Permeability due to the increase of damage in concrete: from diffuse to localized damage distributions. *Journal of engineering mechanics*, 135(9), 1022-1028.
141. Poh, L. H., & Sun, G. (2017). Localizing gradient damage model with decreasing interactions. *International Journal for Numerical Methods in Engineering*, vol. 110, no. 6, pp. 503-522.
142. Preisig, M., & Prévost, J. H. (2011). Stabilization procedures in coupled poromechanics problems: A critical assessment. *International Journal for Numerical and Analytical Methods in Geomechanics*, 35(11), 1207-1225.
143. Prevost, J. H. (2014). Two-way coupling in reservoir-geomechanical models: vertex-centered Galerkin geomechanical model cell-centered and vertex-centered finite volume reservoir models. *International Journal for Numerical Methods in Engineering*, 98(8), 612-624.
144. Prevost, J. H., & Sukumar, N. (2016). Faults simulations for three-dimensional

reservoir-geomechanical models with the extended finite element method. *Journal of the Mechanics and Physics of Solids*, 86, 1-18.

145. Puso, M. A., Chen, J. S., Zywicki, E., & Elmer, W. (2008). Meshfree and finite element nodal integration methods. *International Journal for Numerical Methods in Engineering*, 74(3), 416-446.
146. Rabczuk, T., & Belytschko, T. (2004). Cracking particles: a simplified meshfree method for arbitrary evolving cracks. *International Journal for Numerical Methods in Engineering*, vol. 61, pp. 2316–2343.
147. Rabczuk, T., & Belytschko, T. (2007). A three-dimensional large deformation meshfree method for arbitrary evolving cracks. *Comput. Methods Appl. Mech. Engrg*, vol. 196, pp. 2777–2799.
148. Rabczuk, T., Zi, G., Bordas, S., & Nguyen-Xuan, H. (2010). A simple and robust three-dimensional cracking-particle method without enrichment, *Computer Methods in Applied Mechanics and Engineering*, vol. 199, no. 37-40, pp. 2437-2455.
149. Rabczuk, T. (2013). *Computational Methods for Fracture in Brittle and Quasi-Brittle Solids: State-of-the-Art Review and Future Perspectives*. *Applied Mathematics*. Article ID 849231, 38 pages.
150. Randles, P. W., & Libersky, L. D. (1996). Smoothed particle hydrodynamics: some recent improvements and applications. *Computer methods in applied mechanics and engineering*, 139(1-4), 375-408.
151. Rangarajan, R., Chiaramonte, M. M., Hunsweck, M. J., Shen, Y., & Lew, A. J. (2015). Simulating curvilinear crack propagation in two dimensions with universal meshes. *International Journal for Numerical Methods in Engineering*, vol. 102, no. 3-4, pp. 632-670.
152. Remmers, J. J. C., de Borst, R., & Needleman, A. (2003). A cohesive segments method for the simulation of crack growth. *Computational Mechanics*, vol. 31, pp. 69-77.
153. R  thor   J., Gravouil, A., & Combescure, A. (2005). An energy-conserving scheme for dynamic crack growth using the eXtended finite element method. *International Journal for Numerical Methods in Engineering*, vol. 63, no. 5, pp. 631-659.
154. R  thor   J., de Borst, R., & Abellan, M. A. (2007). A two-scale approach for fluid flow in fractured porous media. *International Journal for Numerical Methods in Engineering*, 71(7), 780-800.
155. R  thor   J., de Borst, R., & Abellan, M. A. (2008). A two-scale model for fluid flow in an

- unsaturated porous medium with cohesive cracks. *Computational Mechanics*, 42(2), 227-238.
156. Rice, J. R., & Cleary, M. P. (1976). Some basic stress diffusion solutions for fluid - saturated elastic porous media with compressible constituents. *Reviews of Geophysics*, 14(2), 227-241.
 157. Samimi, S., & Pak, A. (2012). Three-dimensional simulation of fully coupled hydro-mechanical behavior of saturated porous media using Element Free Galerkin (EFG) method. *Computers and Geotechnics*, 46, 75-83.
 158. Santillán, D., Juanes, R., & Cueto-Felgueroso, L. (2018). Phase Field Model of Hydraulic Fracturing in Poroelastic Media: Fracture Propagation, Arrest, and Branching Under Fluid Injection and Extraction. *Journal of Geophysical Research: Solid Earth*.
 159. Schanz, M., & Cheng, A. D. (2000). Transient wave propagation in a one-dimensional poroelastic column. *Acta Mechanica*, 145(1-4), 1-18.
 160. Schanz, M. (2009). Poroelastodynamics: linear models, analytical solutions, and numerical methods. *Applied mechanics reviews*, 62(3), 030803.
 161. Schiffman, R. L., Chen, A. T., & Jordan, J. C. (1969). An analysis of consolidation theories. *Journal of Soil Mechanics & Foundations Div.* 95: 285-312.
 162. Schrefler, B. A., & Xiaoyong, Z. (1993). A fully coupled model for water flow and airflow in deformable porous media. *Water Resources Research*, 29(1), 155-167.
 163. Schrefler, B. A., & Scotta, R. (2001). A fully coupled dynamic model for two-phase fluid flow in deformable porous media. *Computer methods in applied mechanics and engineering*, 190(24), 3223-3246.
 164. Schrefler, B. A., Secchi, S., & Simoni, L. (2006). On adaptive refinement techniques in multi-field problems including cohesive fracture. *Computer methods in applied mechanics and engineering*, 195(4-6), 444-461.
 165. Secchi, S., & Schrefler, B. A. (2012). A method for 3-D hydraulic fracturing simulation. *International journal of fracture*, 178(1-2), 245-258.
 166. Segura, J. M., & Carol, I. (2008). Coupled HM analysis using zero-thickness interface elements with double nodes. Part I: Theoretical model. *International journal for numerical and analytical methods in geomechanics*, 32(18), 2083-2101.
 167. Shahbodagh-Khan, B., Khalili, N., & Esgandani, G. A. (2015). A numerical model for

- nonlinear large deformation dynamic analysis of unsaturated porous media including hydraulic hysteresis. *Computers and Geotechnics*, 69, 411-423.
168. Shibata, T., & Murakami, A. (2011). A stabilization procedure for soil-water coupled problems using the element-free Galerkin method. *Computers and Geotechnics*, 38(5), 585-597.
 169. Simo, J. C., Oliver, J., & Armero, F. (1993). An analysis of strong discontinuities induced by strain-softening in rate-independent inelastic solids. *International Journal for Numerical Methods in Engineering*, vol. 12, pp. 277-296.
 170. Simone, A., Askes, H., & Sluys, L. J. (2004). Incorrect initiation and propagation of failure in non-local and gradient-enhanced media. *International Journal of Solids and Structures*, vol. 41, no. 2, pp. 351-363.
 171. Smith, M. B., & Montgomery, C. (2015). *Hydraulic fracturing*. CRC Press.
 172. Sneddon, I. (1946). The distribution of stress in the neighbourhood of a crack in an elastic solid. *Proc. R. Soc. Lond. A*, 187(1009), 229-260.
 173. Soares, D. (2014). Iterative analysis of pore-dynamic models discretized by finite elements. *International Journal for Numerical and Analytical Methods in Geomechanics*, 38(4), 391-405.
 174. Soga, K., Alonso, E., Yerro, A., Kumar, K., & Bandara, S. (2015). Trends in large-deformation analysis of landslide mass movements with particular emphasis on the material point method. *Géotechnique*, 66(3), 248-273.
 175. Song, J. H., Areias, P., & Belytschko, T. (2006). A method for dynamic crack and shear band propagation with phantom nodes. *International Journal for Numerical Methods in Engineering*, vol. 67, no. 6, pp. 868-893.
 176. Song, J. H., Wang, H., & Belytschko, T. (2008). A comparative study on finite element methods for dynamic fracture. *Computational Mechanics*, vol. 42, no. 2, pp. 239-250.
 177. Song, J. H., & Belytschko, T. (2009). Cracking node method for dynamic fracture with finite elements. *International Journal for Numerical Methods in Engineering*, vol. 77, no. 3, pp. 360-385.
 178. Sun, W., Ostien, J. T., & Salinger, A. G. (2013). A stabilized assumed deformation gradient finite element formulation for strongly coupled poromechanical simulations at finite strain. *International Journal for Numerical and Analytical Methods in Geomechanics*, 37(16), 2755-2788.

179. Sun, W. (2015). A stabilized finite element formulation for monolithic thermo - hydro - mechanical simulations at finite strain. *International Journal for Numerical Methods in Engineering*, 103(11), 798-839.
180. Sweigle, J. W., Hicks, D. L., & Attaway, S. W. (1995). Smoothed particle hydrodynamics stability analysis. *Journal of computational physics*, 116(1), 123-134.
181. Swenson, D. V., & Ingraffea, A. R. (1988). Modelling mixed-mode dynamic crack propagation using finite elements: theory and applications. *Computational Mechanics*, vol. 3, pp. 187-192.
182. Triantafyllou, A., Perdikaris, P. C., & Giannakopoulos, A. E. (2014). Gradient elastodamage model for quasi-brittle materials with an evolving internal length. *Journal of Engineering Mechanics*, vol. 141, no. 4, 04014139.
183. Truster, T. J. (2016). On interface element insertion into three-dimensional meshes. *Engineering Fracture Mechanics*, vol. 153, pp. 171–174.
184. Truty, A., & Zimmermann, T. (2006). Stabilized mixed finite element formulations for materially nonlinear partially saturated two-phase media. *Computer methods in applied mechanics and engineering*, 195(13-16), 1517-1546.
185. Uzuoka, R., & Borja, R. I. (2012). Dynamics of unsaturated poroelastic solids at finite strain. *International Journal for Numerical and Analytical Methods in Geomechanics*, 36(13), 1535-1573.
186. Van Genuchten, M. T. (1980). A closed-form equation for predicting the hydraulic conductivity of unsaturated soils 1. *Soil science society of America journal*, 44(5), 892-898.
187. Verruijt, A., & van Baars, S. (2007). *Soil Mechanics*. VSSD: Delft.
188. Wan, J., Durlofsky, L. J., Hughes, T. J. R., & Aziz, K. (2003). Stabilized finite element methods for coupled geomechanics-reservoir flow simulations. In *SPE Reservoir Simulation Symposium*. Society of Petroleum Engineers.
189. Wang, J. G., Liu, G. R., & Wu, Y. G. (2001). A point interpolation method for simulating dissipation process of consolidation. *Computer Methods in Applied Mechanics and Engineering*, 190(45), 5907-5922.
190. Wang, J. G., Liu, G. R., & Lin, P. (2002). Numerical analysis of Biot's consolidation process by radial point interpolation method. *International Journal of Solids and Structures*, 39(6), 1557-1573.

191. Wei, W. B., Cheng, Y. M., & Li, L. (2009). Three-dimensional slope failure analysis by the strength reduction and limit equilibrium methods. *Computers and geotechnics*, 36(1-2), 70-80.
192. Wei, W. B., & Cheng, Y. M. (2010). Stability analysis of slope with water flow by strength reduction method. *Soils and foundations*, 50(1), 83-92.
193. Weihe, S., Kröplin, B., & de Borst, R. (1998). Classification of smeared crack models based on material and structural properties. *International journal of solids and structures*, vol. 35, no. 12, pp. 1289–1308.
194. Weng, X. (2015). Modeling of complex hydraulic fractures in naturally fractured formation. *Journal of Unconventional Oil and Gas Resources*, 9, 114-135.
195. Wheeler, M. F., Wick, T., & Wollner, W. (2014). An augmented-Lagrangian method for the phase-field approach for pressurized fractures. *Computer Methods in Applied Mechanics and Engineering*, 271, 69-85.
196. White, J. A., & Borja, R. I. (2008). Stabilized low-order finite elements for coupled solid-deformation/fluid-diffusion and their application to fault zone transients. *Computer Methods in Applied Mechanics and Engineering*, 197(49-50), 4353-4366.
197. Xie, Y., & Wang, G. (2014). A stabilized iterative scheme for coupled hydro - mechanical systems using reproducing kernel particle method. *International Journal for Numerical Methods in Engineering*, 99(11), 819-843.
198. Xu, X. P., & Needleman, A. (1994). Numerical simulation of fast crack growth in brittle solids. *Journal of the Mechanics and Physics of Solids*, vol. 42, no. 9, pp. 1397–1434.
199. Xu, W., & Waas, A. M. (2016). Modeling damage growth using the crack band model; effect of different strain measures. *Engineering Fracture Mechanics*, vol. 152, pp. 126–138.
200. Zienkiewicz, O. C., & Shiomi, T. (1984). Dynamic behaviour of saturated porous media; the generalized Biot formulation and its numerical solution. *International journal for numerical and analytical methods in geomechanics*, 8(1), 71-96.
201. Zienkiewicz, O.C., Chan, A. H. C., Pastor, M., Paul, D. K., & Shiomi, T. (1990a). Static and dynamic behaviour of soils: a rational approach to quantitative solutions. I. Fully saturated problems. In *Proceedings of the Royal Society of London A: Mathematical, Physical and Engineering Sciences*, 429(1877), 285-309.
202. Zienkiewicz, O.C., Xie, Y. M., Schrefler, B. A., Ledesma, A., & Bićanić, N. (1990b). Static and dynamic behaviour of soils: a rational approach to quantitative solutions. II. Semi-saturated problems. In *Proceedings of the Royal Society of London A: Mathematical,*

Physical and Engineering Sciences, 429(1877), 311-321.

203. Zienkiewicz, O.C., Chan, A.H.C., Pastor, M., Schrefler, B.A., & Shiomi, T. (1999). *Computational Geomechanics with Special Reference to Earthquake Engineering*. Wiley: New York.
204. Zhang, H. W., & Schrefler, B. A. (2000). Gradient-dependent plasticity model and dynamic strain localisation analysis of saturated and partially saturated porous media: one dimensional model. *European Journal of Mechanics-A/Solids*, 19(3), 503-524.
205. Zhang, W. J., & Maeda, K. (2014). The model test and SPH simulations for slope and levee failure under heavy rainfall considering the coupling of soil, water and air. In *Soil Behavior and Geomechanics*, 538-547.
206. Zhang, Y., Pedroso, D. M., Li, L., & Ehlers, W. (2017). FDM solutions to linear dynamics of porous media: Efficiency, stability, and parallel solution strategy. *International Journal for Numerical Methods in Engineering*, 112(11), 1539-1563.
207. Zhou, J., Chen, M., Jin, Y., & Zhang, G. Q. (2008). Analysis of fracture propagation behavior and fracture geometry using a tri-axial fracturing system in naturally fractured reservoirs. *International Journal of Rock Mechanics and Mining Sciences*, 45(7), 1143-1152.